

Summer 2024

Experimentatal and Numerical Investigation of Turbojet Engine Performance, Emissions, and Noise/Vibrations Using Jet-A and F24 Fuel

John W. McAfee Jr

Follow this and additional works at: <https://digitalcommons.georgiasouthern.edu/etd>



Part of the [Acoustics, Dynamics, and Controls Commons](#), [Aerodynamics and Fluid Mechanics Commons](#), [Computer-Aided Engineering and Design Commons](#), and the [Propulsion and Power Commons](#)

Recommended Citation

McAfee, John W. Jr, "Experimentatal and Numerical Investigation of Turbojet Engine Performance, Emissions, and Noise/Vibrations Using Jet-A and F24 Fuel" (2024). *Electronic Theses and Dissertations*. 2830.

<https://digitalcommons.georgiasouthern.edu/etd/2830>

This thesis (open access) is brought to you for free and open access by the Jack N. Averitt College of Graduate Studies at Georgia Southern Commons. It has been accepted for inclusion in Electronic Theses and Dissertations by an authorized administrator of Georgia Southern Commons. For more information, please contact digitalcommons@georgiasouthern.edu.

EXPERIMENTAL AND NUMERICAL INVESTIGATION OF TURBOJET ENGINE
PERFORMANCE, EMISSIONS, AND NOISE/VIBRATIONS USING JET-A AND F24 FUEL

by

JOHN WILLIAM MCAFEE JR

(Under the Direction of Marcel Ilie)

ABSTRACT

Drastic improvement in cost effectiveness of high-power computing resources has generated a great interest in numerical simulation to reduce the overhead cost of engine manufacturing, maintenance, and environmental concerns of engine testing. To accomplish this goal, this research presents the differences between military F24 fuel and commercial aviation fuel Jet-A from a thermochemical and engine performance perspective. This experimental data was used to create and validate a numerical model of the engine used in the experiments fueled with both Jet-A and F24 fuels. The experimental data was collected using a research based single stage turbojet engine outfitted with many sensors for collecting engine characteristic data. Emissions data was collected for high priority species and noise/vibration data was gathered. This information was used to develop a scale numerical model of the engine. This simulation was a transient model using the EDM combustion model and k- ϵ turbulence model for engine speeds of 60,000RPM, 65,000RPM, and 70,000RPM. The results show that F24 proves to be a more economical, better performing environmentally friendly fuel. F24 has lower internal engine temperatures by approximately 4.92% across all data collection points. F24 produced a minimum of 8% greater thrust with a 5.3% decrease in fuel flow as compared to Jet-A. F24 drastically reduced emissions in all species analyzed with a maximum reduction of 160% in THC. This greatly improved the thrust specific emission of F24. F24 also had greater SPL and acceleration at all engine speeds. The numerical model followed experimental trends very closely but resulted in some outlier percentage errors at very specific points to be as great as 31%. Furthermore, numerical analysis showcased the swirl effect produced by guide vanes and rotors. The increase in engine speed enhanced the swirl number of the air and resulted in more efficient combustion, as identified through the temperature, velocity, and fuel mass fraction contours. TKE contours identified areas of the engine that

were susceptible to high energy eddies and therefore areas of flow path improvement in the turbine and exhaust stages.

EXPERIMENTAL AND NUMERICAL INVESTIGATION OF TURBOJET ENGINE
PERFORMANCE, EMISSIONS, AND NOISE/VIBRATIONS USING JET-A AND F24 FUEL

by

JOHN WILLIAM MCAFEE

B.S., Georgia Southern University, 2024

A Thesis Submitted to the Graduate Faculty of Georgia Southern University

in Partial Fulfillment of the Requirements for the Degree

MASTER OF SCIENCE

STATESBORO, GEORGIA

© 2024

JOHN WILLIAM MCAFEE

All Rights Reserved

EXPERIMENTAL AND NUMERICAL INVESTIGATION OF TURBOJET ENGINE
PERFORMANCE, EMISSIONS, AND NOISE/VIBRATIONS USING JET-A AND F24 FUEL

by

JOHN WILLIAM MCAFEE

Major Professor:
Committee:

Marcel Ilie
Valentin Soloiu
Mosfequr Rahman

Electronic Version Approved:
July 2024

DEDICATION

This thesis would not have been possible without a large collection of people who have supported, encouraged, trained, advised, and been overwhelmingly good to me.

First is my Lord and Savior Jesus Christ. He has truly led me through the valley of the shadow of death, led me by cool waters and green pastures. I wouldn't be at this point in my life without Him. He guided me to GSU to pursue my Masters, He led me to a woman who would love and support me and opened up doors to relationships with professors and lab mates that have inspired me professionally and spiritually. This thesis and the work done therefore, is for Him and His glory, that He may see my work as good, curious, and creative. He has empowered and invigorated my life with joy, purpose, desire, and drive. If your reading this, He can do it for you too.

Second is my wife, Mary Lee McAfee. She has supported me in ways I cannot express without extending the length of this thesis by numerous pages. Thank you for loving me through all the late nights and for all your understanding character as I pursued this degree. It your support that encourages me to continue when it gets difficult.

Next is my family. They have supported me in all the work I have done. They were generous when they didn't have to be. Their love for me is clear, and I am grateful for every birthday card, every red velvet cake, every academic break working with my dad and brother, and every blessed moment to hang out with my brother while we attended the same school.

This would be incomplete without mentioning my lab mates. David, Chipper, Lily, Amanda, Brad, Levi, Cesar, Austin, Aidan, Kody, Shaen, Zach, and Coleman. I could write at least a paragraph of the way each of you have not only assisted with this thesis but made it all enjoyable. The many laughs, jokes, late night conference papers, and Saturday Soloiu lunches. Your friendship means more than all of your help you put towards my own thesis, and y'all supported me a TON!

This thesis is dedicated to this large group of people's generosity, love for me, compassion, patience, and friendship. Thanks again!

ACKNOWLEDGMENTS

I would like to begin by acknowledging the assistance and guidance of my advisor Dr. Marcel Ilie. His time, mentorship, and support is what provided me with the encouragement to continue working hard to complete this thesis and achieve this awesome success. His guidance helped me learn to analyze the world as an engineer and for that I am grateful.

I would like to acknowledge Dr. Valentin Soloiu for his mentorship throughout my Master's degree. He was tough and relentless, but it was these attributes that made me an excellent engineer and prepared me for my current role. I wouldn't be where I am without his refinement of my skills.

I would like to acknowledge the guidance of my thesis committee: Dr. Marcel Ilie, Dr. Valentin Soloiu, and Dr. Mosfequr Rahman. They provided valuable insight and feedback during the review process to make my work far more diligent, comprehensive, and respectable.

Finally, I would like to acknowledge the support and guidance given by my lab mates: David Obando Ortega, Richard 'Chipper' Smith III, Brad Willis, Amanda Weaver, Lily Parker, Levi McKinney, Cesar Carapia, Austin Brant, Aidan Rowell, Kody Pierce, Shaen Mehrzed, Zachary Davis, and Coleman Norton. Our discussions developed my engineering prowess, and your encouragement to continue in my studies propelled me to success.

TABLE OF CONTENTS

DEDICATION	2
ACKNOWLEDGMENTS	3
LIST OF TABLES	8
LIST OF FIGURES	9
CHAPTER 1	12
1.1 History of Gas Turbine Engines.....	12
1.2 Purpose of Study	13
1.3 Statement of Hypothesis.....	15
CHAPTER 2	16
2.1 Types of Gas Turbine Engines	16
2.1.1 Turbojet Engine	16
2.1.2 Turboprop engine	17
2.1.3 Turbofan Engine	19
2.1.3.1 Low bypass ratio Turbofans.....	20
2.1.3.2 High bypass ratio Turbofans	22
2.1.4 Turboshaft engine	23
2.2 Description of a Jet Engine Components	24
2.2.1 Air Intake	24
2.2.2 Compressor.....	26
2.2.2.1 Centrifugal Compressors	27
2.2.2.2 Axial Flow Compressor	29
2.2.3 Combustion Chamber	31
2.2.3.1 Can Combustion Chambers	33
2.2.3.2 Can-Annular Combustion Chambers	34
2.2.3.3 Annular Combustion Chambers.....	35
2.2.4 Turbines	35
2.2.4.1 Impulse Turbines	36
2.2.4.2 Reaction Turbines	37
2.2.5 Exhaust nozzle	38
2.2.5.1 Convergent Nozzles	38

2.2.5.2 Laval Nozzles.....	39
2.3 Thermodynamic Principles and Efficiencies.....	40
2.3.1 Thermodynamic Principles.....	40
2.3.2 Gas Characteristics and Engine cycle.....	44
2.3.3 The Engine Cycle	46
2.4 Fuel Characteristic and Systems	50
2.4.1 Ideal Fuel Properties and Characteristics	51
2.4.2 Fuel Types and Additives.....	53
CHAPTER 3	55
3.1 Experimental and numerical experimentation of Turbojet Engines.....	55
3.2 Experimentation of Alternative Fuels and Effects on Gas Turbine Emissions.....	58
3.3 Noise and Vibration Analysis for High Aromatic Fuels	63
CHAPTER 4	67
4.1 Overview	67
4.2 Numerical Modelling and Simulation.....	67
4.2.1 Turbulence Modelling	67
4.2.2 Combustion Modelling.....	70
4.2.3 Model and Mesh Development.....	72
4.2.4 Boundary Conditions.....	75
4.2.6 Solver Equipment and Procedures.....	80
4.3 Physical Experimental Setup and Procedure.....	80
4.3.1 Fuel Characterization Methodology	80
4.3.1.1 Brookfield Viscometer DV-II +Pro	80
4.3.1.2 Phase Technology JFA-70Xi AS	82
4.3.1.3 Shimadzu DTG-60.....	83
4.3.1.4 Malvern MIE Scattering He-Ne Laser.....	84
4.3.1.5 Petroleum Analysis Company CID 510.....	87
4.3.1.6 Parr 1341 Constant Volume Calorimeter.....	89
4.3.2 Experimental Methods Overview of the Turbojet Engine Fueled with Jet-A and F24	90
4.3.2.1 Gas Turbine Experimental Setup.....	90
4.3.2.2 Emissions Experimental Setup	92
4.3.2.3 Noise and Vibration Experimental Setup	94

4.3.3 Experimental Methodology and Data Processing	97
CHAPTER 5	99
DATA AND RESULTS ANALYSIS.....	99
5.1 Fuel Characterization	99
5.1.1 Overview	99
5.1.2 Viscosity and Density.....	99
5.1.3 Spray Distribution.....	101
5.1.4 Low Temperature Heat Release via Thermogravimetric and Differential Temperature Analysis	103
5.1.5 Combustion Properties Analysis	105
5.2 Numerical Simulation Results and Analysis.....	107
5.2.1 Numerical Simulation Overview	107
5.2.2 Numerical Engine Temperature.....	108
5.2.3 Numerical Engine Pressure	111
5.2.4 Numerical Engine Velocity	113
5.2.6 Numerical Engine Turbulent Kinetic Energy (TKE)	116
5.2.7 Numerical Engine Fuel Spray Analysis.....	117
5.2.8 Numerical Engine Emissions.....	118
5.3 Gas Turbine Experimentation Results.....	125
5.3.1 Experimental Engine Overview.....	125
5.3.2 Engine Temperature.....	125
5.3.3 Engine Pressure.....	128
5.3.4 Engine Thrust.....	130
5.3.5 Engine Fuel Flow	132
5.3.6 Engine Air-Fuel-Ratio and Equivalence Ratio	133
5.3.7 Engine Thrust Specific Fuel Consumption	135
5.3.8 Engine Emissions Analysis	136
5.3.9 Engine Noise and Vibration Analysis	140
CHAPTER 6	145
FINDINGS, CONCLUSIONS, AND RECOMMENDATIONS	145
6.1 Conclusions	145
6.2 Future Work	147
6.3 Special Thanks	148

REFERENCES	149
------------------	-----

LIST OF TABLES

Table 1: Boudary Conditions for the Numerical Simulations	77
Table 2: NASA Polynomial data of Jet-A and F24	78
Table 3: ASTM D78668-14a Standard Testing Parameter in the Constant Volume Combustion Chamber	88
Table 4: SR-30 Small-scale Turbojet Engine Specification	91
Table 5: Specifications for Microphones	94
Table 6: Kinematic Viscosity and Density	100
Table 7: Average Temperature and Mass Percentage (TA%) of Jet-A and F24	104
Table 8: Combustion Properties of Jet-A and F24.....	107
Table 9: Vibration properties of the engine with corresponding component frequency	142
Table 10: Temperature for the experimental and numerical simulation of Jet-A and F24.....	155
Table 11: Pressure for the experimental and numerical simulation of Jet-A and F24.....	156
Table 12: Engine Characteristic for the experimental and numerical simulation of Jet-A and F24	156
Table 13: Experimental emission results for Jet-A and F24.....	157
Table 14: Experimental TSFC emission results for Jet-A and F24	157
Table 15: SPL for Jet-A and F24 at each engine speed	157

LIST OF FIGURES

Figure 1: Basic Function of a turbojet engine.(Administrators 2023).....	16
Figure 2: J85 FE 17A turbojet engine (Acharya 2008).....	17
Figure 3: Schematic of the components of a turboprop jet engine (Malar 2012).	18
Figure 4:General Electric turboprop engine developed by G.E. Aviation Czech (Praga 2016)...	19
Figure 5: GE9X high bypass ratio turbofan engine (ArkSolo 2017).	20
Figure 6: Schematic of a low bypass ratio turbofan engine (Academic 2023).	21
Figure 7: GE Affinity SST turbofan for Aerion AS2 (Economics 2018).	22
Figure 8: Schematic of a high bypass ratio turbofan engine (Anna Snakowska 2008).	23
Figure 9: Schematic of a turboshaft engine (Ohad Gur 2023).	24
Figure 10: Pressure and temperature as a function of position in the turbofan engine (Sturesson 2018).....	26
Figure 11: Centrifugal compressor with impeller, diffuser, compressor manifold (Hunecke 1997).	28
Figure 12: Two stage centrifugal compressor(left) and a double entry centrifugal compressor (right) (Mind 2024).....	29
Figure 13: The rotor and stator of an axial flow compressor (Baskharone 2006).	30
Figure 14: Basic schematic of an combustion chamber (Nemeth 2017).	32
Figure 15: Can style combustion chamber flow pattern (left) and diagram (right) (Notes 2021).	34
Figure 16: Flow pattern (left) and a diagram (right) of a can-annular combustion chamber(Notes 2021).	34
Figure 17: Flow pattern (left) and diagram (right) of an annular combustion chamber (Notes 2021).....	35
Figure 18: Reaction turbine (right) compared to an impulse turbine (left)(Administrators 2017).....	37
Figure 19: Subsonic converging exhaust nozzle (flight-mechanic 2023).....	39
Figure 20: A converging nozzle (left) and a Laval (converging-diverging) nozzle (right) (flight-mechanic 2023).....	40
Figure 21:Comparison between reciprocating and gas turbine engine cycle (mechanical-engg 2023).	47
Figure 22: Brayton Cycle.....	48
Figure 23: Enthalpy-Entropy	48
Figure 24: SolidWorks model of the scaled Turbine Technologies turbojet engine.	73
Figure 25: Final SolidWorks model of the turbojet engine.	74
Figure 26: Numerical mesh for the final engine (top left and top middle), injector (top right) and cross-sectional view(bottom).....	75
Figure 27: Boundary Conditions for the numerical models.....	76
Figure 28: Plane of data collection for the numerical simulation.	79
Figure 29: Data collection points for numerical and experimental comparison.	79
Figure 30: Brookfield DV-II +Pro Rotational Viscometer (Grall 2021)	81
Figure 31: JFA-70XI AS 3-in-1 Jet Fuel Analyzer (Gordon Chiu 2018).....	83
Figure 32: Shimadzu DTG-60 ((Shimadzu 2023)	84

Figure 33: Malvern Spraytec with Mie & Fraunhofer Scattering, He-Ne Laser Experimental Setup (Valentin Soloiu 2024).....	86
Figure 34: Constant Volume Combustion Chamber Schematic (Valentin Soloiu 2024)	88
Figure 35: Parr 1341 Calorimeter with cross-sectional schematic(Parr_Instrument_Company 2021, 2014)	90
Figure 36: Location of each temperature and pressure sensor in the turbojet engine (Turbine_Technologies 2011).....	92
Figure 37:Emissions Experimental Setup	94
Figure 38: Microphone layout in the experimental setup.	95
Figure 39: Location and orientation of the Triaxial Accelerometer	96
Figure 40: Noise and vibration data collection experimental setup.....	97
Figure 41: Dynamic Viscosity vs Time for Jet-A and F24	100
Figure 42: MIE Scattering Laser Droplet Volume Frequency for Jet-A and F24	101
Figure 43: MIE Scattering Laser Sauter Mean Diameter for Jet-A and F24	102
Figure 44: Thermogravimetric Analysis of Jet-A and F24	103
Figure 45: Differential Temperature Analysis of Jet-A and F24.....	104
Figure 46: AHRR results for Jet-A and F24	105
Figure 47: Average Pressure release for Jet-A and F24	106
Figure 48: <i>Temperature contours of Jet-A and F24 at each investigated engine speed.</i>	109
Figure 49: <i>Isometric and Front view of the temperature contour for F24 at each engine speed.</i>	110
Figure 50: Pressure contours for the numerical simulation of Jet-A and F24	112
Figure 51: Velocity contours for the numerical simulation of Jet-A and F24	114
Figure 52: Velocity streamlines for the numerical simulation of F24.....	115
Figure 53: Turbulent kinetic energy for the numerical simulation of Jet-A and F24	116
Figure 54: Fuel Spray Mass Fraction for the numerical simulation for Jet-A and F24	118
Figure 55: Water Vapor emissions from the numerical simulation of Jet-A and F24.....	119
Figure 56: Carbon Dioxide emissions from the numerical simulation of Jet-A and F24	121
Figure 57: Carbon Monoxide emissions from the numerical simulation of Jet-A and J24	122
Figure 58: Nitrogen Oxides emissions from the numerical simulation of Jet-A and F24	123
Figure 59: Oxygen mass fraction results from the numerical simulation of Jet-A and F24.....	124
Figure 60: Turbine Temperature at each data collection point in the engine for both experimental and numerical simulation at each engine speed.	126
Figure 61: Turbine Pressure at each data collection point in the engine for both experimental and numerical simulation at each engine speed.....	129
Figure 62: Turbine Thrust for both experimental and numerical simulation at each engine speed.	131
Figure 63: Turbine Fuel Flow rate for both experimental and numerical simulation at each engine speed.	132
Figure 65: Turbine AFR for both experimental and numerical simulation at each engine speed.	133
Figure 66: Turbine Equivalence ratio for both experimental and numerical simulation at each engine speed.....	134

Figure 67: Turbine Thrust specific fuel consumption for both experimental and numerical simulation at each engine speed.....	135
Figure 68: Average H ₂ O and CO ₂ Percentage for Jet-A and F24	136
Figure 69: Average CO and THC PPM for Jet-A and F24.....	137
Figure 70: Average NO _x PPM for Jet-A and F24	138
Figure 71: Thrust Specific H ₂ O and CO ₂ percentage emissions for Jet-A and F24.....	139
Figure 72: Thrust Specific CO, THC, and NO _x PPM emissions for Jet-A and F24	140
Figure 73: Experimental setup for the noise, vibration, emissions, and gas turbine testing.....	155
Figure 74: Vibration results for Jet-A and F24 at 60,000RPM.....	158
Figure 75: Vibration results for Jet-A and F24 at 65,000RPM.....	159
Figure 76: Vibration results for Jet-A and F24 at 70,000RPM.....	159
Figure 77: Sound Pressure results from the Multifield microphone for Jet-A and F24 at 60,000RPM.	160
Figure 78: Sound Pressure results from the Multifield microphone for Jet-A and F24 at 65,000RPM.	161
Figure 79: Sound Pressure results from the Multifield microphone for Jet-A and F24 at 70,000RPM.	161
Figure 80: Sound Pressure results from the Freefield microphone for Jet-A and F24 at 60,000RPM.....	162
Figure 81: Sound Pressure results from the Freefield microphone for Jet-A and F24 at 65,000RPM.	162
Figure 82: Sound Pressure results from the Freefield microphone for Jet-A and F24 at 70,000RPM.	163

CHAPTER 1

INTRODUCTION

1.1 History of Gas Turbine Engines

The development of the gas turbine engine has been fundamental for the progression of modern-day aviation and power generation. The most basic of the principles used in jet engines, propulsion, was development and introduced to the world by the Chinese as early as the 13th century with rockets propelled via gunpowder. The study of this basic principle led to further development of what is known today as the modern gas turbine engine.

The modern-day gas turbine engine was developed through centuries of both purposeful and unknowingly brilliant investigations into the principles of physics known as fluid mechanics, thermodynamics, and combustion. This began in the 1500's with an invention developed by Leonardo da Vinci (Hunecke 1997, 1). His invention used hot air to rotate a turbine which turned a barbeque spit. This rudimentary device used the fundamental principle still used in high RPM gas turbine engines today. Another major development of these basic principles was the work of Isaac Newton, specifically the third law. This law states that for every force acting on a body, there is an equal and opposite reaction exerted by the body against the force. For jet engines, this force (also known as the thrust) is exerted out the back of the engine, propelling the body forwards. Modern day gas turbine engines were developed from these simple principles.

Near the turn of the 19th century, John Barber received a patent for a steam powered turbine engine. This engine mixed air and gas into a combustible mixture. Once compressed, the mixture would flow into a combustion chamber. This hot gas would flow over a turbine, producing rotation that would, in theory, cycle the reciprocating compression stage as well as provide mechanical work that could be translated to drive an axle. Although a working model was never produced due to the insufficient materials at the time, this concept is considered the beginning of modern-day gas turbine engines (Hunecke 1997, 2). This patent

was further expanded on by John Bumbell in 1808, which used a similar design. Instead of a reciprocating piston compressor, this design compressed air with rotating turbine blades, much like what is used in modern compressor stages. However, this design lacked stators, losing the advantages seen in multistage compressors (Wild 2018, 301). The beginning of World War I instigated a more fervent investigation into the use of gas turbine engines. Sanford Moss, through General Electric (G.E.) developed an exhaust turbocharger for reciprocating aircraft engines in 1918. This development was the first use of a gas turbine in the aviation industry.

As further development of gas turbines was conducted, the advantage of these engines possessed was quickly seen for application in the aerospace and power generation industry. In 1930, the first gas turbine engine, fully equipped with an axial and centrifugal compressor, annular combustion chambers located radially around the engine, and a single turbine was developed for investigation into propulsion. This engine was developed by Frank Whittle of Great Britain and ran using liquid fuel. Following this development, in 1939, a German company (Heinkel) developed a gasoline burning gas turbine engine. This would be what is now known as a turbojet engine and is significant because it was the first gas turbine engine used in flight. This engine propelled a Heinkel He 178 jet aircraft and produced 5000N (1100 lb) of thrust with a weight of 360 N (795 lb.)(Wild 2018, 301, Hunecke 1997, 2-3). Over the course of the 20th century, this development was followed by an increase in design effectivity and efficiency. Different companies, including Rolls Royce in Great Britain, the Bell Aircraft Cooperation and General Electric in the United States, and Messerschmitt of Germany continued to produce and improve the jet engine market. Over time, these developments lead to the modern day high thrust jet engines being owned and operated across the globe.

1.2 Purpose of Study

This study seeks to combine the most valuable components of numerical and experimental testing to develop models and enhance the understand of relationships between the fuels used in turbojet engines

and their properties. These fuel properties have been examined using in-house state of the art equipment in Georgia Southern Universities Combustion Research Lab. By combining these measured physical properties with thermochemical data collected from outside academic institutions, a surrogate F24 fuel can be developed and implemented in a computational fluid dynamic (CFD) model. Furthermore, by using an existing CFD model created for Jet-A and implementing the F24 surrogate fuel, a numerical model can be generated and then validated with the use of experimental testing via an instrumented small-scale turbojet engine. With the numerical F24 model validated against experimental data, the turbulent phenomenon inside the turbojet engine (namely the combustion chamber and exhaust sections) can be analyzed and understood. This provides an opportunity to better understand the turbulence behavior of the air and gas inside the engine, provides valuable knowledge on the flame front characteristics of F24 as compared to Jet-A, and allows for an in depth examination of the combustion phenomena inside the combustion chamber.

Furthermore, emission production of F24 and Jet-A can be compared using experimental data. The numerical model will allow for a better understanding of the formation process of harmful greenhouse emissions like CO₂, CO, NO_x, H₂O, and other important gases produced from the combustion process. The turbulent behavior and combustion efficiency can then be correlated to the production of these emissions, providing further information that experimental data rarely provides. Finally, the noise and vibration of F24 as compared to Jet-A can be examined through experimental means to evaluate the effect of physical, chemical, and molecular composition of each fuel on the vibration and sound produced from experimental testing.

The experimentation as described in this study is a focal point for many companies using gas turbines, organizations with a focus on reducing greenhouse emissions, and even the modern consumer. The increase of greenhouse gases, especially but not limited to the Industrial Revolution era, has led to measurable, negative effects on the environment. Therefore, to reduce individual and organizational carbon footprints, there has been a large trend towards the development of more fuel-efficient and less harmful

emissions produced by gas turbines. Not only is the environmental impact of jet engines important, but similarly important is the cost associated with the testing of engines. Despite the size of the engine, jet engines are costly to test. This cost can be seen not only in a financial strain but also through an environmental lens. The cost of natural, biological, and synthetic fuels can be costly for companies. The maintenance and development of existing and prototype engines also involves a very high financial cost. By generating a working numerical simulation, this study could potentially save companies from financial cost by reducing the maintenance required on current jet engines from the various operation of the engines. It could also benefit financial costs through the development of new engines. By using a numerical simulation to test the engine, companies can bypass the expensive process of manufacturing a jet engine. This has dramatic environmental and financial cost-saving benefits.

1.3 Statement of Hypothesis

By implementing combustion and thermophysical property data for F24 fuel conducted both in-house and through external laboratories, the model Jet-A fuel library properties can be adjusted to create a surrogate F24 fuel and implemented in numerical CFX combustion simulations to validate the numerical model through the use of engine performance data.

CHAPTER 2

LITERATURE REVIEW

2.1 Types of Gas Turbine Engines

There are four main types of gas turbine engines that have been used predominately in aircraft travel. These types are turboprop, turboshaft, turbojet, and turbofan. Each type is used in a different application. These different applications dictate the transfer of power throughout the system and have offered unique improvements to aircraft travel since the development of the reciprocating aircraft engine. However differently, each engine utilizes the same components throughout the system. These components are the inlet, compressor, combustion chamber, and the turbine.

2.1.1 Turbojet Engine

The turbojet engine was the original jet gas turbine used for aero propulsion. This jet engine utilizes the air coming from the intake. This air then proceeds through a compressor stage where it experiences a dramatic rise in pressure and temperature, preparing it for combustion. This conditioned air is then ignited in the combustion chamber.

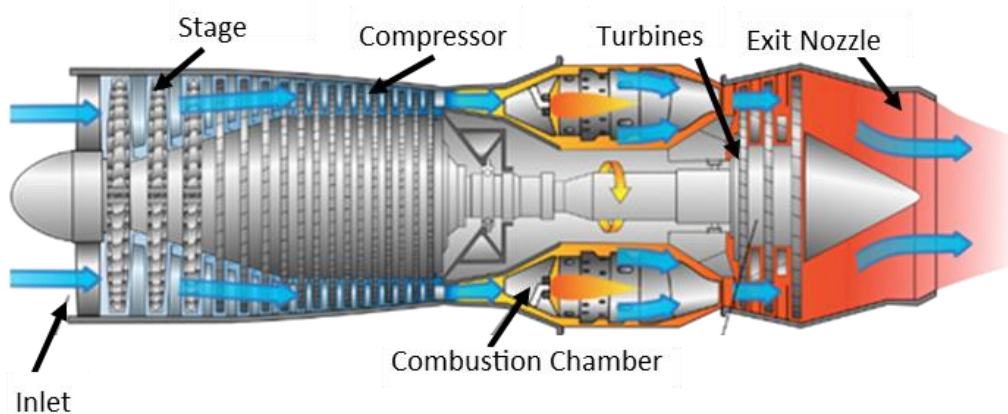


Figure 1: Basic Function of a turbojet engine.(Administrators 2023)

From the combustion chamber, the flow is axially forced into the turbines. These turbines convert the hot gas energy into mechanical energy in the form of rotation. This rotation is applied to a shaft that

rotates the preceding compressor rotors or impellers. It also powers any auxiliary components. Finally, the remainder of the energy of the hot gas is converted into kinetic energy in the form of velocity. This high velocity flow exits the turbine through the exhaust nozzle, which uses either converging nozzles or converging-diverging nozzles to accelerate the flow. A schematic of a turbojet engine can be seen in Figure 1, and shows the general layout of an axial flow multistage turbojet engine.

These engines have been used since the 1950's and created major domination for the US Airforce and can even be found in some military today. However, since the development of the turbofan engine, these engines are currently generally limited to military application (Wild 2018, 302, Hunecke 1997, 2-3). This is the type of engine used in this research. Figure 2 shows a J85 GE 17A turbojet engine.

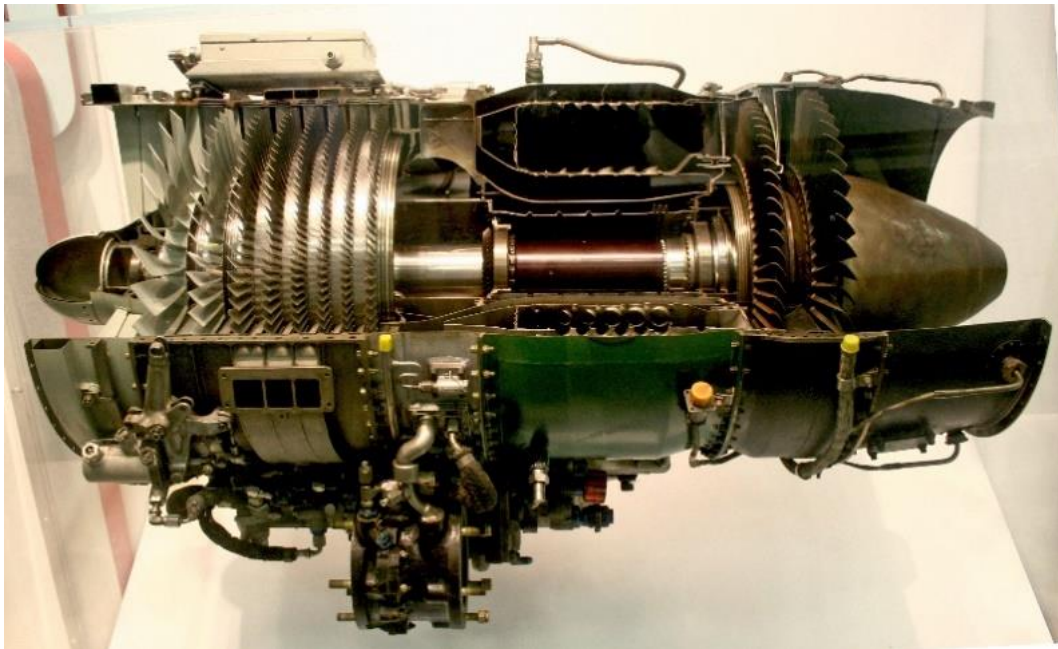


Figure 2: J85 FE 17A turbojet engine (Acharya 2008).

2.1.2 Turboprop engine

Simply put, a turboprop is a gas turbine engine used to turn a propeller at the front of the engine. This engine uses a two-spool rotary shaft to turn two separate turbines. One turbine(s) is used to rotate the

compressor stage while another turbine(s) is used to rotate the propeller. The rotation of this shaft, however, moves at an rpm that is not ideal for the most efficient rotation of the propeller. Therefore, a gear reduction is utilized between the two components to lower the rotations per minute down to an optimized level for the propeller. Due to the function of a turboprop engine, most of the energy of the hot gas exiting the combustion chamber is converted into rotational energy to power the propeller. Approximately 10% of the energy from the hot gas is utilized for the exhaust thrust. The remaining 90% is extracted by the turbine (Wild 2018, 303). A schematic a turboprop engine can be seen in Figure 3.

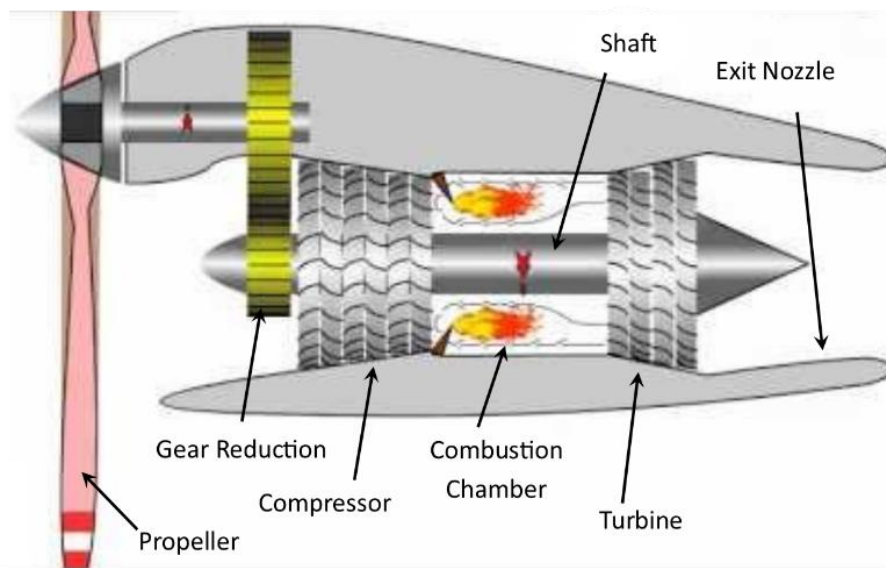


Figure 3: Schematic of the components of a turboprop jet engine (Malar 2012).

One main difference between turboprop engines and the remainder of the turbo family is in the usage of the air. Turbojet engines take low air mass flow from the intake and convert it into high velocity exhaust. Turboprops, however, take high air mass flow and convert it to low velocity. This difference can be seen in the performance (Hunecke 1997, 4-6). Turbojets operate for the purpose of high thrust and reduced noise; however, fuel efficiency suffers under these conditions.

Turboprop engines have incredible fuel efficiency when compared to turbojet engine, but likewise suffer from a high noise pollution and operate at much lower speeds (Hunecke 1997, 6-8). Figure 4 shows a General Electric turboprop engine developed by G.E. Aviation Czech.

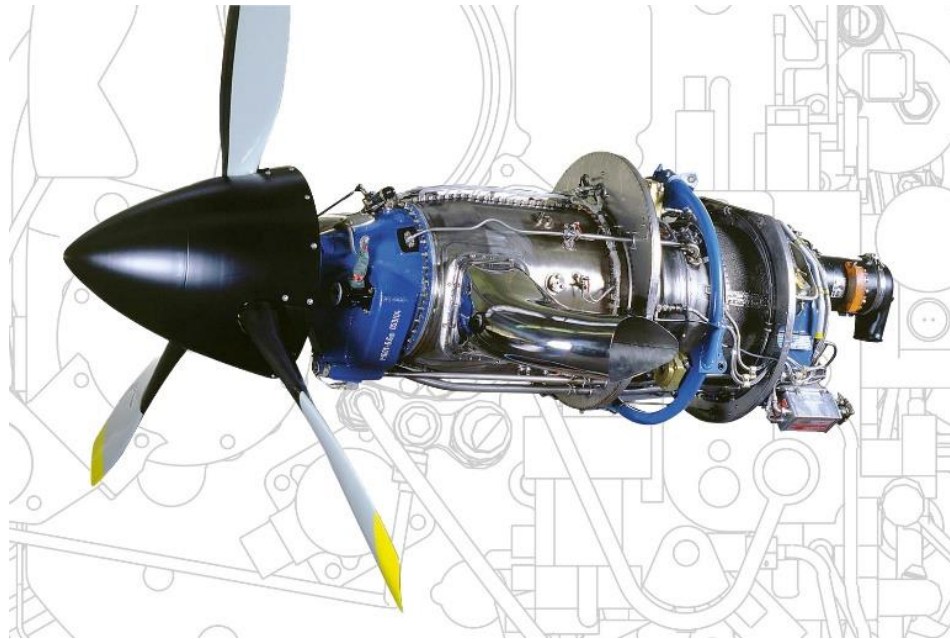


Figure 4: General Electric turboprop engine developed by G.E. Aviation Czech (Praga 2016)

2.1.3 Turbofan Engine

The turbofan was produced as a cross between the turbojet and the turboprop. Whereas a turboprop uses gas generator (compressor, combustion, and turbine) to rotate a large front propeller to produce a majority of the thrust, the turbofan uses the large front propeller as a compressor stage to utilize thrust from both the bypassed cold air and that which is generated from the gas generator. The turbofan bypasses a certain percentage of the mass of the incoming air through a duct that moves around the inter core of the engine. This bypassed cold air attributes approximately 80-85% of the entire thrust produced by the engine (Wild 2018, 303). This percentage of bypassed cold air is also known as the bypass ratio. Depending on the bypass ratio, turbofan engines can be used for a wide variety of applications. Figure 5 shows an example of a turbofan engine used for commercial flights.

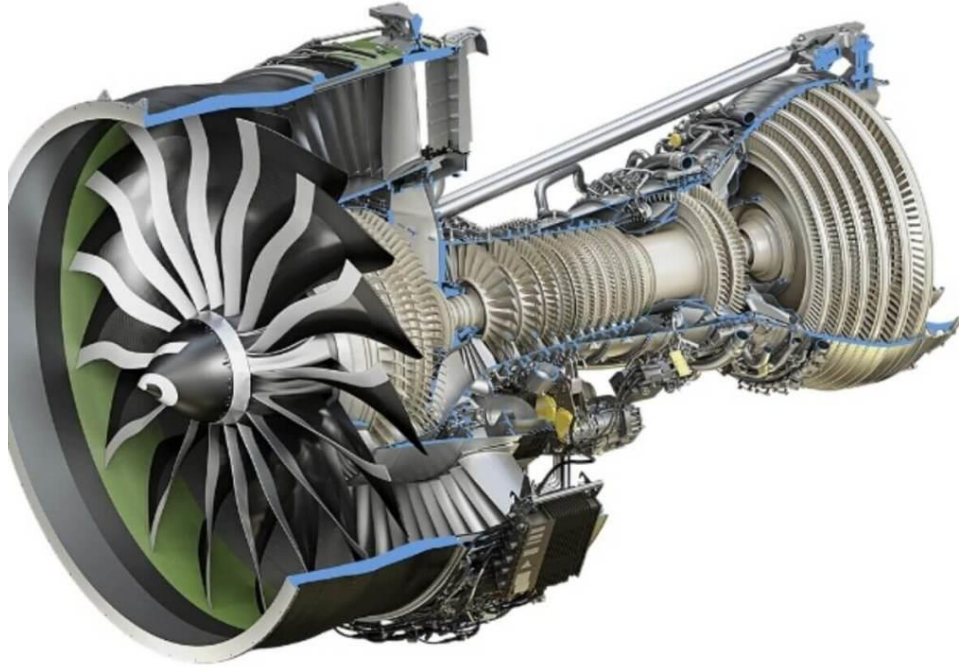


Figure 5: GE9X high bypass ratio turbofan engine (ArkSolo 2017).

2.1.3.1 Low bypass ratio Turbofans

Low bypass ratio turbofans are turbofan engines that bypass between 20% and 100% of the air mass that passes through the core. This can also be viewed as 5% to 50% of the total air that passes through the entire engine (Hunecke 1997, 10-13). These types of engines consume less fuel with the same amount of thrust when compared to turbojet engines. A schematic of a low bypass ratio turbofan engine can be seen in Figure 6.

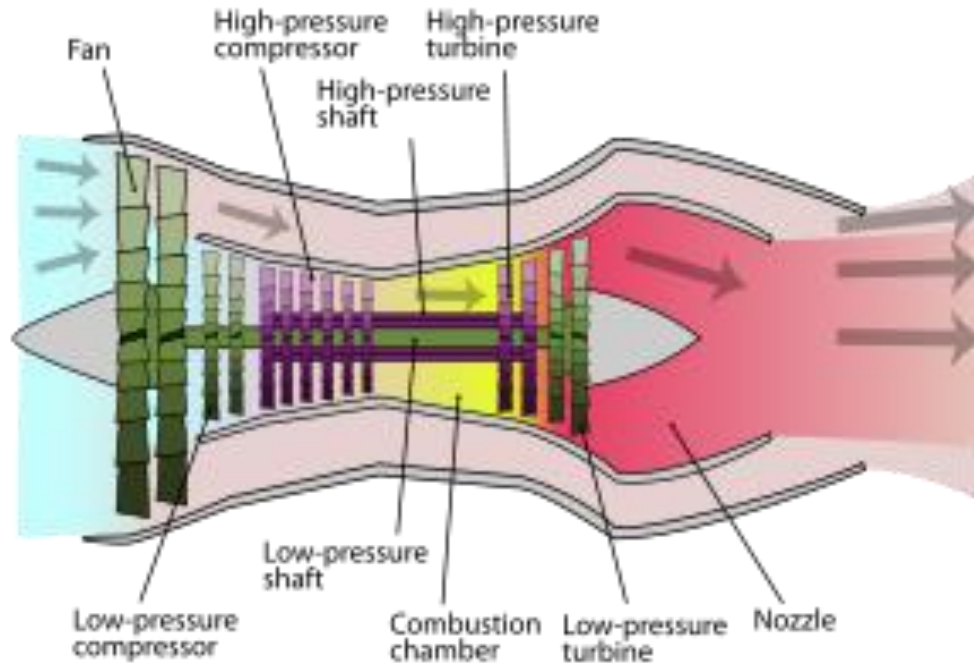


Figure 6: Schematic of a low bypass ratio turbofan engine (Academic 2023).

These engine types are not as fuel efficient and as a high or ultra-high bypass, nor do they offer acceptable ranges of noise levels as compared to today's commercial airlines (Hunecke 1997, 10). However, these engines are still used in high subsonic, large range combat fighters. A low bypass turbofan engine can be seen in Figure 7.

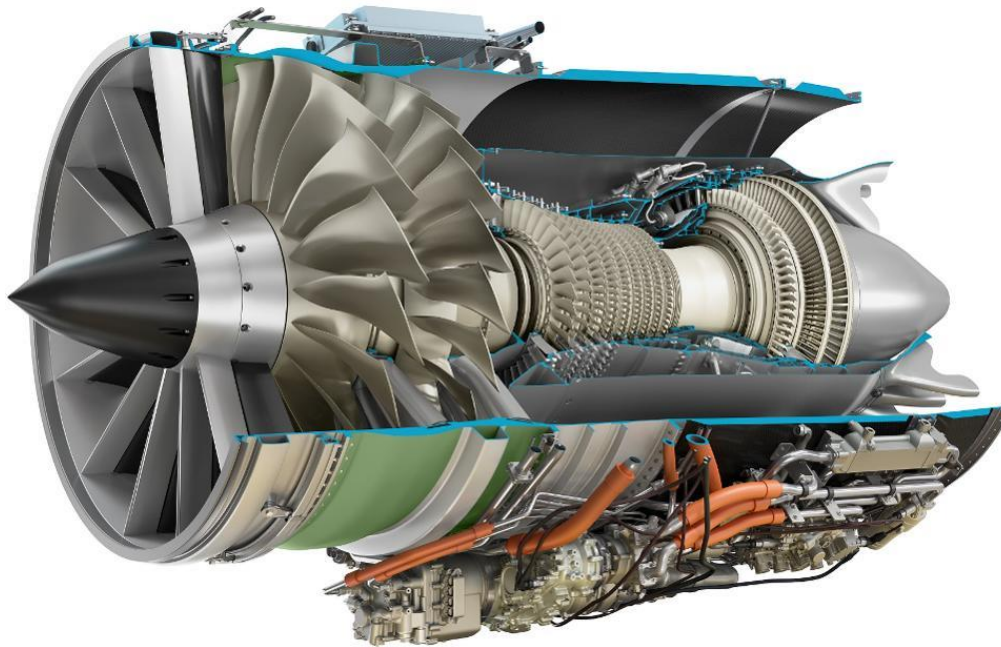


Figure 7: GE Affinity SST turbofan for Aerion AS2 (Economics 2018).

2.1.3.2 High bypass ratio Turbofans

High bypass ratio turbofan engines, contradictory to low bypass engines, operate at much lower speeds and have a much better fuel efficiency and reduced noise levels (Hunecke 1997, 15-16). These engine types have been adopted in many industries, predominately in commercial flight. However, some are also used for long-range military transport aircraft. This distinction is due to the bypass ratio. High bypass ratio engines typical operate in ratio's up to 5:1 and 6:1 (Wild 2018, 303). A schematic of a high bypass turbofan can be seen in Figure 8.

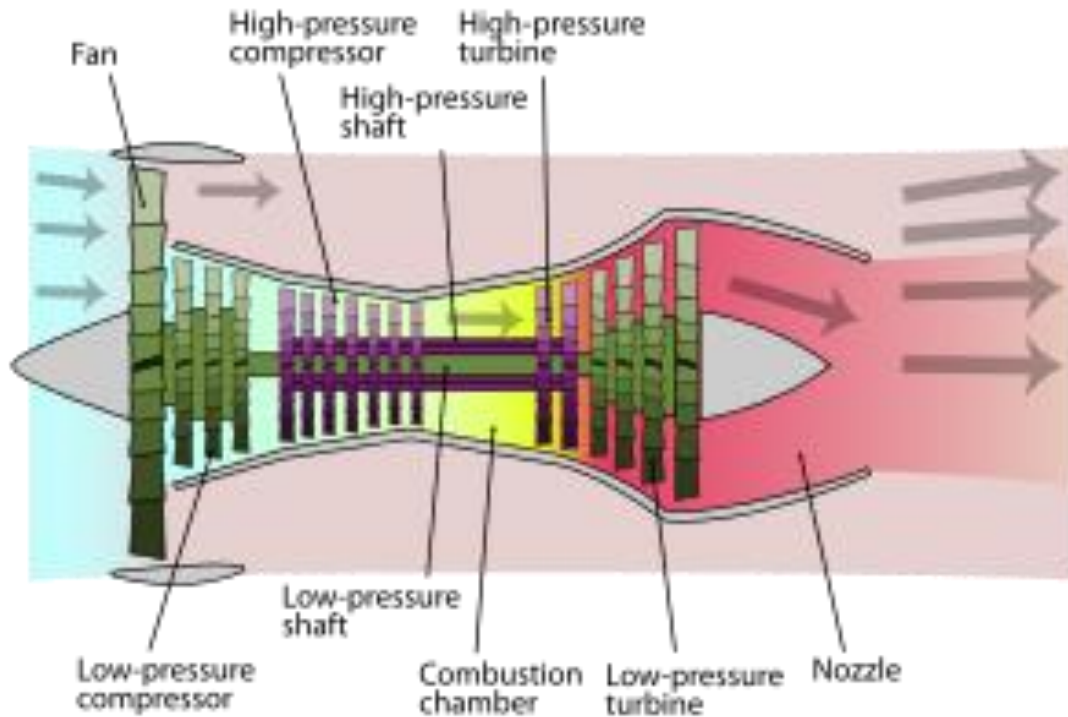


Figure 8: Schematic of a high bypass ratio turbofan engine (Anna Snakowska 2008).

An extension of the high bypass turbofan, the ultra-high bypass engine have bypass ratios in the scale of 10:1. These engines utilize new technological advances in fan blade design to operate at higher fuel efficiencies and high speeds (Wild 2018, 303).

2.1.4 Turboshaft engine

A turboshaft jet engine differs from the previous three in purpose but is most similar to the turboprop. Turboshaft engines utilize a gas generator to create shaft horsepower, which rotates a gear transmission system or is used for electricity generation.

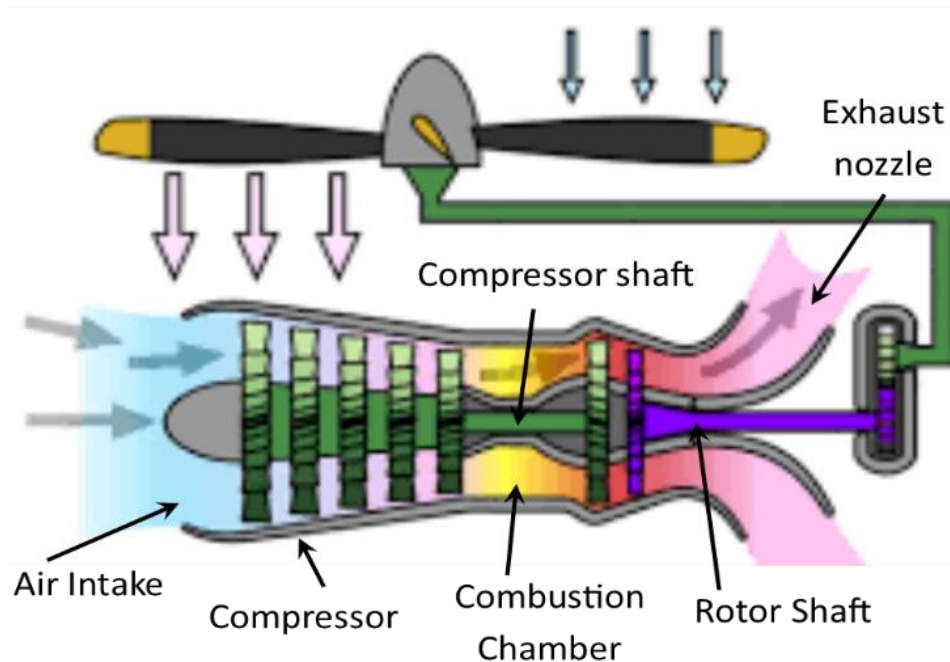


Figure 9: Schematic of a turboshaft engine (Ohad Gur 2023).

Turboshaft engines are commonly used for helicopter rotors and auxiliary power units inside large aircraft (Wild 2018, 303). Special classes of turboshaft engines have specific uses separate from aviation. These engines can be used for power generation by different industries as well as tanks and ship engines (Hunecke 1997, 21-22). The exhaust for these engines exits through an exit nozzle and generates no useful thrust. A schematic of a turboshaft engine can be seen in Figure 9.

2.2 Description of a Jet Engine Components

2.2.1 Air Intake

There are several different components that comprise a functioning turbo gas turbine engine. The first of the multiple sections is the inlet. Although it is not considered as a part of the engine, inlet is a crucial section of the engine due to the requirements of air breathing internal combustion engines. The air that is pulled into the turbine must be properly conditioned to ensure the best possible performance of the engine. The purpose of the air intake is to produce a high-quality flow that is laminar and uniform to reduce the energy loss due to the ram effect as well as drag forces (Wild 2018, 304). There are other structural

requirements of the intake, such as housing the forward bearings for the compressor, however the orientation of the flow is of the utmost importance regarding thrust production and fuel efficiency. This can be accomplished with the use of guide vanes.

Since the air intake is a component of the nacelle and not a part of the engine, engine manufacturers create engines that require specific air flow rates. These requirements must be met by the aircraft company. Considering this fact, there are many arrangements of air intake cross sections depending on the functionality of the aircraft. For aircraft like cargo and civil passenger planes, the intakes may be circular, while for subsonic military jets, they may be half circular, elliptical, or irregular in the cross section depending on application. The air intake of all aircraft utilizes a round lip of the intake to reduce the flow separation and decrease drag forces experienced by the aircraft. Although most effectively implemented in subsonic vessels, high speed aircraft requires a thin lip, and must reduce the radius of the lip (Hunecke 1997, 49).

One of the most important stages of life for an air intake for subsonic engine, as used in this experiment, is the take-off stage. This low velocity flow can be highly impacted by the surroundings, including the location of the engine, environmental concerns like crosswinds and ground vortexes, and location of the surrounding aircraft components. Crosswinds are especially dangerous at high speeds due to their capability to destroy fan blades. This is possible due to the flow separation caused between the lip and the blades of the fans. This flow separation causes an increase in the drag force, which when applied to the fans, may break the fans (Hunecke 1997, 50).

A big concern regarding the air intake is the icing of the intake. At high speeds, ice may form on the lip or the guiding vanes of the intake. These large pieces of ice negatively affect the engine, inhibiting the flow of air into the engine, decreasing the thrust, and increasing the exhaust gas temperature (EGT). This change in thrust is compensated for by the fuel system, injecting more fuel into the combustion chamber and increasing the inlet turbine temperature. Modern day engines counter these issues by using warm compressed air from the compressor and bleeding it into the ducts of the intake. This must be used

during the entirety of the flight if icing is expected and can lead to a 30% decrease in loss of thrust. Centrifugal compressors, as is used in the experiment, does not experience an icing effect (Wild 2018, 305).

2.2.2 Compressor

The next section of the turbo engine is the compressor. The compressor's main purpose is to increase the pressure of the air using the mechanical work supplied by the turbine section. This increase in pressure is accompanied by a corresponding decrease in velocity. Due to the direct relationship between pressure and temperature, this also causes an increase in the temperature of the air, as seen in Figure 10.

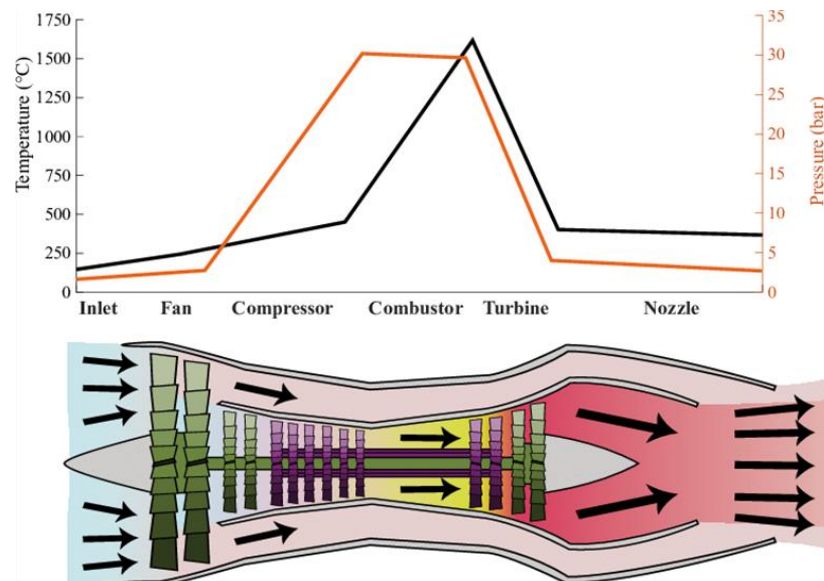


Figure 10: Pressure and temperature as a function of position in the turbofan engine (Sturesson 2018)

Each component works to bring the air to an ideal state for the most efficient combustion. There are several important factors in considering a compressor. The efficiency of a compressor is described as the machine's ability to convert the most mechanical work of the turbine into pressure energy. Most turbines can deliver efficiency levels of around 80%-90% depending on the style of compressor (Hunecke 1997, 87). The compression ratio is another important factor of the compressor. The compression ratio is the attainable increase in pressure from the atmosphere level in the compressor intake to the resulting pressure

in the compressor exit. This ratio can be determined by use of the equation below, where the compression ratio is represented by **Error! Reference source not found.**

$$\Pi = \frac{P_{C2}}{P_{atm}} \quad \text{Eq. 1}$$

This ratio is of incredible importance because higher pressure ratios affect the thrust, engine weight, fuel efficiency, and engine efficiency. This can be seen by examining the properties of the combustion process. Higher pressure ratios allow more air to be pushed into the combustion chamber at once, which improves the combustion, and produces greater thrust. Modern day engines typically use compression ratios around 16:1, where larger engine, like ultra-high bypass turbofans, can generate up to 30:1 pressure ratios (Hunecke 1997, 87). Another important use of the compressor is the air flow rate. The amount of air forced through the compressor is generally affected by the rpm of the turbine, the forward speed of the aircraft, and the density of the incoming air (Wild 2018, 305). These values of compressors typically denote the engine sizes, where larger engines like turbofans, intake a larger volume of air than turbojet engines. Many engines intake approximately 200 kg/s of air, which larger engines intaking as high a 900 kg/s (Hunecke 1997, 87).

There are two main types of compressors used in the market for jet engines. These include centrifugal and axial compressors.

2.2.2.1 Centrifugal Compressors

Centrifugal compressors were used up until the 1950's in many jet engines. These compressors get their name from the method in which they convert mechanical energy of the turbine shaft into pressure energy. These compressors use centrifugal forces to convert the mechanical work of the turbine shaft to pressure energy. Centrifugal compressors are comprised of three main components: The impeller, diffusor, and manifold, all of which are picture in Figure 11.

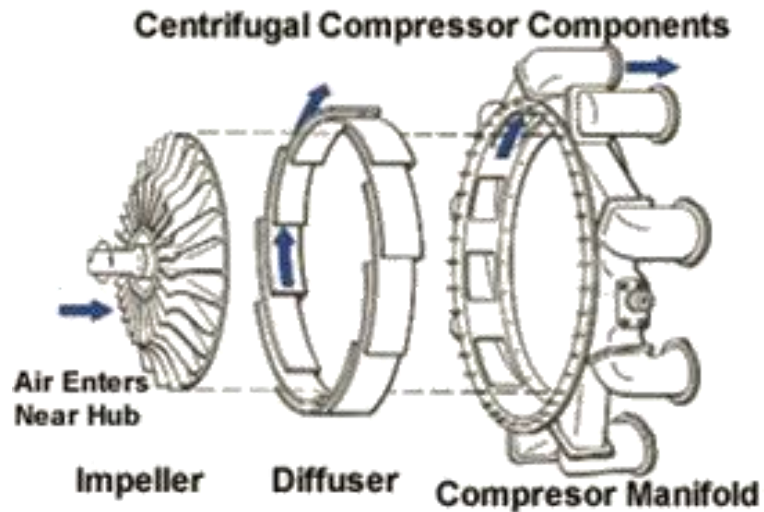


Figure 11: Centrifugal compressor with impeller, diffuser, compressor manifold (Hunecke 1997).

Air enters the impeller at the smaller radius. As the air is drawn in, the pressure is increased, and the impeller pushes the air outward radially, increasing the velocity of the air. This increase in velocity results in a proportionate increase in kinetic energy. As the air moves through the diffuser, this kinetic energy is converted into pressure energy. The impeller and diffuser both do approximately one-half of the total pressure increase in the system (Hunecke 1997, 89). The diffuser also works to properly orient the flow as it exits the impeller. These compressors can be used in stages, using either two, oriented in one direction with one following the other, or can be a double entry compressor, which allows air entry from both the front and back. These can be compared by examining Figure 12.

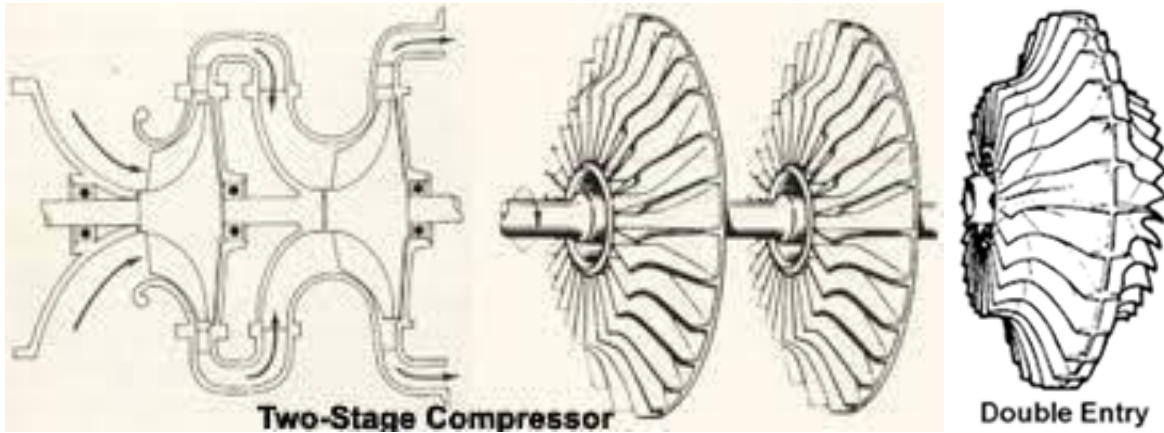


Figure 12: Two stage centrifugal compressor(left) and a double entry centrifugal compressor (right)

(Mind 2024)

The centrifugal compressor has several advantages, including the high-pressure ratio per stage which is approximately 5:1. This can be further taken advantage of by introducing two stages as seen in Figure 12. This, however, does introduce an added weight due to the ducts required to re-orient the flow, as well as the added complication of flow separation in the ducts (Hunecke 1997, 89). It also has the advantage of being more cost efficient, due to the simplicity in manufacturing. Depending on the implementation, these compressors can also have a good efficiency (80%), have a reduced weight (as compared to axial flow) and require less starting power. There are several disadvantages as well, including the lower efficiency at higher rpms, and a larger frontal area for a given air flow, leading to more drag (Hunecke 1997, 88-89, Wild 2018, 305)

2.2.2.2 Axial Flow Compressor

Axial flow compressors were developed by the Germans during WWII and dominated aviation warfare. While centrifugal compressors use centrifugal forces to increase pressure, axial flow compressors take advantage of aerodynamic forces to increase pressure. Axial compressors main advantage is the amount of air that can be introduced through the compressor (Wild 2018, 306, Hunecke 1997, 93-94). These higher mass flow rates are directly equivalent to the increases in thrust that can be attained by axial flow

compressor engines. These compressors use a series of aerodynamic blade stages known as rotors and stators. Stators are generally attached to the outer casing of the compressor. The purpose of the stators is to orient the flow as it is pushed past the rotor. The rotors are rotated by the turbine shaft. This rotation forces air into the engine and increases the pressure of the air. This can be seen in Figure 13.

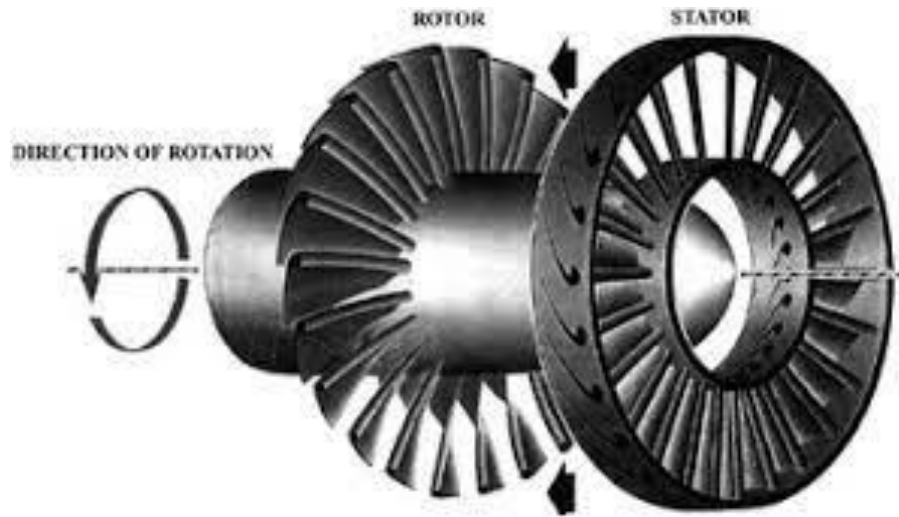


Figure 13: The rotor and stator of an axial flow compressor (Baskharone 2006).

While individually, these rotors and stators produce much less compression ratio (1.2-1.3) than centrifugal compressors, they have the advantage of using as many stages as the developer determines is necessary. However, these increase in stages are accompanied by an increase in weight, which is the reason axial flow compressors are much heavier than centrifugal compressors (Wild 2018, 305). This weight addition is negligible in comparison to the excess thrust that is developed. This thrust comes from the increased mass flow rate of the compressor. Axial flow compressors have much smaller cross-sectional areas with the same mass flow rate as centrifugal compressors. This reduces the drag forces experienced. Another advantage of axial compressors is the singular orientation of the air. Where centrifugal compressors must change the direction of the flow, axial compressors send air in a single direction axially down the engine. This leads to less energy loss from changing direction of the flow and higher ram efficiency. Some

issues that persist axial compressors are the high manufacturing cost, high starting power requirements, and more narrow range of efficiency in terms of rpm (Wild 2018, 305).

2.2.3 Combustion Chamber

The combustion chamber follows the diffuser in the core of the gas turbine engine. The combustion chamber is responsible for delivering energy into the system in the form of heat energy that is derived from a chemical reaction between a fuel and the air coming into the system. There are many variables that affect the combustion chambers performance, including fuel characteristics, combustion efficiency and flight conditions. The fuel used for combustion ideally optimizes density (and therefore weight) and the heating value or lower calorific value (LCV) to reduce the weight added by the fuel and increase the possible amount of energy that can be extracted. Another consideration of this is the combustion efficiency. All fuels have a total possible energy extraction value. This value is never practically reached. The practical amount of energy extracted from combustion of the fuel can be represented by the combustion efficiency which can be seen below.

$$\eta_{\text{eff}} = \frac{Q}{Q_0} \quad \text{Eq. 2}$$

In this equation, Q is the amount of energy released from combustion, and Q_0 is the theoretical energy available from combustion. Modern day engine are able to achieve a combustion efficiency in the range of 90% to 98% (Hunecke 1997, 128). The flight conditions are also very important in the case of the combustion chamber. The altitude of the flight corresponds to a decrease in pressure and temperature, neither of which are desirable for combustion. However, this increase in altitude also affects the density of the air, which is increased at colder temperature, and decreased at lower pressure. The velocity of the flow as it enters the chamber is another consideration. Air enters the compressor at around 150 m/s. It must be reduced to several meters per second to achieve the velocity for a combustible flow (Hunecke 1997, 125).

High compressor exit velocity will make combustion more difficult, requiring a richer mixture. This also contains the possibility of a flame out, where the flame is extinguished.

The airflow within the combustion chamber is another factor that must be taken into account when designing a combustion chamber. The air fuel ratio (AFR) when analyzing the total amount of air in the system is anywhere between 45:1 and 130:1 (Hunecke 1997, 125). This is far greater than necessary for ideal combustion. Therefore, combustion chambers are properly designed to direct the flow of air properly in the primary zone. The schematic of the combustion chamber seen in Figure 14: Basic schematic of an combustion chamber clearly shows the location of air flowing into the combustion chamber.

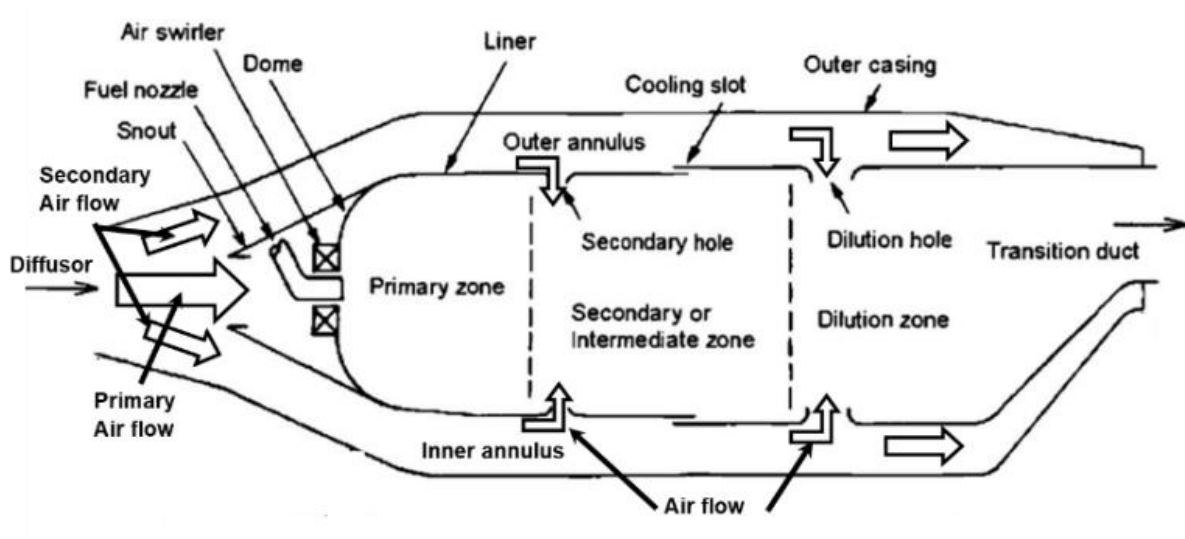


Figure 14: Basic schematic of an combustion chamber (Nemeth 2017).

Approximately 25% of the air in the system enters the primary zone for combustion (Wild 2018, 311). This is done to maintain an optimal AFR. The remaining air is directed around the perforated section known as the flame liner. The holes present in the liner allow air to flow into the secondary and dilution zone to cool the flame temperature and direct the flame towards the transition duct. This excess is also useful for cooling the flame liner. Temperatures inside a combustion chamber can reach 2000 K (Hunecke 1997, 125). This is far beyond the tolerable temperature for most metals used in combustion chamber manufacture. Therefore, air acts as cushion to keep the flame, and subsequent high temperatures, away from

the liner. For this same reason the flame is cooled in the secondary and dilution zone. The initial temperature of combustion is far above that which the turbine blades downstream can tolerate. This ensures tolerable stress on the blades under the high temperatures. Although the holes in the liner act to positively affect the engine, the swirl flow created also contributes to pressure loss in the system which results in a loss of energy.

2.2.3.1 Can Combustion Chambers

Can combustion chambers be the original methods of producing combustion in gas turbine engines and can still be found today in gas turbines used for power generation. Can combustion chambers be cylindrical containers with all of the main components mentioned in the previous section? These containers are arranged circumferentially around the engine turbine shaft and a manifold from the compressor is used to direct the flow into the chambers. These chambers offered advantages in the maintenance of the system. Single cans could be replaced if malfunctions occurred, and the curvature of the cans reduced the warpage effects of the high temperatures. These cans were also interconnected to allow for flame propagation between the cans and also to equalize pressure and temperature across the cans. However, these combustion chambers are typically 25% heavier than more modern annular combustion chambers. They also are ineffective in their use of the space available, decreasing the overall thrust that is produced. Figure 14 shows the flow pattern of a combustion chamber (left) and the physical diagram (right).

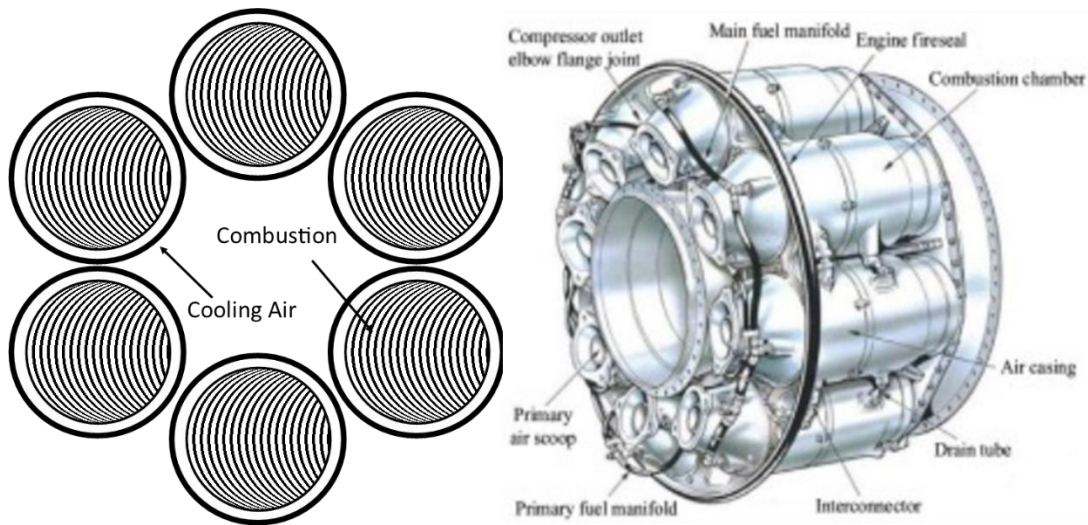


Figure 15: Can style combustion chamber flow pattern (left) and diagram (right) (Notes 2021).

2.2.3.2 Can-Annular Combustion Chambers

Can-annular combustion chambers were created as the transition model between the can and the annular style combustion chambers. Can-annular combustion chambers utilize the air flow style of an annular, while still allowing combustion to occur within the cans. Air flow is allowed to flow around the perforated cans, which is where combustion takes place. This process, as well as a diagram of a physical can-annular combustion chamber, can be seen in

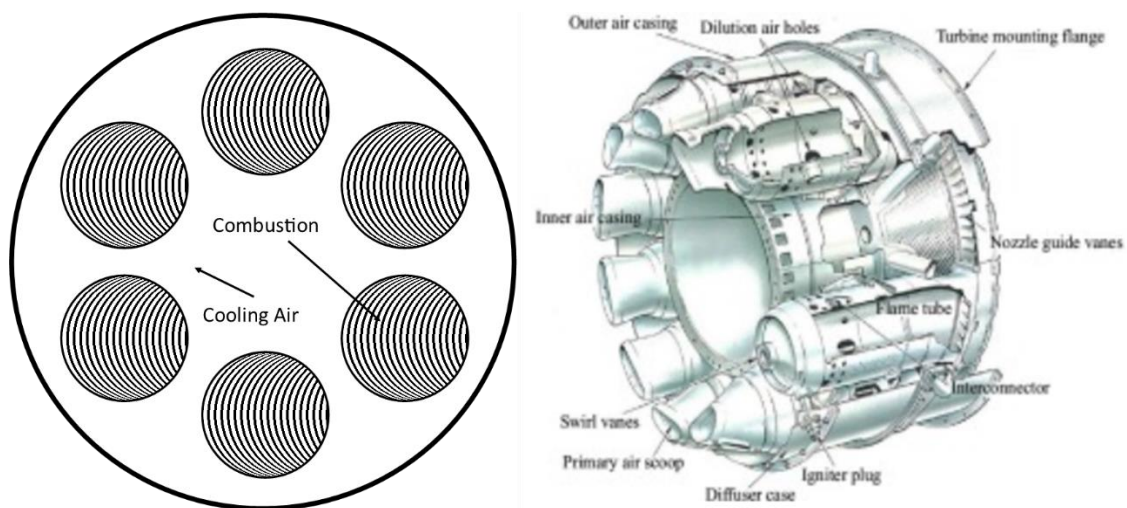


Figure 16: Flow pattern (left) and a diagram (right) of a can-annular combustion chamber(Notes 2021).

These chambers have a major advantage in the ability to maintain high pressure (Wild 2018, 313). This is especially useful for efficient combustion at low power levels, as well as operation under low-pressure, high-altitude circumstances.

2.2.3.3 Annular Combustion Chambers

The final type of combustion chamber and the one used in this experiment is the annular chamber. This is the most modern form of combustion chamber and is used in many high fuel-efficient engines, such as the high bypass turbofan engines. These chambers have the advantage of a much lighter chamber due to the omission of the cans. They also better optimize the space in the engine, allowing for a smaller engine size. Pressure and temperature equalization is no longer an issue without the cans, however the maintenance for the annular chamber is more difficult, requiring the entire chamber be removed for repair or replacements. It also suffers from warpage issues from the high temperatures due to the straight edges. Figure 17 shows the flow pattern of the air and a physical diagram of the annular combustion chamber.

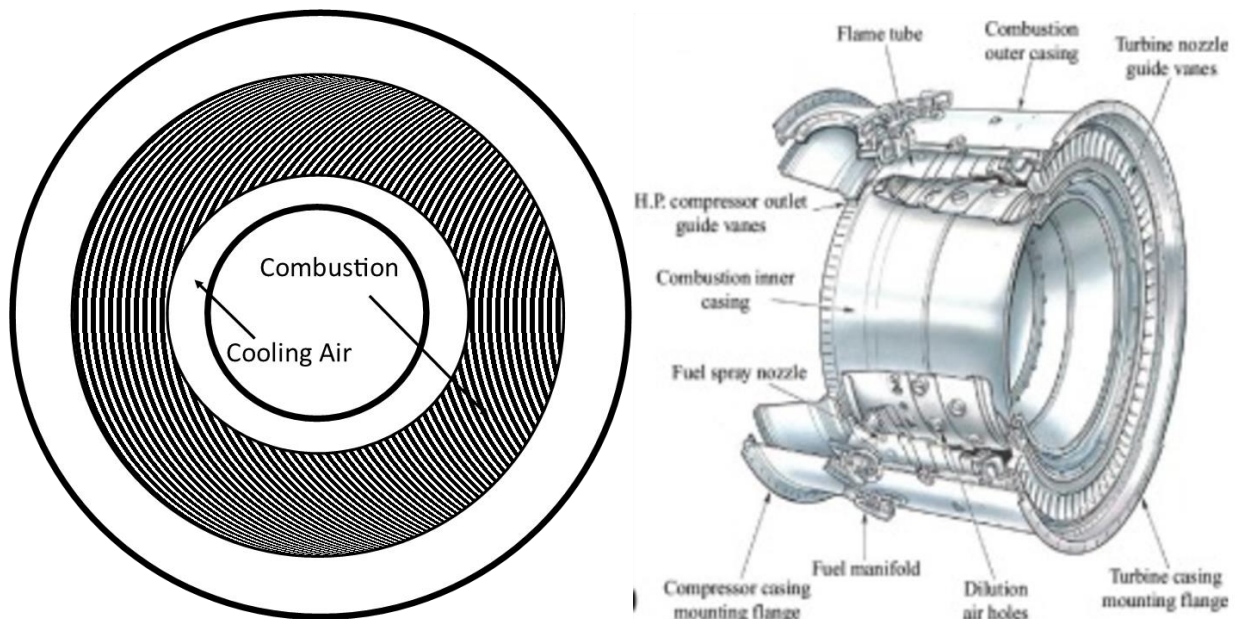


Figure 17: Flow pattern (left) and diagram (right) of an annular combustion chamber (Notes 2021)

2.2.4 Turbines

The turbines that succeed the combustion chamber are very similar to the turbines seen in an axial flow compressor. The purpose of these turbines is to extract most, or ideally all the energy produced from the combustion chamber to rotate a shaft. This shaft may supply power to the compressor, the propeller, or the rotor for helicopters. For civil class transportation aircraft, it may also provide power to an auxiliary power unit to control cabin temperature, pressurization, etc. In turbojet engines, approximately 75% of the power extracted by turbine is used to drive the compressor. For turboprop and turboshaft engine, this number may be as high as 90% (Wild 2018, 313). This is because these engines do not use the thrust produced by the combustion process, and therefore it is most efficient to extract as much energy as possible to deliver it to other components. For many engines, a nozzle diaphragm precedes the turbine. The purpose of this component is to increase the speed of the flow, which also decreases pressure and temperature, and to properly direct the flow. Increasing the velocity also increases the kinetic energy, which will be used to produce work on the blades to create a moment on the shaft. The turbine section contains a series of stators, preceded by rotors. Like the compressor, each set of stator and rotor is called a stage. The number of stages used depends on the number of compressor spools (or the number of shafts needed), the magnitude of rotation required by the compressor (rpm), the amount of energy that is required to be extracted, and finally the maximum allowed diameter of the turbine section of the engine (Hunecke 1997, 137). Another important factor is a derivative of the compressor spools. With higher pressure ratios comes a high amount of energy needed to compress the air. This also impacts the type of turbine used. There are two types of turbines used today. This includes the impact turbine, and the reaction turbine.

2.2.4.1 Impulse Turbines

The impulse turbine was the first turbine type invented. The original water wheel, which used to impact the water of a river or creek to turn the wheel, is an example of this. These turbine types use pressure forces to implement the rotation of the turbine blade. These turbines are often used in turbochargers for automobiles. The stator that precedes the turbine is airfoil shaped. This airfoil shapes of these blades, as well as the angle of attack, create a larger cross-sectional area between adjacent turbines at the leading edge,

and a smaller cross-sectional area at the trailing edge. This narrowing of the flow path increases the velocity and decreases the temperature and pressure. Along with this increase in velocity, the stator also works to direct the flow at an optimized angle and direction as it passes to the rotor. For impulse turbines, energy is transferred by changing the direction of a high velocity flow. This is also referred to as the change in momentum. This energy transfer creates a rotational force in the direction of the convex side of the turbine blade. As the flow moves through the rotor, there will be a decrease in the velocity of the flow due to the energy transfer to the turbine. Because of the flow path, the flow will maintain a constant pressure, however there will be a slight temperature increase due to friction (Hunecke 1997, 139, Wild 2018, 315). Figure 18: Reaction turbine (right) compared to an impulse turbine (left) show an example of a simplified impulse and reaction turbine.

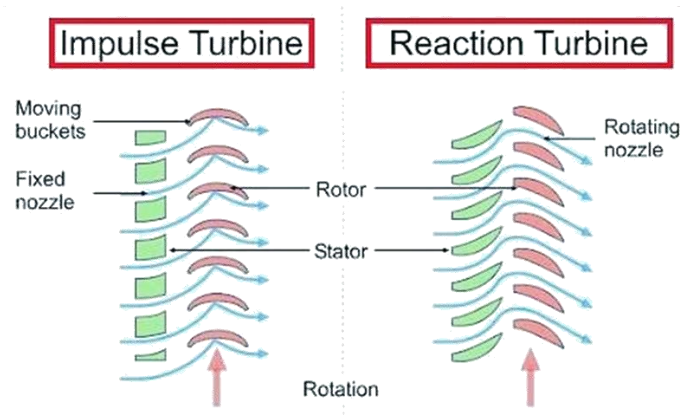


Figure 18: Reaction turbine (right) compared to an impulse turbine (left)(Administrators 2017)

2.2.4.2 Reaction Turbines

A reaction turbine differs from an impulse turbine through the method the turbine rotates. As seen in Figure 18, reaction turbine blades use a stator that is very similar to impulse turbines, however the rotor blades are different. The rotor on a reaction turbine has an airfoil shape that can be used to take advantage of the lift forces. As the hot gas passes through the stator, the flow moves into the rotor. The shape of the airfoil allows for an increase in velocity. Accompanying this is a decrease in pressure. By altering the velocity of the gas, the rotor is able to extract this energy from the gas (Wild 2018, 315). This energy is

extracted and used to rotate that rotor. As previously described, the change in direction of the flow due to the profile of the airfoil allows for a change in momentum, which also increases the amount of energy extracted from the flow. Reaction turbines are most commonly used in aircraft engines due to their high efficiency, which can reach values up to 0.92 (Hunecke 1997, 141).

2.2.5 Exhaust nozzle

The final component of the jet engine is the exhaust nozzle. The purpose of the exhaust nozzle is to extract the remaining potential energy from the hot gas and convert it into kinetic energy in the form of flow velocity (Hunecke 1997, 155). This is accomplished solely through the specifically designed geometry of the exit nozzle. Each nozzle is designed to operate under specific conditions and flight speeds. The exit air velocity from the turbine stage is generally between 750 ft/s and 1200 ft/s (Wild 2018, 317), which will lead to friction loss. The air is therefore diffused to reduce the velocity, while also typically adding rear struts to properly orient the flow to decrease energy loss from the vorticities created by the swirl of the flow. There are two main types of exhaust nozzles: convergent and convergent-divergent (or Laval nozzles).

2.2.5.1 Convergent Nozzles

Convergent nozzles are primarily used for subsonic speeds. This is due to the geometry of the nozzle, which can be seen in Figure 19. Convergent nozzles allow for the velocity of the air to accelerate up to the speed of sound. This limit is due to the mass flow rate of the air as it passes through the exit of the nozzle. As the velocity of the air approaches the speed of sound, more air mass is forced through the nozzle until it reaches a limit to which it cannot force more air mass through. This is described as a “choked” nozzle (Hunecke 1997, 156). In this stage, the pressure at the exit of the nozzle is greater than the pressure in the atmosphere. This causes air to escape in a radial direction out of the exit nozzle, which creates energy loss in the flow. Because of this, converging nozzles are generally used in subsonic applications, such as

military and commercial transport. For supersonic speeds, aircraft will generally use converging-diverging nozzles, as discussed in the next section.

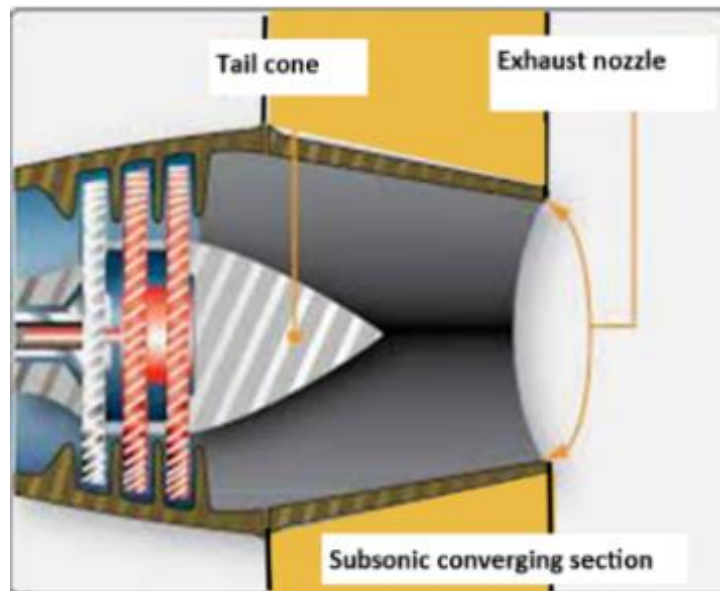


Figure 19: Subsonic converging exhaust nozzle (flight-mechanic 2023).

2.2.5.2 Laval Nozzles

Laval nozzles, also called converging-diverging nozzles, were developed in the 20th century for use in steam engines. Today, these nozzles are used to allow aircraft to travel at supersonic speeds. Laval nozzles, in its most basic form, is a diverging addition to the converging nozzle, and can be seen in Figure 20.

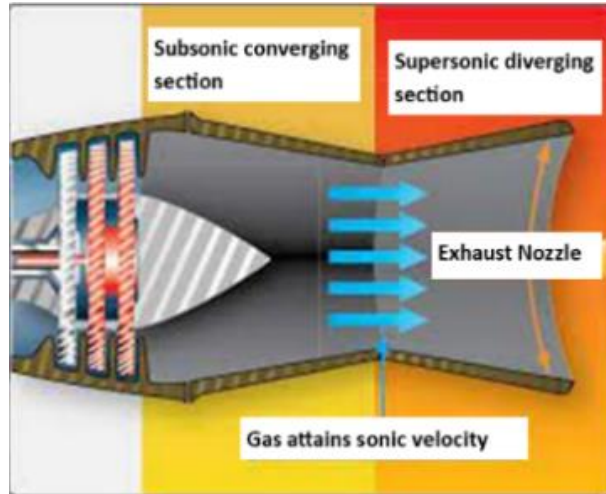


Figure 20: A converging nozzle (left) and a Laval (converging-diverging) nozzle (right) (flight-mechanic 2023)

This diverging section allows the gas at the throat (the smallest cross-sectional area) to experience a decrease in pressure, while still allowing the velocity to increase (Hunecke 1997, 159). This increase in velocity continues due to the pressure and temperature difference between the atmosphere and the hot gas. Practically speaking, Laval nozzles are not useful. This is due to the pressure and temperature engines operate at between at cruising altitude compared to that at ground level (Hunecke 1997, 160). While the air speed in the exit nozzle is below the speed of sound, there is a noticeable loss of thrust. This is compensated for by use of a variable exhaust nozzle. Variable exhaust nozzles may use mechanical or aerodynamic methods to achieve the appropriate exit cross section depending on the atmospheric and engine operation levels.

2.3 Thermodynamic Principles and Efficiencies

2.3.1 Thermodynamic Principles

Gas turbine engines are thermodynamically governed machines. Their operation mainly follows the first law of thermodynamics, which is a version of the law of conservation of energy. This law states that the total energy within a system remains constant. In respect to the thermodynamics of a gas turbine,

this can also be viewed as the difference between the heat energy inserted into the system and the amount of thermodynamic work that is done on the system. This can be seen through the equation below.

$$\Delta U = Q - W \quad \text{Eq. 3}$$

In this format, ΔU is the internal energy of the system, Q is the heat energy added to the system, and W is the work done on the system.

Properly understanding the function behind a gas turbine engine requires fundamental knowledge of several scientific fields of study. This section will briefly cover the necessary fundamental principles involved in the operation of a gas turbine engine.

The thrust produced by the engine is a key component in determining engine efficiency. Thrust is simply the force exerted by the engine opposite and parallel to the velocity of the engine. The production of this thrust is the focus of the next section. Thrust is produced by accelerating air that comes into the engine. This acceleration leads to a greater air exit velocity than the air that entered the inlet. This change in velocity leads to the foundation of thrust production which is a change in momentum flux. The general momentum flux equation can be seen below.

$$p = mV \quad \text{Eq. 4}$$

The change in momentum flux can then be calculated as it applies to the air in the engine. In this analysis, the momentum of the air coming into the engine is examined with the momentum of the air that exits the engine after the combustion cycle has increased the temperature and energy of the air. This can be represented by the equation below.

$$\rho_{in} = m_{air} V_{air}$$

$$p_{exit} = (m_{air} + m_{fuel}) * V_{thrust} \quad \text{Eq. 5}$$

The difference between these two momentum fluxes represents the amount of thrust produced by the engine and can be seen below.

$$F_{thrust} = (m_{air} + m_{fuel})V_{thrust} - m_{air}V_{air} \quad Eq. 6$$

In most cases, the mass flow rate of the fuel can be neglected due to its inconsequential effect on the overall thrust produced. This is therefore the thrust produced by the engine under flight conditions only. Examining the engine thrust produced while stationary (i.e. during initial take off scenario) is a thrust known as gross thrust. The equation itself does not take drag into account. This would result in a decrease in overall thrust produced, also known as the net thrust. The gross thrust and net thrust can be used in the calculation of the efficiency of the engine. This efficiency is composed of two components: thermal efficiency and propulsion efficiency. The propulsion efficiency is the efficiency of the production of thrust of the engine. Therefore, the propulsion efficiency is derived from the power supplied from the engine and the kinetic energy produced. The power supplied to the aircraft can be seen by examining the equation below.

Power to aircraft=flight speed*net thrust

$$P_{aircraft} = V_{aircraft}F_{thrust} \quad Eq. 7$$

By substituting in the thrust, and the kinetic energy, the thrust efficiency can therefore be described by the equation below.

$$\eta_p = \frac{[V_{aircraft}(m_{air} + m_{fuel})]}{1/2[(m_{air} * m_{fuel})V_{thrust}^2 - m_{air}V_{thrust}^2]} \quad Eq. 8$$

Due to the negligible effect the flow of the fuel offers on the production of thrust, this equation can be further simplified to be solely dependent on the velocity, as seen below.

$$\eta_p = 2 * \frac{V_{thrust}}{(V_{thrust} + V_{inlet})} \quad Eq. 9$$

The importance of this equation is in the relationship between efficiency and velocity. As the velocity of the thrust approaches the velocity of the aircraft, the aircraft approaches a better rate of efficiency. In an ideal situation, this thrust velocity would be the velocity of the aircraft, however due to drag forces, there is a decrease in the velocity of the aircraft. For this purpose, the turbines in the compressor stage pull in air to increase the velocity of the air moving into the engine. This is especially important during the takeoff stage when airflow into the engine is zero. It is also important when increasing speed. To increase speed, the engine must pull in a large mass of air that is being forced into the engine due to the velocity of the aircraft.

The other important type of efficiency is the thermal efficiency of the engine. The thermal efficiency is defined as the ratio of the work the engine does overall to the energy input from the ignition of the fuel (Nicholas Cumpsty 2015). The work the engine does to the surrounding air can be represented by the change in kinetic energy of the air as it flows through the system. Furthermore, the energy input from the ignition of the fuel can be described by the lower calorific value (LCV) and the mass flow rate of the fuel in the system. The LCV describes the amount of heat energy that is a result of the combustion of the fuel. The thermal efficiency is described by the equation below.

$$\eta_p = \frac{1}{2} * \frac{m_{air}(V_{thrust}^2 - V_{inlet}^2)}{m_{fuel} * LCV} \quad Eq. 10$$

To determine the overall efficiency of the engine from both the thermal combustion and the propulsion of the engine, a summation of the two efficiencies is performed. Due to both efficiencies utilizing the kinetic energy (or the power supplied by the jet), these values can be cancelled out, resulting in a more simplistic relationship. This can be displayed below.

$$\eta_o = \frac{\text{Useful work}}{\text{Thermal energy from fuel}} = \frac{\text{Thrust} * \text{Speed}}{\dot{m}_{fuel} LCV} \quad Eq. 11$$

Due to the relationship between thrust and mass flow rate of the fuel (i.e., thrust specific fuel consumption) this can be further simplified.

$$\eta_o = \frac{V}{(sfc * LCV)} \quad \text{Eq. 12}$$

The relationship for the overall efficiency of the propulsion of the engine can therefore be seen in this equation. One noteworthy relationship in this equation is the directly proportionate relationship between the velocity of the aircraft and efficiency. This shows that by obtaining the real flight speed, it is possible to determine the efficiency of the propulsion of the engine by using fuel analysis and determining the sfc.

2.3.2 Gas Characteristics and Engine cycle

A gas turbine is an internal combustion engine, similarly to the reciprocating engine found in automobile engines. Heat engine also describes these types of engines. Heat engines operate by increasing the temperature of the air in the system and converting the heat into mechanical work. For automobile and jet engines, this mechanical work is shaft rotation. Therefore, maximizing the heat created within the material constraints leads to more work that can be produced (Wild 2018, 331).

The air is heated by a chemical reaction between a fuel and the air pulled into the system. This chemical reaction is the combustion process. The air in the system, also the atmospheric air, is a mixture itself, comprised of approximately 20% oxygen and 80% nitrogen (Hunecke 1997, 26). There is a negligible percentage of molecules in this mixture that contain inert gases that do not produce any products or react in the combustion process. The combustion process is accomplished due to the oxygen present in the system. Oxygen reacts with fuel (hydrocarbon based) and produces carbon dioxide and water. The result of incomplete combustion (i.e., not enough fuel to react with the oxygen to create carbon dioxide and water) results in the production of carbon monoxide and soot (Hunecke 1997, 131). These pollutants are exacerbated by high temperatures, which are necessary in the combustion process. These high temperatures

produce large amounts of nitrogen (Wild 2018, 26). These are the main products created by the chemical reaction of the combustion process and many studies have been devoted to reducing these products.

This chemical reaction creates the heat that is added to the system. This increase in heat causes the gas to expand, which increases the kinetic energy of the gas. As the gas retreats from the combustion chamber, the turbine impedes the flow of the gas, which increases the pressure. The greater the expansions of the gas, the greater the pressure exerted onto the turbine (Nicholas Cumpsty 2015, 42). This can be seen by examining the formula for pressure,

$$P = \frac{F}{A} \quad \text{Eq. 13}$$

where the force exerted on the turbine can be determined through the thrust force equation below.

$$F_T = mV_{gas} \quad \text{Eq. 14}$$

This pressure is converted into mechanical energy through the rotation of the shaft. The pressure exerted on the turbine is one of the three main variables for air that must be considered when analyzing the operation of a gas turbine (Nicholas Cumpsty 2015, 42). Temperature must also be considered. Temperature can be described as a measure of kinetic energy of a body. This is very important for many aspects of gas turbines. The second law of thermodynamics is utilized with respect to temperature in the cooling of engine components. The last variable to consider is density. Density is a crucial element of the incoming air because the greater density a kilogram of air contains, the more mass of air that will be forced through the engine given the constant cross-sectional area of the inlet. More mass of air means a higher probability of a more complete combustion process, which will produce more thrust. More will be explained on densities effect on thrust and combustion at a later point. These variables and their relationship can be denoted by the ideal gas equation.

$$\frac{P}{\rho} = RT \quad \text{Eq. 15}$$

2.3.3 The Engine Cycle

Internal combustion engines, like the reciprocating and gas turbine, are composed of the same fundamental processes that create power. These processes both use air and chemical reactions to generate power. This process is known as the engine cycle. Figure 21 shows the comparison between a gas turbine and reciprocating engine cycle.

The four components of the engine cycle are the intake, compression, combustion, and expansion. The intake and compression cycles are very comparable between the piston and gas turbine engine; however, the combustion and expansion cycles work in different methods. Combustion in a piston engine occurs once per 720°. However, the combustion for the gas turbine engine cycle occurs constantly while the engine is running. This constant combustion is sustained by conditioning the fuel and air to the appropriate pressure and temperature and mixing the two together. This, along with a constant fuel and air flow, keeps the turbine rotating.

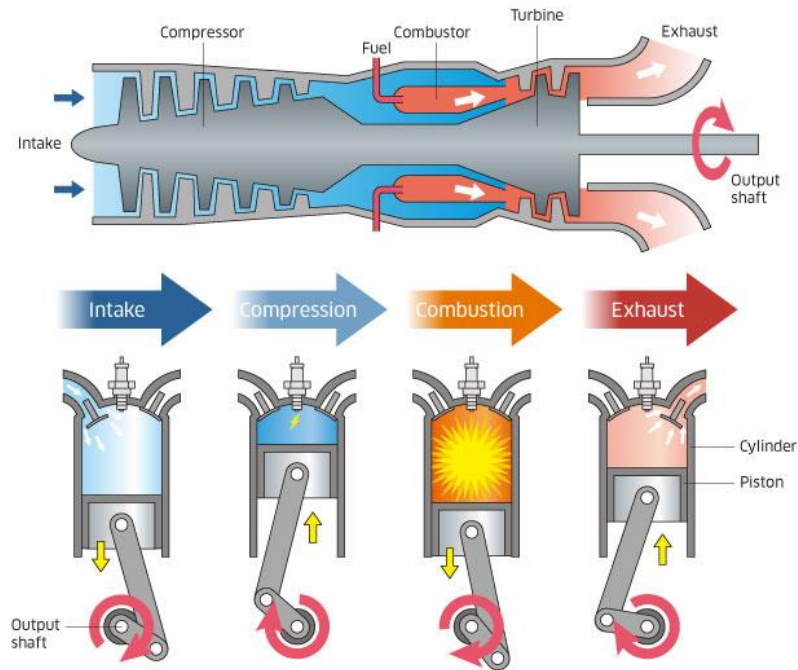


Figure 21: Comparison between reciprocating and gas turbine engine cycle (mechanical-engg 2023).

The work done during the expansion phase is also slightly different as well (Wild 2018, 333). Piston engines use the rapid expansion of the hot gas in the combustion chamber to do work in the form of translation. The piston heads linear motion is connected to the crank shaft, which is rotated. The gas turbine engine uses the expansion of the gas to generate lift forces acting on the turbine located downstream of the combustion. These lift forces rotate the turbine, which powers the compressor and any other auxiliary power systems necessary. The lack of reciprocating components in a gas engine offers the most advantage, allowing more energy to be transferred.

With a fundamental understanding of the combustion and gas characteristics, the engine cycle can be further analyzed by investigating the pressure-specific volume diagram as well as the enthalpy-entropy diagram. These diagrams illustrate the different characteristics of the air flow as it passes through the engine with respect to the air's location in the engine.

Using Figure 22 and Figure 23, it is possible to describe the air at any point inside the engine. The air enters the engine at point A at the atmospheric pressure. As the air approaches point B, the air is

travelling through the compressor, increasing the total pressure and the density of the air flow. This increase in pressure correlates to an increase in pressure energy, which increases the enthalpy of the air. Due to the relationship between temperature and entropy, there will be a constant increase in entropy throughout the entire cycle. Heat is added as the air moves between points B to point C. This introduction of heat (combustion) leads to a decrease in density.

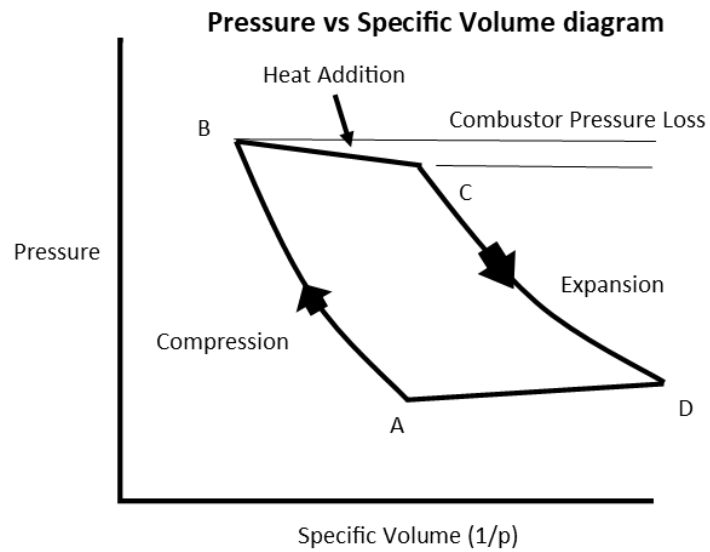


Figure 22: Brayton Cycle

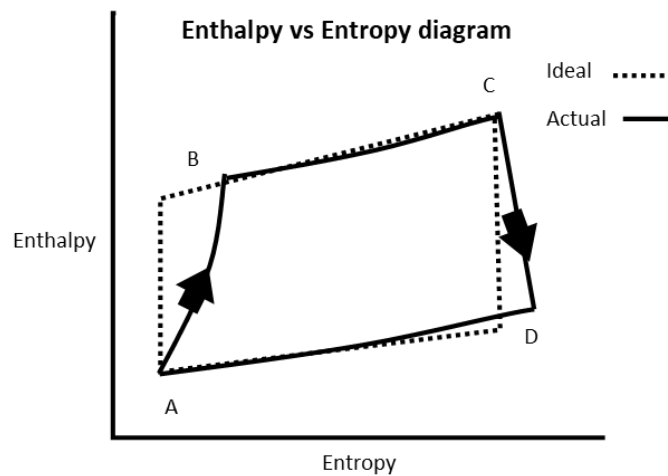


Figure 23: Enthalpy-Entropy

Ideally, there is no pressure loss in this process, however due to friction and natural losses, there is a slight pressure decrease. Combustion in a constant pressure environment, such as that of a gas turbine, allows for a greater mass of air into the system, as well as using much lighter materials and the ability to use low-octane fuels (Hunecke 1997, 28). The addition of heat correlates to an increase in enthalpy and entropy. As the air moves from point C to point D, the gas expands and does work on the turbine, therefore decreasing the enthalpy in the system. The pressure also decreases, with the pressure energy converted into mechanical energy in the shaft, however the hot temperatures allow for a decrease in the density of the air.

Predictability is fundamental in the understanding of a gas turbine. There are several thermodynamic and physics principles that allow for accurate assumptions which aid in the research of gas turbine engines. One such principle is the conservation of matter. This principle states that the matter entering the system does not randomly exit the system. In other words, matter is not created or destroyed. This understanding allows researchers to better predict the combustion efficiencies and thrust. This principle is mathematically represented by the following equation.

$$m_1 = m_2 \quad \text{Eq. 16}$$

$$\rho_1 V_1 A_1 = \rho_2 V_2 A_2$$

This understanding can be specifically utilized in the combustion process. The more air mass that can be pulled into the compressor will allow for a greater thrust. This is a result of the conservation of matter. The combustion process creates a reaction between the fuel and the oxygen in the air. This same amount of air mass must be present as the gas expands and exits the system. This constant mass property allows for the thrust produced.

Another important principle is the conservation of energy. This is based on the first law of thermodynamics which states energy is indestructible. Therefore, energy must be transferred throughout the system. This transfer of energy can be taken advantage of to optimize the transfer, allowing the greatest practical energy exertion to generate thrust.

The energy of the gas is represented by three variables: the internal energy, pressure energy, and kinetic energy. The internal energy is a function of the temperature of the gas as it enters the system. Pressure energy is a function of the pressure state of the gas as it enters the system, and the density of the gas. Finally, kinetic energy is a function of the velocity of the flow. These can be represented mathematically below.

$$\begin{aligned}
 U &= c_{v1}t_{v1} \\
 P &= \frac{p_1}{\rho_1} \\
 K &= \frac{1}{2}v^2
 \end{aligned}
 \tag{Eq. 17}$$

The purpose of the combustion process is to input heat into the system, therefore increasing the energy of the gas between when it enters the system and exits the system. The introduction of energy into a system is therefore equivalent to the energy that exits the system (or in other words is used to produce work). This can be represented as the first law of thermodynamics in the equation below.

$$c_{v1}t_{v1} + \frac{p_1}{\rho_1} + \frac{1}{2}v_1^2 + \frac{Q}{m} - W = c_{v2}t_{v2} + \frac{p_2}{\rho_2} + \frac{1}{2}v_2^2
 \tag{Eq. 18}$$

This vital concept introduces the importance of understanding the different static pressure and temperature throughout the flow specifically before and after the combustion. This understanding of the present state of the air at these locations experimentally can lead to a better understanding of the energy transfer in the system. It also gives important information on the emissions of the combustion process. The products released, specifically NO_x, is a more prevalent product with higher combustion temperatures. Therefore, understanding the temperatures experienced in the combustion chamber can allow for better prediction of the NO_x emissions and prove instrumental in creating methods of NO_x reduction.

2.4 Fuel Characteristic and Systems

The fuel used in the combustion of a gas turbine engine is an immensely important factor in the propulsion and emissions of the engine, not to mention the proper operation through lubrication and necessary viscous properties. Therefore, fuel properties and characteristics must be properly matches to the engine purpose and function. Ambient temperature, distance of operation, altitude of the flight, and many other factors contribute to the fuel used. Not only is the fuel important in the proper operation of the turbine, but the fuel control system must also be working effectively to appropriately regulate the fuel input into the combustion chamber. The next section discusses the important characteristics involved in the selection of the fuel as well as the systems that control fuel flow.

2.4.1 Ideal Fuel Properties and Characteristics

Gas turbines operate under different circumstances than reciprocating internal combustion engines. While the operation parameters for automobile and marine engines allow for the use a gasoline, gas turbine must typically consider a drastic change in operation temperature and pressure, as well as an increase in risk and therefore increase factor of safety, which affects optimal choice of the fuel. Because of the differences in operation conditions, gasoline is not typically used in powering gas turbine engines.

There are many factors when considering the fuel type to use for a gas turbine (Wild 2018, 343). The fuel must be appropriately viscous at all operation parameters. This includes the changes in temperature and pressure that accompany a higher altitude. It must also allow for the engine to start under conditions at the ground. Proper combustion is also a factor in the fuel type used. This includes efficient combustion at high altitudes as well as ground level, and all heights in between. Different factors like humidity, pressure, and temperatures affect the combustion differently and will change throughout the flight. Therefore, the fuel must have properties that allow for efficient combustion at each instance, and if this is not attainable, an augmentation must be made to the system to sustain proper thrust. A highly sought-after factor in fuel quality is the calorific value. High calorific values per unit of fuel allow for more energy to be converted to heat and creates more favorable results in several different areas (weight of the fuel, emissions, fuel rate,

etc.). It is also important that the fuel is not corrosive or damaging to the engine. Depending on the materials used in the engine, different fuels can have negative effects on the different components. For example, some fuel tanks are designed for specific fuel types and are made from elastic materials. The introduction of synthetic fuels that have aromatics (compounds that create harmful emissions) removed can shrink the fuel tanks, creating cracks and leaks in the tank (Hunecke 1997, 194). Finally, it is important to consider the safety of the fuel. Some fuels are more volatile than others. This difference in volatility changes how the technicians refuel the plane. Fuels like Jet A are less volatile, while aviation gasoline must take increased precautions to reduce electric static, high velocity refuels, and turbulent refueling to avoid fire and explosion. These factors should be considered when choosing a fuel type for engine combustion.

2.4.2 Fuel Composition

Knowing the factors that qualify fuels for use in gas turbines is equally as important as knowing the properties that compose fuels and allow for energy extraction as well as the determinates of emissions. As previously discussed, the calorific value is the heat created from the chemical reaction of combustion of a certain fuel. This value is determined by the hydrocarbons present in the fuel. Heavier hydrocarbons (i.e., a denser fuel) lead to a larger calorific value. Sulfur is also a factor to consider. Sulfur is responsible for the corrosive nature of fuels, and therefore, more sulfur present in a fuel will lead to a more corrosive fuel, which will need to be accommodated for in the fuel system. Another very important property of the fuel is the freezing point. High altitude flight (30,000 to 36,000 ft in commercial airlines) imposes a decrease in temperature on the engine. This can lead to freezing temperatures (approximately -55°C) that have the potential to freeze the fuel. This is an issue because when fuel begins to freeze, ice crystals begin to form. This formation of ice crystals creates waxy particles that clog fuel filters. Many factors affect fuel temperature (ground level atmospheric temperature, aircraft speed, quantity of fuel etc.) and must be considered in fuel choice. Another property that must be considered is the volatility of the fuel. Certain fuels are not harmful in liquid state, but the vapors that settle above the fuel in the fuel tank have high level volatility, and therefore present a higher risk of fire and explosion. These fuels should be handled with more

caution. A final property of fuel that is considered for gas turbine is the emissions. In recent years, more focus has been placed on reducing harmful emissions created by the combustion process. Because of this, emissions are a very important factor to consider in fuel choice.

2.4.3 Fuel Types and Additives

There are many different types of fuels used in gas turbine engines. Kerosene, also known as Jet A, is one of the most common inside the US, while wide-cut gasoline, also known as Jet B, is much more common in military applications and outside the US. Kerosene is the most commonly used in commercial aircraft industry because of the high calorific value, low freezing point (between -40°C and -50°C), and low vapor pressures. Wide-cut gasoline is a mix of gas and kerosene. This makes the resulting fuel less dense and more volatile (vapor pressure around 2-3 psi) than kerosene. However, wide-cut fuel has an advantage in the freezing temperature (approximately -60°C). The calorific value, however, is either higher or lower, depending on how it is measured. When measured by unit volume, the calorific value for kerosene is higher than wide-cut fuel, however when measure per unit mass, the wide-cut has a higher value.

Other fuel types are currently being investigated as well to reduce emissions. These fuels are synthetic and bio-derived fuels. Synthetic fuels use the Fisher-Tropsch process to remove aromatics and other harmful material from the fuel. The remaining fuel is cleaner burning but causes issues in the reduced density and causes problems with some fuel system components. Bio-derived fuel is generally made up of a natural material combined with ethanoyl. This natural material can be from animals, like fat, or from vegetables, like vegetable, corn, rice, or sunflower oil (Badami et al. 2014). Most frequently, bio-derived fuel is mixed with kerosene or wide-cut fuel to combine the clean burning of the bio-derived fuel and the high calorific and density of kerosene fuels.

Additives present in fuel, either purposefully or unavoidably placed, have significant effect on the performance and resultants of the fuel. Water will naturally occur in fuel despite the efforts of engineers to

only inject pure fuel. The amount of water present in the fuel is affected by the atmospheric temperature. The saturation level (amount of water prevalent in the fuel) is measured in parts per million (ppm) and is approximately equivalent to the temperature in Fahrenheit. Therefore, 50°F atmospheric temperatures correlated to approximately 50ppm of dissolved water in the fuel. At cool temperatures, water tends to settle at the bottom of the fuel tank due to the heavier nature of water. However, at freezing temperatures, the water will combine with the fuel, creating a gel or icing. This causes issues with the fuel filters in the fuel system. It also allows for the introduction of small amounts of increases in water. When warm temperature outside air enters the fuel tank, condensation takes place, which can increase the saturation level of the fuel. There are manufactured additives that can be combined with the fuel or the fuel tank to relieve these issues. These additives, like Prist, combine with water at lower temperature and further lower the freezing temperature of the water. This delays the icing effects of the fuel and water. The presence of water also introduces the growth of microorganisms in the fuel tank. This can typically be confirmed by noting an abnormal smell or a brownish/reddish discoloration of the fuel. These microorganisms can form chemical compounds that reduce the structural integrity of the fuel tank, causing cracks and leaks. This can be remedied by coating the fuel tank with a corrosive resistant mixture. These mixture limit or sometime even eliminate the presence and effect of microorganisms on the fuel tank.

CHAPTER 3

LITERATURE REVIEW

3.1 Experimental and numerical experimentation of Turbojet Engines

The usefulness and importance of smaller turbojet engines cannot be underrepresented. Jet engines in general are very expensive to design and manufacture, not to mention the maintenance that must be done and replacing any malfunctioning parts. Because of this, the cost to operate and test can be very high. The cost is not only represented in economic terms, but also environmental. Operation of jet engines, especially larger ones, comes with harmful emissions created from this process. Smaller jet engines, however, produce less emissions, and have a much smaller operation and manufacturing cost than large engines. This accompanied by the increasing accuracy of CFD analysis, provides an excellent opportunity to use smaller jet engines as a proxy for larger engines, while allowing for comparable results to that of a larger engine.

One study conducted by Badami et al (Badami, Nuccio, and Signoreto 2013) compares the experimental results from a SR-30 turbojet engine to the numerical results created using CFD. The experimental component records the pressure and temperature at various critical components on the engine, while also measuring the thrust produced, air flow rate, fuel flow rate, and an emission measurement to collect the output of carbon monoxide, nitrogen oxide, oxygen, and the unburned hydrocarbons. The purpose of this study was to compare and gain knowledge on the accuracy of numerical and experimental data from a mini turbojet engine. This study found that the operative fluid pressures and temperatures were comparable to that of a regular sized turbojet engine in idle, supporting the validity of the accuracy of the miniature compared to the regular sized engine. For the compressor, this study found that the CFD analysis was accurately comparable. With respect to the temperature through the system, this study found that the outlet temperature of the compressor showed cooler temperatures due to the warming effects the compressor exerts on the compressed air. It also found that an oscillation of temperature at the turbine outlet as the engine increases speed, which is not present in the numerical analysis. This can be explained due to

incomplete and inefficient combustion (especially at low speeds) and varying temperature hotspots created due to the spray of the fuel injector. This spray results in an anisotropic fuel to air mixing, which generates higher temperatures in some areas, and cooler areas in others at the combustion. A similar inconsistency in the temperature between the numerical and experimental was also seen at the turbine inlet. The data showed a temperature difference between the two experiments anywhere from 60-180°C. This can also be explained by similar principles as stated above.

Again, when examining the theoretical and experimental results of gas turbine engines, the research conducted by Sajesh et. al (Sajesh 2014) is another useful source. This study consisted of using a Minilab SR-30 test rig including a diffuser, axial flow compressor, reversible annular flow combustion chamber, and an axial flow turbine to gather experimental data. It also calculated theoretical values. The purpose of this experiment was to use the accuracy of the data gathered when compared to the theoretical data to determine the accuracy and better understand the Braton thermodynamic cycle. This experiments a difference of 18.35% between the data for the compressor, 16% for the turbine, and a difference of 56N between the thrust.

Another study conducted by Dubovas and Brucas (Dubovas and Bručas 2021) was done to compare the numerical and experimental results between a combustion chamber for a small turbojet engine. This experiment used propane gas for the fuel, and in computational methods used three different methods to model the combustion process: WD1, WD2, and WGS (Westbrooke Dryer combustion reactions). It also used 4 different meshing methods with increasingly more elements and nodes and used four different fuel-air ratios. This study found that with greater fuel-air ratios, there was more variance in the accuracy of the resulting exhaust temperature between the computational and experimental results. The most accurate results occur in fuel-air ratios between 1:30 and 1:150. It also found that richer mixtures led to computational deviance from the experimental in the form of a surplus, while lean mixtures resulted in lower temperatures as compared to the experimental.

More research conducted by Gonzalez, Wong, and Armfield (Gonzalez, Wong, and Armfield 2007) was done to investigate the convergence of numerical CFD and experimental results. This investigation first used 6 different computational methods (3 types of RANS, 3 types of LES) to determine which had a convergence of temperature and velocity (experimentally measured at the outlet). These models simulated a 60° section of the combustion chamber, using tetrahedral elements for the inner section of the chamber, and hexahedral elements for the vaporizer and outer section. These simulations elements ranged between 130,000 and 500,000 elements. The fuel used was a model of kerosene which had 80% n-decane and 20% toluene. The boundary conditions used were as follows: air flow of 0.22 kg/s, inlet pressure of 2.2 bar, global air fuel ratio of 65, air inlet temperature of 400K, and inlet temperature of fuel being 300K. This investigation found that the LES-WALE (wall adapted local eddy) model provided the most accurate results when compared to the experimental. When further examining the LES-WALE model, it showed stoichiometric mixing occurred at the same area of the high temperature. It also found high temperatures located before the outlet, and lower temperatures at the outlet. This was determined to be caused by the location of the holes of the diffuser. It is likely that an increase in air, creating a leaner mixture, will reduce the high temperatures seen in the results.

Another study conducted by Wessley and Chauhan (John Wessley and Chauhan 2019) used a modeling simulation software called Flownex to model a small turbojet engine capable of producing 4 kN of thrust. This software uses component matching to input the parameters for each component. The components were chosen from a library of components that are preloaded into the software. These main components of the engine were the inlet, compressor and impellor, combustion chamber, turbine, exit nozzle, pipes, and heating elements, and the analysis was performed in a one-dimensional space. This study found a direct relationship between the ambient pressure and the max temperature, mass source, exit Mach, thrust, and the power generated from the turbine. It was concluded that the maximum temperature, velocity in the compressor, and exit velocity was 561.29K, 23.363 m/s, and 433.157 m/s respectively, all of which

were inside the design constraints. Finally, it was concluded that at an ambient pressure of 1.01 bar and 8.71 kg/s inlet air flow, the thrust produced was 3.79 kN, which was just under the engine's thrust capability.

3.2 Experimentation of Alternative Fuels and Effects on Gas Turbine Emissions

While the function and design of the turbojet engine is important, equally so are the emissions produced from the combustion process. With a large percentage of research focusing on climate change, the reduction of greenhouse gases is of the utmost importance. This has led to many studies being conducted to investigate the gases produced during emission and the best methods for reducing them. This has led to advancements in biofuels and synthetic fuel, which act to reduce emission due to their chemical composition, as well as the introduction of augmentations to the combustion process.

Ossello, Balepin, and Snyder (Vladimir Balepin 2002) conducted a study which examined the reduction of NO_x emissions through water injection technology (WIT). This study used a Boeing 777-200 aircraft equipped with 2 Pratt and Whitney 4084 turbofan engines with a low pressure compressor (LPC) and high pressure compressor (HPC) and implemented the water injection into 5 different locations in the engine; the inlets of the HPC, the inlet of the LPC, the combustion chamber, the inlet of the LPC with a reduced air bleed, and finally the inlet of the HPC with a reduced air bleed. This study found that the WIT located at the LPC with reduced air bleed led to the most reduction in NO_x (up to 60%) with the less amount of water present in the air flow. It also found that through WIT, there could be a reduction in the HPC temperature up to 300K. It also found that by implementing the WIT during takeoff, the turbine temperature could be maintained at a constant temperature of 1482 K. The implementation of WIT could also have other benefits including the durability of the engine (due to a decrease in stress from high temperatures) and better efficiency of the engines (due to the ability to better optimize turbine clearance because of lower length of expansion of blades).

In a study conducted by Gawron and Bialecki (Gawron and Bialecki 2017), the authors presented an experiment to compare the performance and resulting emissions between two fuel types: Jet A-1 and a Jet-A-1/HEFA fuel blend. This study was conducted using a miniature turbojet (part of a test rig). The authors setup included testing several variables, including temperature, thrust, fuel efficiency, thrust-specific fuel consumption (TSFC) and emissions as it relates to carbon monoxide, carbon dioxide, and nitrogen oxide. These variables were studied, and data collected at RPM values of 39,000, 70,000, 88,000, 112,000. This study found Jet A-1 produced higher or marginally higher data in all experiments, with the largest difference being 10%. It is noted that the fuel consumption rate and TSFC were lower for the HEFA blend. This lower value can be explained by the higher heat of combustion and the lower density of the blend. It was seen that the most dramatic difference in values was seen at low RPM values. Another noteworthy conclusion was the lower emissions recorded by the HEFA blend.

Another study conducted by Gawron et al (Gawron, Bialecki, and Kazmierczak 2016) was performed to study the effects of using a Jet A-1/Butanol blend on performance and emissions. The fuel blend was comprised of 90% Jet A-1 fuel and 10% butanol. This experiment compared this fuel blends effect on exhaust gas temperature, thrust, specific fuel consumption, fuel consumption, and the carbon dioxide, carbon monoxide, and nitrogen oxide emissions with that of the Jet A-1 fuel. These tests were conducted at varying motor RPM's, including 39,000, 70,000, 88,000, and 112,000. This study found that the two fuel types were accurately comparable for the thrust produce and the exhaust temperature. The Jet A-1/Butanol blend results showed a slightly higher fuel consumption and specific fuel consumption rate, which can be explained by the lower fuel calorific value. This fuel blend also showed lower emissions for carbon dioxide, carbon monoxide, and nitrogen oxide.

Once more, in analyzing fuel blends and the emissions and performance, another study was conducted by Solmaz et. al (Hamit Solmaza 2014). This study focused on examining the effects of using multiple fuel blends of jet A1 and diesel on the emissions and performance of the engine. This study used blends containing 100%, 95%, 90%, 75%, and 50% diesel. This study found that a straight diesel produced

the most torque per engine speed, with the 50% blend following behind. It attributed this loss of power for the Jet-A1 blends to the lower heating value, calorific value, density of the Jet-A1 fuel. This greatly reduced the power output seen. It also concluded the same factors negatively affected the fuel consumption of the Jet-A1 blends, finding diesel to produced lower fuel consumption values. When examining the emissions, this study found that lower heating values and higher latent heat of evaporation values led to a lower value of produced NO_x for the Jet-A1 blend. In studying the smoke and CO₂ contents, the study concluded Jet-A1 blends had undesirably higher values of these variables than pure diesel. This was attributed to the higher carbon content present in Jet-A1 fuels.

Another study conducted by Altarazi, et. all (Altarazi et al. 2021) was conducted to determine the effect of using dual diesel biofuels compared to single diesel biofuel, and compared these values to a baseline of Jet-A1. The fuel blends in this experiment were B90, B70, B50, B30 and B10. The blends were constructed of *Thespesia populnea* oil methyl ester (THOME) and Palm oil methyl ester (POME). This experiment tested the performance in terms of specific fuel consumption vs brake power (BP) of the engine. It also tested the emissions of CO, CO₂, and NO_x of each fuel blend. This experiment found that the B10 (5% THOME, 5% POME, and 90% Jet-A1) dual diesel biofuel had lower specific fuel consumption per the brake power of the engine, even lower than Jet-A1. This was determined to be a consequence of the low calorific value of the other blends. With respect to the emissions, the CO emissions seemed to decrease with an increase in BP, while the CO₂ emissions increased with BP. This could be understood to occur due to a richer air/fuel ratio being required for higher BP. It was also found that the B10 diesel fuel blend created less emission than the baseline Jet-A1 for both the CO and CO₂. These lower emissions could be concluded to occur because the biodiesels contained oxygen, which leads to easier combustion at high temperatures. Finally, the NO_x was seen to increase with the BP. While Jet-A1 fuel had lower emissions than the B10 blend, it was found that these values were very similar.

Another study conducted by Benini, Pandolfo, and Zoppellari (Benini, Pandolfo, and Zoppellari 2009) studies the NO_x and CO₂ emission by inserting steam and water into the combustion chamber. This

was done by using both experimental and computation methods. Steam and water were inserted downstream of the combustion just before it escaped into the turbine section. The computational results were obtained by using a 30° section (due to the symmetry). The results found that, for steam, there is an overall reduction in both CO₂ and NO_x, the most at 100% and 200% respectively. This was most likely due to the increase turbulence, and the decrease in the temperature of the fluid. When inserting water into the system, the results found that there was no reduction for CO₂, but there was a reduction for NO_x at 100% water. This was most likely due to the reduction in the temperature. This study found that the numerical and experimental results aligned well.

Other studies have been conducted as well, like those done by Gurbuz et al (Gürbüz et al. 2021). This study was conducted to determine the effects of using a euro diesel/hydrogen blend compared with the lean euro diesel fuel. The turbine used in this study is a small turbojet engine, and the experiment tests the fuel's effect of performance and emission levels. This study found that there was a dramatic decrease in fuel consumption and specific energy consumption with an increase in rpm. It also found that there was an increase in engine efficiency up to 15% at all speeds. Finally, with the environmental variables, there was a slight decrease in CO and CO₂, and an increase in HC and NO_x emissions.

Another study conducted by Badami, Nuccio, et. al (Badami et al. 2014) was conducted which used three different types of fuels and attempted to validate computation results with experimental results of a mini turbo jet engine. This research used an SR-30 turbojet engine with Jet-A (as the control), a synthetic Gas to Liquid blend, and a bio-diesel fuel blend comprised of 30% Jatropha Methyl Ester (JME) and 70% Jet-A. With respect to the CFD computations, this study used 1.4 million cells across 1/6th of the actual combustor (due to the 6 fuel injectors). This simulation used a two-step Eddy Dissipation model to model the combustion and used a Reynolds Stress Model. The NO_x was predicted using a Probability Density Function (PDF) and a Eulerian-Lagrangian model was used to simulate the spray evolutions. Experimentally, this study showed that the GTL synthetic and Jet-A had similar results in terms of CO emissions, thrust produced and fuel flow rate. It also found that the GTL synthetic and JME blend showed

similar trends in respect to NO_x and CO emissions, and the JME blend showed a more favorable UHC emissions. This study also found correlating results between the simulation and the experimental results for the NO_x at high operating speeds only. This was not the case for lower operational speeds. This was determined to be due to larger than expected SMD of the fuel droplets. This caused flame envelopes, which produced higher levels of NO_x that the CFD simulation was not set capable of predicting. Therefore, the CFD simulation predicted less NO_x than was actually present. It also found that the CFD simulation predicts nearly two magnitudes less CO emissions than were experimentally gathered.

Chiariello, Allouis, Reale, and Massoli (Chiariello et al. 2014) investigated the results of using 4 different bio-fuel blends on the emissions output, specifically analyzing the CO, NO_x, and particulate matter (PM) with respect to the load of the engine. These loads were full load (25kW) and partial load (15kW). This experiment used a Capstone micro gas turbine (C30) and a portable flue gas analyzer (TESTO 350 S) to measure the O₂, NO, NO₂, CO, SO₂, and CO₂, and also measured the exhaust temperature and pressure. The different blends used in the experiment were sunflower oil, rapeseed oil, and Jet A1 was used as the constant. Each oil was mixed with Jet A1, comprising both 10% and 20% of the total volume, resulting in 4 different biofuels for the experimentation. This investigation found that the rapeseed and sunflower blend offers no substantial difference in emissions of NO_x and CO with respect to Jet A1 fuel. However, there were very high increases in the partial size of the PM for the sunflower and rapeseed blends. The approximate size of the Jet A1 fuel was 20 $\mu\text{g}/\text{m}^3$, while the rapeseed and sunflower fuel blends resulted in PM size of approximately 60 $\mu\text{g}/\text{m}^3$ and 1000 $\mu\text{g}/\text{m}^3$, with the partial load creating slightly higher PM values. The sunflower blend also produced larger particle sizes than the rapeseed. In comparing the 10% and 20% of each oil blend, it was found that there were no significant changes between each blend for either sunflower or rapeseed. This study concluded that the explanation for the oils high PM is due to a greater soot induction time when compared to Jet A1. This delayed reaction leads to slower soot oxidation, which leads to the higher PM results.

Hoxie and Anderson (Hoxie and Anderson 2017) conducted an experiment which tests fuel blends using soybean oil (SBO) and #2 ultra-low sulfur diesel. This experimented using blend comprised of 25%, 50%, and 75% SBO mixed on a per volume basis with ULSD and compared the results to pure ULSD. This experiment was conducted using a SR-30 turbojet engine at 78,000 RPM and used a thermocouple and pitot probe to measure temperature, kinetic energy, thrust, and enthalpy flux. These measured values were used to calculate the engine efficiency due to the poor nozzle design and disruptive thermal efficiency of the SR-30, and therefore, the efficiency represents the combustion efficiency. This study concluded that the SBO blends showed a greater variation in exhaust temperature than ULSD. This could have been caused by the exhaust nozzle design, which included several struts for structural support. It also found that efficiency was slightly higher than the ULSD, however, the higher values were insignificant due to the error margin. Finally, the 25% SBO blend was compared to the USLD at different RPM's. This found that increases in the RPM showed increase in efficiency, exhaust gas temperature (EGT), and thrust, with the SBO blend having a slightly higher EGT than ULSD.

Qui et.all (Lei Qui 2018) also conducted research in a similar field examining the effects on fuel flow rate on a small micro turbojet engine. This study used Fluent software to investigate the best location to place an ignitor based on high temperature and mass fraction of the fuel in the system and based on the lower areas of velocity of the air. This study also applied changes to the combustion chamber, rounding off the back wall and centering and adding a conical exit nozzle for the vaporizers. Using this information, the experiment was conducted with the new location of the ignitor. This study tested 5 fuel flow rates of diesel and measured the rotational speed of the electric motor used to start the engine and compared it to the time taken to reach idling turbine speed. This found that 7000 rpm was the most ideal speed for the electric motor, providing the quickest startup time. It also used this ideal electric motor speed and 5 different fuel flow rates to determine the turbine power output. It found that the larger fuel flow rates lead to a higher power output.

3.3 Noise and Vibration Analysis for High Aromatic Fuels

Finally, noise and vibration analysis are critical to the research and development of engines. This can be addressed via the harmonics found based on geometrical foundations of the engine, however the fuel used in the engine also plays a significant role in the vibrations experienced. High volatility fuels, like Jet-A, can lead to higher vibrations in certain parts of the engines. Most fuels, including Jet-A, F24, JP-8, and so on include a fairly higher aromatic content. This aromatic content is important for sealing purposes. However, fuels with high aromatic content are also generally higher in emissions. The following section investigates the effect of these aromatics in the fuels and how it relates to the noise and vibration development of the engines.

The work conducted by Bhupendra (Khandelwal et al. 2014) investigated the emission and vibration characteristics of a small-scale gas turbine engine when using 4 different types of fuel. These fuels include Jet-A from 2 different sources, CTL synthetic jet fuel, and GTL synthetic jet fuel. The results found that the GTL fuel produced better operational stability in each range of the engines load as compared to the other fuels.

Furthermore, Sharma (Sharma et al. 2020) conducted similar work on the aromatics contents in various diesel blends to determine their effect on the spray behavior and engine performance. The results found that with blends of 5%, 10%, and 15% aromatics added diesel fuel, there was no significant change in the spray behavior of the fuel. Furthermore, an improvement in the fuels was found when using Ethylbenzene and toluene. This was found to be due to the favorable calorific value, atomization, cetane number, and structure. Moreover, the lower aromatic content of certain diesels like ULSD leads to high noise pollution as compared to those with higher percentages of aromatics.

Furthermore, Almohammadi conducted similar research on the effect of four different aromatics blended with low (Almohammadi et al. 2021) aromatic fuel to determine engine performance. The results found that the reduction in calorific value and cetane number due to the introduction of aromatics reduced engine performance. The results found that introducing the higher density methylnaphthalene aromatic

resulted in higher levels of emissions. This was due to the higher boiling point and lower H/C ratio. Indane mixed at 5% found more promising results, with a higher brake thermal efficiency and lower BSFC.

The study done by Zheng (Zheng et al. 2021) was done to test 16 different aromatic blended fuels to determine the effect of molecular structure, density, and H/C ratio on the emissions and performance. The results found that indene and naphthalene additions greatly increase emissions. It also found high density and high H/C ratios properties for the aromatics have a direct correlation to high levels of soot and emissions. Moreover, the molecular structure of di-aromatics and cyclo-aromatics produce higher levels of soot and emissions, while the alkyl-benzene molecular structure showcased improved emissions.

Wijesinghe (Wijesinghe and Khandelwal 2021) investigated the impact of alternative fuels and aromatic species on the spray behavior and atomization properties of the fuels. The results found that as the aromatic species of ethylbenzene, cumene, and tert-butylbenzene correlated to an improvement in atomization, leading to the conclusion that the greater the size of these types of aliphatic groups attached to the benzene ring results in an improvement in the droplet size and subsequent combustion properties. These groups also have lower densities, which corresponds to the improved spray characteristics.

An investigation conducted by Matthaïou (Matthaïou, Khandelwal, and Antoniadou 2017, Matthaïou and Antoniadou 2016) was done to investigate the vibrational instabilities seen in a combustion chamber when using different fuels. These investigations also used different fuel blends and air-fuel ratios to determine their effect of combustion stability when using and training a one-class support vector machine (OCSVM) method. The algorithm found there was very little difference between the fuel blends and air-fuel ratios with respect to the vibration.

Other studies conducted by Wijesinghe (Wijesinghe, Ling, and Khandelwal 2019) have been done to investigate the effect of using JEFA type alternative fuels. In this experiment, an auxiliary power unit was used to compare the vibrations between the low aromatic HEFA alternative fuel and traditional commercial Jet-A. This investigation found that the difference in a low aromatic HEFA fuel and traditional

Jet-A resulted in significant differences in vibration results. These results showed the pure low aromatic fuel had higher vibrational amplitudes.

Presently, the literature presented leads to the conclusion that many aromatics provide a degree of combustion stability to many kerosene-based fuels. This can be derived strictly from the vibration data, as well as the atomization enhancements that certain aromatics provide fuel droplets. Furthermore, the introduction of lower density, lower viscosity aromatics also have proven to improve atomization and lead to better combustion stability. The negative impact of better combustion stability is the increase in PM, NO_x, and other aromatic induced emissions. Therefore, a strategic fuel blend mix should be employed to reach the optimal combination of emissions and combustion stability.

CHAPTER 4

METHODS

4.1 Overview

Numerical and experimental procedures have been recorded to ensure repeatability of the experiments conducted. The numerical boundary conditions and meshing considerations were recorded in the following section, and the equipment used in the experimental testing can be found in the Appendix.

4.2 Numerical Modelling and Simulation

4.2.1 Turbulence Modelling

To properly model the phenomenon occurring the turbine, it is necessary to implement an appropriate turbulence model to capture the effects turbulence has on the many variables studied throughout this experiment. The turbulence, or the fluctuations in the flow field, occurs when the inertial forces of the flow overcome the viscous forces. The Navier-Stokes equation's usefulness in modeling this turbulence is limited due to computational requirements. Therefore, turbulence models have been created to simplify the computational requirements. These models work by reducing the velocity component into an averaged component and a time dependent component (ANSYS 2011a). This can be seen below.

$$U_i = \bar{U}_i + u_i \quad \text{Eq 1}$$

In this equation U_i is the velocity component, and it is divided into the averaged velocity, \bar{U}_i , and the time dependent component u_i . The average velocity component is derived from Eq 2, which determines the velocity fields across the element (ANSYS 2011a).

$$\bar{U}_i = \frac{1}{\Delta t} \int_{\Delta t}^{t+\Delta t} U_i dt \quad \text{Eq 2}$$

In determining the average velocity component, Δt is the timescale. This must be large compared to the turbulent fluctuations, but small compared to the total timescale.

The turbulence models use several foundational equations, along with assumptions, to predict the turbulence and its effect on the surrounding system. These equations are the continuity, momentum, and total enthalpy equations, seen below (ANSYS 2011a).

$$\frac{\partial \rho}{\partial t} + \nabla * (\rho U) = 0 \quad \text{Eq 3}$$

$$\frac{\partial(\rho U)}{\partial t} + \nabla * (\rho U \otimes U) = -\nabla \rho + \nabla * \tau + S_M \quad \text{Eq 4}$$

$$\frac{\partial(\rho h_{tot})}{\partial t} - \frac{\partial \rho}{\partial t} + \nabla * (\rho U h_{tot}) = -\nabla * (\lambda \nabla T) + (U * \tau) + U * S_M + S_E \quad \text{Eq 5}$$

These equations must then be modified to reduce computational requirements. This is done by using the averaged quantities of the different parameters in the equations (as determined in Eq 2). The result is the Reynolds Averaged Navier-Stokes (RANS) equations. These models are defined as statistical turbulence models. Despite this reduction in computation requirements, these equations still offer complexity in determining the accurate turbulent outcomes. Therefore, the introduction of turbulent models, like the k- ϵ turbulence model, can be used as support models and are useful in providing closure to the equations.

The k- ϵ turbulence model alters Eq 3, Eq 4, and Eq 5 to provide the necessary closure to solve the equations (ANSYS 2011a). The continuity, momentum, and total enthalpy equations can be reworked as seen below in Eq 6, Eq 7, and Eq 8.

$$\frac{\partial \rho}{\partial t} + \frac{\partial}{\partial x_j} (\rho U_j) = 0 \quad \text{Eq 6}$$

$$\frac{\partial(\rho U_i)}{\partial t} + \frac{\partial(\rho U_i U_j)}{\partial x_j} = -\frac{\partial(\rho)}{\partial x_i} + \frac{\partial}{\partial x_j} (\tau_{ij} - \rho \overline{u_i u_j}) + S_M \quad \text{Eq 7}$$

$$\frac{\partial(\rho h_{tot})}{\partial t} - \frac{\partial \rho}{\partial t} + \frac{\partial}{\partial x_j} (\rho U_j h_{tot}) = \frac{\partial}{\partial x_j} \left(\lambda \frac{\partial T}{\partial x_j} - \rho \overline{u_j h} \right) + \frac{\partial}{\partial x_j} [U_i (\tau_{ij} - \rho \overline{u_i u_j})] + S_E \quad \text{Eq 8}$$

The continuity and momentum equations are modified to contain the turbulent stress, designated by $\rho \overline{u_i u_j}$. The total enthalpy equation is also modified to contain the temperature changes due to the

turbulent mixing. It is also altered to include the viscous work that is produced. These terms are represented by $\rho\overline{u_j h}$ and $\rho\overline{u_i u_j}$, respectively (ANSYS 2011a). Furthermore, the total enthalpy can be represented by Eq 9 and Eq 10, where the turbulent kinetic energy (k) can be derived.

$$h_{tot} = h + \frac{1}{2} U_i U_i + k \quad Eq\ 9$$

$$k = \frac{1}{2} \overline{u_i^2} \quad Eq\ 10$$

The additional variable (Φ) can also be introduced into the momentum equation. The addition of this variable allows for the ability to solve for the Reynolds flux, which is denoted by $\rho\overline{u_j \Phi}$ in Eq 11.

$$\frac{\partial(\rho\Phi)}{\partial t} + \frac{\partial(\rho U_j \Phi)}{\partial x_j} = -\frac{\partial}{\partial x_i} \left(\Gamma \frac{\partial(\Phi)}{\partial x_j} - \rho\overline{u_j \Phi} \right) + S_\Phi \quad Eq\ 11$$

With the Reynolds flux introduced, the use of a turbulence model can now be implemented to provide closure to the governing equations by solving for the Reynolds stress and Reynolds's flux. This can be done with two types of models, Reynolds Stress models or Reynolds Viscous models. This simulation will focus on the latter.

The Eddy Viscosity Turbulence model assumes that turbulence is caused by vortices that form and dissipate over time. These Reynolds stresses created by the vortex is then assumed to be proportional to the mean velocity gradients. These assumptions dictate the solving of the model. One of the Eddy Viscosity models is the k-epsilon turbulence model. This model uses the introduction of turbulent kinetic energy (k) and turbulent eddy dissipation (ϵ) to solve the momentum equations and provide the outputs. The turbulent kinetic energy is described as the variance of the fluctuations of the flow, while the turbulent eddy dissipation is described as the rate at which the velocity fluctuations dissipate (ANSYS 2011a).

In applying this model to the transport equations, the continuity equation remains similar to the original, while the momentum equation is slightly altered to include the modified pressure value (p') and the effective viscosity (μ_{eff}). This can be seen in Eq 12.

$$\frac{\partial(\rho U_i)}{\partial t} + \frac{\partial(\rho U_i U_j)}{\partial x_j} = -\frac{\partial(p')}{\partial x_i} + \frac{\partial}{\partial x_j} \left[\mu_{eff} \left(\frac{\partial(U_i)}{\partial x_j} + \frac{\partial(U_j)}{\partial x_i} \right) \right] + S_M \quad Eq 12$$

The effective viscosity and the modified pressure are the viscosity and pressure, respectively, resulting from the turbulence of the flow. This can be represented by Eq 13, Eq 14, and Eq 15.

$$\mu_{eff} = \mu + \mu_t \quad Eq 13$$

$$\mu_t = C_\mu \rho \frac{k^2}{\varepsilon} \quad Eq 14$$

$$p' = p + \frac{2}{3} \rho k + \frac{2}{3} \mu_{eff} + \frac{\partial(U_k)}{\partial x_k} \quad Eq 15$$

In Eq 17, C_μ is a k- ε turbulence model constant and μ_t is the turbulent viscosity of the fluid. Finally, the governing equations that define k and epsilon can be generated and can be seen below in Eq 16 and Eq 17 respectively.

$$\frac{\partial(\rho k)}{\partial t} + \frac{\partial(\rho U_i k)}{\partial x_j} = \frac{\partial}{\partial x_j} \left[\left(\mu + \frac{\mu_t}{\sigma_k} \right) \frac{\partial(k)}{\partial x_j} \right] + P_k - \rho \varepsilon + P_{kb} \quad Eq 16$$

$$\frac{\partial(\rho \varepsilon)}{\partial t} + \frac{\partial(\rho U_i \varepsilon)}{\partial x_j} = \frac{\partial}{\partial x_j} \left[\left(\mu + \frac{\mu_t}{\sigma_\varepsilon} \right) \frac{\partial(\varepsilon)}{\partial x_j} \right] + \frac{\varepsilon}{k} (C_{\varepsilon 1} P_k - C_{\varepsilon 2} \rho \varepsilon + C_{\varepsilon 1} P_{\varepsilon b}) \quad Eq 17$$

In these equations, $C_{\varepsilon 1}$, $C_{\varepsilon 2}$, σ_k , and σ_ε are constant values determined by the CFX solver code. P_{kb} and $P_{\varepsilon b}$ represent the influence of buoyancy forces, and the P_k is the turbulence production due to the viscous forces, and is represented by Eq 18 (ANSYS 2011a).

$$P_k = \mu_t \left(\frac{\partial(U_i)}{\partial x_j} + \frac{\partial(U_j)}{\partial x_i} \right) \frac{\partial(U_i)}{\partial x_j} - \frac{2}{3} \frac{\partial(U_k)}{\partial x_k} \left(3\mu_t \frac{\partial(U_k)}{\partial x_k} + \rho k \right) \quad Eq 18$$

4.2.2 Combustion Modelling

The combustion modelling used for this simulation is the Eddy Dissipation Model (EDM). This model was chosen over other model types because of the accuracy and simplicity of the model as compared to Finite Rate Chemistry or Flamlet models. The EDM assumes the rate of the reaction is directly

proportional to the time required to mix the reactant. While in reality, the reaction occurs as soon as the reactants are brought together at a molecular level, EDM is still useful where the reaction rate is fast as compared to the mixing rate. This method also assumes the turbulence is the dominant force in the mixing rate. Therefore, Eq 19 shows the relationship between the turbulent flow and the reaction rate (ANSYS 2011a).

$$\text{rate} \propto \frac{k}{\varepsilon} \quad \text{Eq 19}$$

The rate of this reaction is necessary to determine. This rate is determined by the reaction limiter equation and the product limiter equation. Both can be seen below as equation Eq 20 and Eq 21 respectively.

$$R_k = A \frac{\varepsilon}{k} \min \left(\frac{[I]}{v'_{kl}} \right) \quad \text{Eq 20}$$

$$R_k = AB \frac{\varepsilon}{k} \min \left(\frac{\sum_P I W_I}{\sum_P v''_{kl} W_I} \right) \quad \text{Eq 21}$$

For the EDM model, the smallest value calculated from the two equations is used for the reaction rate. Many of these values are inputted as constants. I represents the species component for combustion, W_I represents the molar mass of I , $[I]$ represents the molar concentration of I , v'_{kl} and v''_{kl} represents the stoichiometric coefficients for reactions and products respectively, and $[A]$ and $[B]$ are the EDM coefficients (ANSYS 2011a).

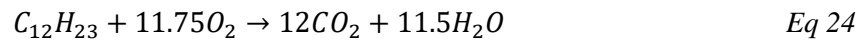
The Eddy Dissipation model used the Arrhenius equations to determine the rate of reaction within the simulation. The Arrhenius equation is used to describe the effect of temperature on the velocity of the reaction. The equation for this can be seen in Eq 22 below (ANSYS 2011a).

$$R = k * V * \prod_{\alpha=Reactants} \left(\frac{m_{\alpha}}{V} \right)^{n_{\alpha}} \quad \text{Eq 22}$$

The rate constant, designated by k , is determined by Eq 23 listed below.

$$k = A * T_p^m * \exp\left(-\frac{T_A}{T_p}\right) \quad \text{Eq 23}$$

To accurately employ the use of the EDM combustion model, reaction models were imported from the ANSYS CHEMKIN II reaction library supported by the ANSYS CFX software. The reactions were chosen based on their ability to accurately capture the energy and emissions output of the reaction while also maintaining computational efficiency. Because of this, three single step reactions were chosen to be implemented with two more multistep reactions that would combine the single step and improve the accuracy of the carbon monoxide production (ANSYS 2011b). The first reaction, seen as Equation 27, was used to indicate complete combustion of the fuel. This includes the combination of fuel and oxygen to produce carbon monoxide and water vapor. Equation 28 takes into account the incomplete combustion that occurs in combustion. This is represented by carbon monoxide combining with oxygen and water vapor to form carbon monoxide. Finally, Equation 29 is the production of nitrogen oxides at high temperatures. Shows the nitrogen in the system naturally combining with the oxygen in the system naturally at high temperatures to produce the nitrogen oxides.



4.2.3 Model and Mesh Development

The numerical model that was used for this experimentation was taken from previous work conducted in this field. The scaled SR-30 turbo jet engine CAD model was initially provided by Turbine Technologies as a SolidWorks file as seen Figure 24 in below.

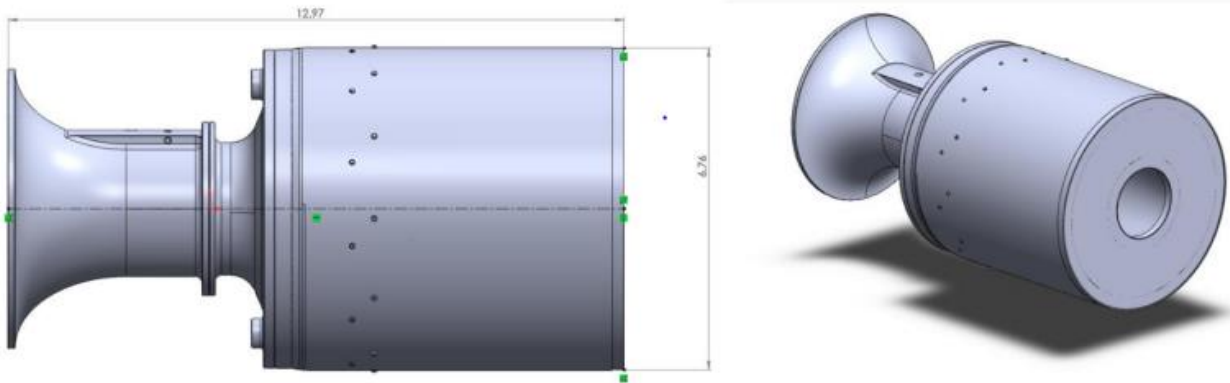


Figure 24: SolidWorks model of the scaled Turbine Technologies turbojet engine.

Significant work was performed to create the negative of the turbojet engine, including the creation of the injector, which were not present in the original CAD model (Grall 2021). Moreover, the presence of the bell-mouth inlet and the compressor section proved to be insignificant to the analysis of the combustion of the model. The increase in elements added a significant increase in the numerical model's calculation time, without improving the results in a significant way. Therefore, these portions were removed in favor of utilizing the combustion chamber, turbine, and exhaust section. The influence of the compressor section was set as a boundary condition to enhance the reality of the simulation. The final model that was created included the creation of a negative of the original CAD model with the addition of injector negative space with a spray cone angle of 60° . This can be seen below in Figure 25.

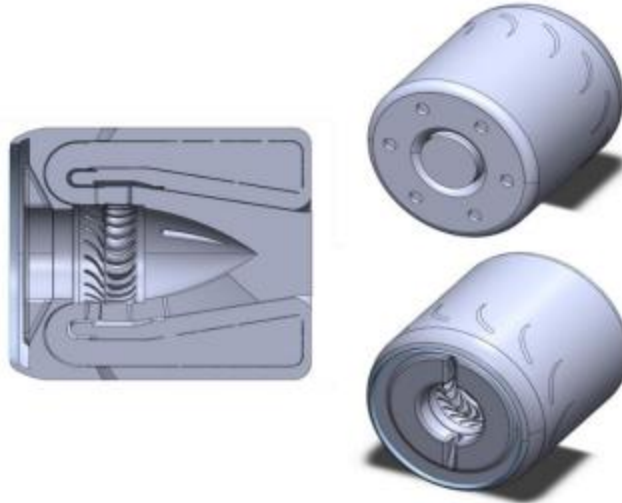


Figure 25: Final SolidWorks model of the turbojet engine.

The final solid model of the turbojet engine required an intentional effort to ensure the results gathered were based on the simulation boundary conditions and properties as opposed to being limited by the mathematical model made possible through the mesh. The numerical mesh was developed using ANSYS Mechanical meshing and was composed using tetrahedral elements. These elements were used due to the complexity of the geometry in the turbine and compressor section. A local face mapping and face sizing were applied to the body and face of all six injectors. This was done due to the relative small size of the injectors, which had a diameter of 0.006" and a length of 0.032" (Grall 2021). The local face mapping and face sizing improved the transition of the small elements in the injector to the relatively larger elements located in the combustion chamber. The final mesh resulting from this mesh control generated a mesh with approximately 748,591 elements and 157,703 nodes. This mesh control, as well as the final mesh for a cross-sectional view of the engine can be seen in Figure 26.

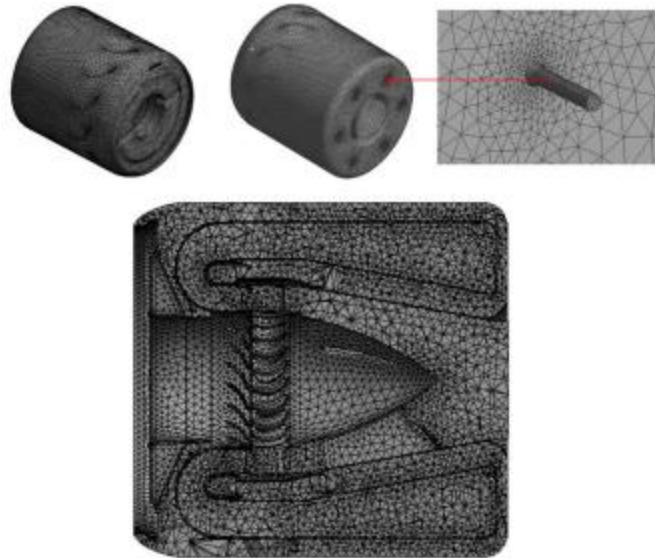


Figure 26: Numerical mesh for the final engine (top left and top middle), injector (top right) and cross-sectional view(bottom)

4.2.4 Boundary Conditions

The numerical boundary conditions for this simulation were created to accurately represent the physical conditions found in the experimental study. The model was created as a transient model with 20,000 timesteps. The timesteps were $0.05 \mu\text{s}$ in duration, resulting in a run time of 0.01 seconds. The RANS k-epsilon turbulence model was chosen for this simulation due to the flexibility of this model. This flexible and general-purpose model allows for time efficiency with accurate results that make it a general use turbulence model. This model was used with a medium (5%) turbulence option and uses an Eddy Dissipation Combustion model. There were four boundary conditions created for each simulation, including a no-slip wall, the compressor exit, fuel inlet, and turbine exit. The locations of each boundary condition can be seen in Figure 27 below.

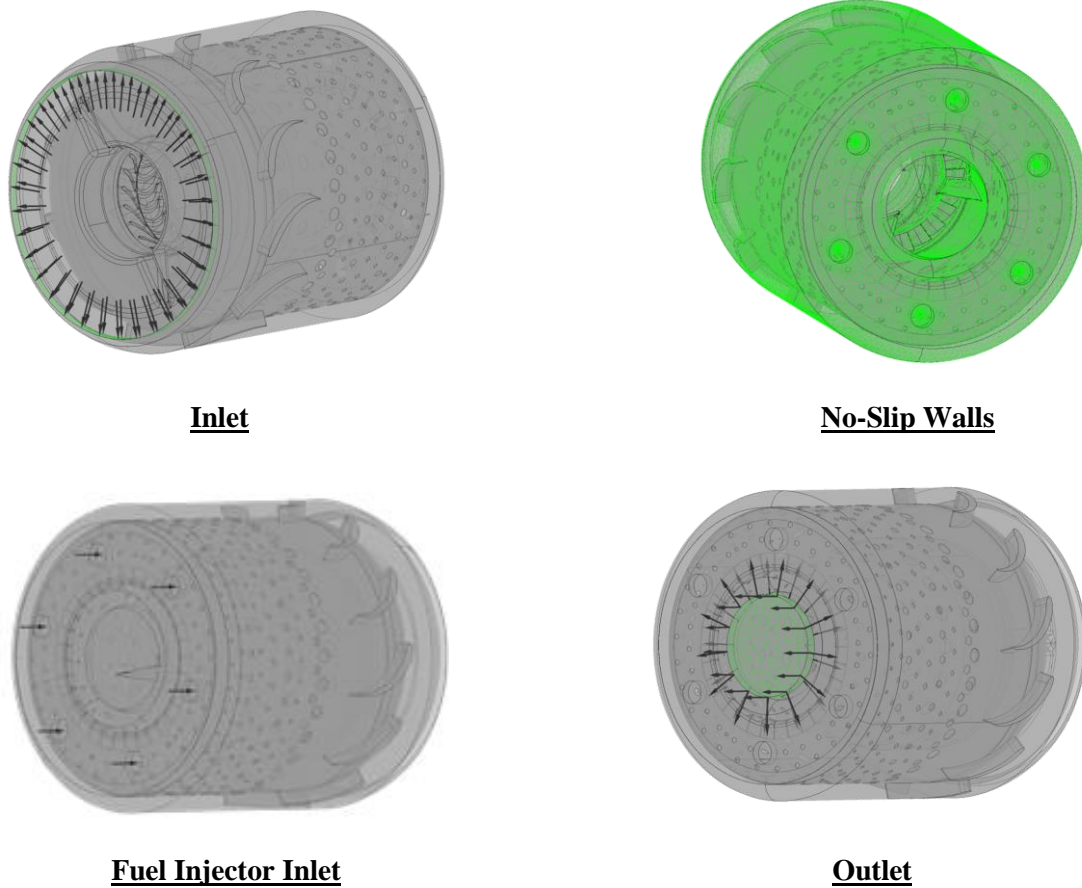


Figure 27: Boundary Conditions for the numerical models

When modeling the engine using transient simulations, the initial conditions were set, with the initial time set to 0 seconds. The initial condition for the velocity component of the Fuel Injector Inlet was set to 0 m/s, with the initial temperature and pressure in the simulation set to 300 K and 1 atm respectively. Moreover, the component details for the species in air were set to prior to ignition were set to mimic realistic conditions as well. CO_2 , H_2O , and O_2 were all set to a mass fraction of 0.01, 0.01, and 0.21 respectively. Although the carbon dioxide and water vapor initial condition may not necessarily be realist, the combustion model used requires the presence of the products in the system to begin the ignition (ANSYS 2011b, 304). Furthermore, this defaulted the nitrogen mass fraction value to 0.77. The boundary conditions as described below in Table 1, reflect measured and calculated conditions from the experimental tests.

Table 1: Boundary Conditions for the Numerical Simulations

Boundary Conditions			
Boundary	Compressor Exit	Fuel Inlet	Turbine Exit
Boundary Type	Inlet	Inlet	Outlet
Mass Flow Rate [kg/s]	0.32 - 0.44	~	~
Normal Speed [m/s]	~	104.7 – 106.4	~
Static Temperature [K]	328 - 477	300	~
Static Pressure [Pa]	~	~	3,337 - 17,023
Species Mass Fraction: O ₂	0.21	0	~
Species Mass Fraction: Jet-A	0	1	~
Species Mass Fraction: F-24	0	1	

Furthermore, when setting the two different numerical models (one model for Jet-A, and the second for F24), the fuel was changed to match the corresponding fuel for the test. Since F24 was derived from Jet-A, it is collectively understood that Jet-A and F24 are practically the same fuel (Ryu et al. 2020, Amezcua et al. 2022, Guzman and Brezinsky 2021, FAA 2014). Furthermore, it is also well understood that JP-8 and Jet-A are also very similar in molecular structure (Marines 2014, Ryder et al. 2010). Therefore, F24 was modelled by altering the NASA Polynomials of the default Jet-A fuel as is described by the ANSYS Model Fuel Library, and replaced with the NASA Polynomials that are experimentally derived for JP-8 by the research conducted by Xu et al (Rui Xu 2015). The lower, midpoint and upper temperatures values were all altered as well to the values described in the aforementioned research. The molecular weight for F24 was altered to match the molecular weight values that have been found in literature and experimental measurements (Ryu et al. 2021). The NASA Polynomials for the ANSYS Jet-A fuel and the F24 fuel that were used in the numerical modelling can be found below in Table 2.

Table 2: NASA Polynomial data of Jet-A and F24

Parameter	Jet-A	F24
Molecular Weight (g/mol)	167.31462	167.6
Lower Temp (K)	273.15	298
Midpoint Temp (K)	1000	1000
Upper Temp (K)	5000	3000
Upper Coefficients		
a1	2.4880201E+01	2.5974230E+01
a2 (K ⁻¹)	7.8250048E-02	5.5462092E-02
a3 (K ⁻²)	-3.1550973E-05	-1.7337738E-05
a4 (K ⁻³)	5.7878900E-09	1.7582452E-09
a5 (K ⁻⁴)	-3.9827968E-13	6.3971899E-14
a6 (K)	-4.3110684E+04	-4.6337805E+04
a7	-9.3655255E+01	-1.1004780E+02
Lower Coefficients		
a1	2.0869217E+00	4.7049127E+00
a2 (K ⁻¹)	1.3314965E-01	5.8911327E-02
a3 (K ⁻²)	-8.1157452E-05	1.0500014E-04
a4 (K ⁻³)	2.9409286E-08	-1.8501088E-07
a5 (K ⁻⁴)	-6.5195213E-12	8.2238431E-11
a6 (K)	-3.5912841E+04	-3.7391863E+04
a7	2.7355289E+01	1.3439449E+01

Data collection and analysis was conducted by running six different simulations. The independent variables for the series of tests were the fuel type (Jet-A and F24) and the engine speed (60,000, 65,000, and 70,000 RPM). The data was collected and processed using ANSYS CFX-Post, where a state file (.cst) was used to ensure the same ranges and graphs were produced from the data set. The parameter contour plots were collected across a plane that was oriented to intersect with the centroids of the two fuel injectors on opposite radial sides of the engine as seen in Figure 28. This data collection plan ensured the spray development of the vaporized fuel can be easily visualized. This also ensures an accurate representation of the temperature, pressure, and other engine characteristics across each simulation.

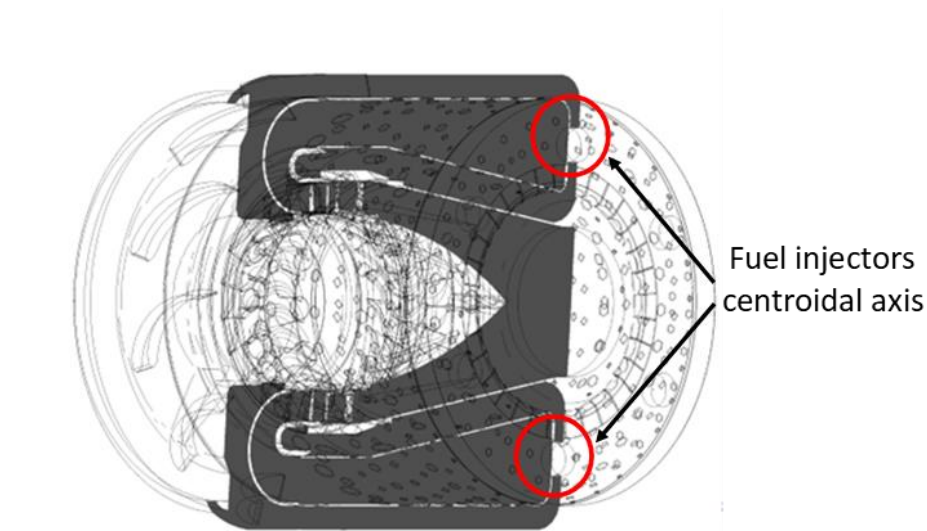


Figure 28: Plane of data collection for the numerical simulation.

The data to compare the experimental and numerical results were collected at similar locations around the engine as the physical locations of thermocouples. These locations were measured based on the physical engine and then correlated to the numerical model position to reduce variation in the results. The location of each point can be seen Figure 29 in below.

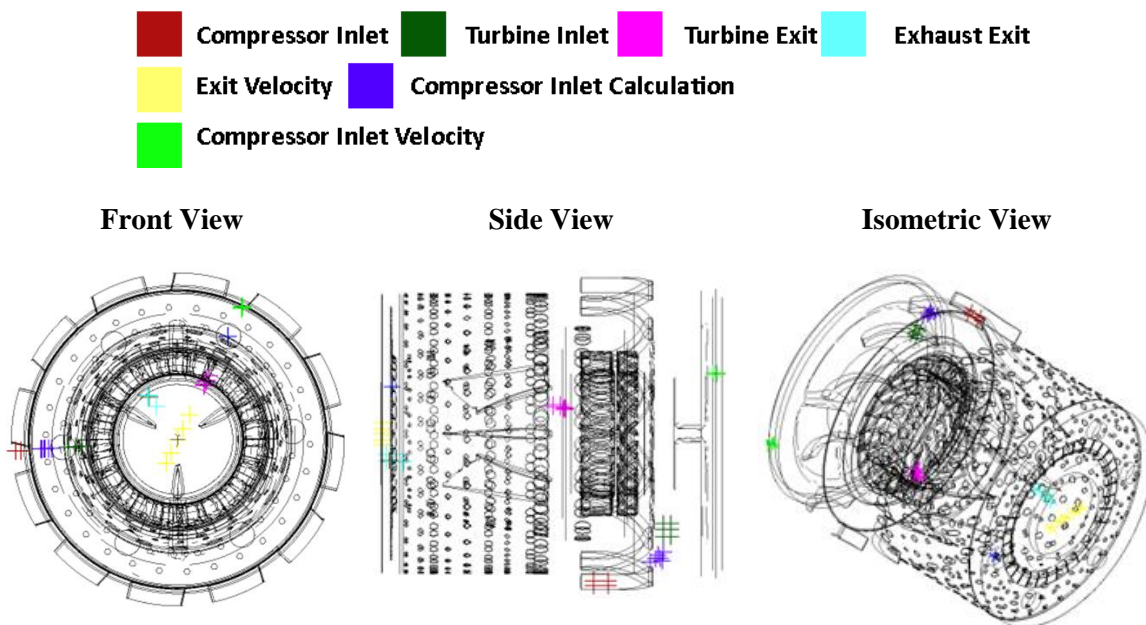


Figure 29: Data collection points for numerical and experimental comparison.

4.2.6 Solver Equipment and Procedures

To reduce computational time and improved efficiency of the initial simulation phases, the numerical model was solved using a High-Performance Talon Cluster provided by Georgia Southern University's Computational Research Technical Support Center. The Cluster is comprised of 35 Dell PowerEdge servers, 92 physical CPU's and 289 cores across all CPU's (Valentin Soloiu 2024). The setup also utilizes Intel HyperThreading technology that presents 1184 virtual CPU's and a total of 5 TB of RAM across all servers (Valentin Soloiu 2024). Each simulation was solved using 96 cores on a single CPU. This method of simulation rapidly reduced the computational time, resulting in solve time of approximately 10 hours for each simulation. This allowed for the solving of multiple different simulation setups to determine the optimal settings that provided the most accurate results.

4.3 Physical Experimental Setup and Procedure

4.3.1 Fuel Characterization Methodology

The thermophysical properties of Jet A and F24 were evaluated using multiple ASTM standardized testing that was conducted in house. These tests were conducted to ensure the fuel properties were within the range that is expected for these fuels to obtain accurate experimental result. They were also performed to ensure the accuracy of the input material properties, which can have a measurable effect on the combustion and emissions results. The following properties were measured and extrapolated: dynamic and kinematic viscosity, density, freezing point, lower heating value, droplet size, thermogravimetric and differential thermal analysis, derived cetane number, ignition delay, and combustion delay.

4.3.1.1 Brookfield Viscometer DV-II +Pro

The viscosity of a fuel has a great impact on the combustion and emissions properties of different fuels as they are burned. A high viscosity fuel represents a fuel that resists motion to a higher degree than

lower viscosity fuels. This can have a negative effect on the fuel injection system. First, a high viscosity fuel requires pumps to input a higher amount of work to move the fluid a nominal amount. Moreover, it affects the spray atomization of the fuel as well. High viscosity fuels tend to form in larger droplets than the droplets of low viscosity fuels. These larger fuel droplets results in poor combustion efficiency, as higher flame temperature and heat energy is required to ignite the larger droplets of fuel (Sallevelt et al. 2014). When all the fuel is not burned in the combustion chamber, the results can be higher levels of soot and total hydrocarbons in the emissions. The dynamic viscosity measurement of Jet A and F24 in this work was measured using the Brookfield Viscometer DV-II +Pro.

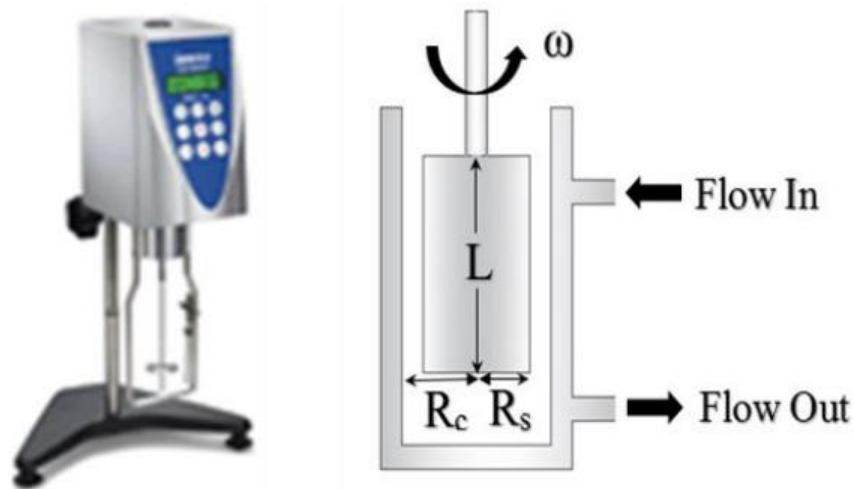


Figure 30: Brookfield DV-II +Pro Rotational Viscometer (Grall 2021)

This measuring device determines the viscosity of a fluid based on the amount of torque required to rotate a fluid specific spindle while submerged in approximately 7 mL of the fuel. As the spindle rotates, the fuels is cycled through a heater which gradually raised the temperature from 26°C to 90°C in increments of 2°C. Data is collected using the Rheocalc software, which collects the rotational velocity of the spindle and calculates the shear rate and shear stress at the surface of the spindle. Using the equations below, the dynamic viscosity (η) can be calculated in Pa*s.

$$\dot{\gamma} = \frac{2\omega R_c^2}{R_c^2 - R_s^2}$$

Eq. 19

$$\tau = \frac{M}{2\pi R_s^2 L}$$

$$\eta = \frac{\tau}{\dot{\gamma}}$$

In the equation above, $\dot{\gamma}$ is the shear rate in s^{-1} , ω is the angular velocity in $\frac{rad}{s}$, R_c and R_s are the radii of the container and spindle respectively in meters, L is the length of the cylinder in meters, M is the motor torque in Nm, τ is the shear stress in $\frac{N}{m^2}$, and η is the dynamic viscosity in Pa*s (Roylance 2000)

4.3.1.2 Phase Technology JFA-70Xi AS

When discussing fuel combustion efficiency, emissions, and applications of a fuel, the density, freeze point, and kinematic viscosity are important aspects of a fuel. The kinematic viscosity is a ratio between the dynamic viscosity and density, which represents the speed fluids move when a known force is applied to the fluid (2020). This is particularly important when discussing pump power of fuel systems. The freeze point is another important variable of fuel properties. An increase in altitude comes with a decrease in temperature, which can cause engine failure. Furthermore, the density is a vital part of fuel thermochemistry. The density of a fuel is inversely proportional to the viscosity, where low density fuels are typically less viscous. This improved viscosity improves fuel atomization, but often comes with the negative effect of having a lower specific energy content. This decrease energy content results in a lower thrust specific fuel consumption. To determine these thermochemical properties, the Phase Technology JFA=70Xi AS was used to measure the kinematic viscosity, density, and freezing point.

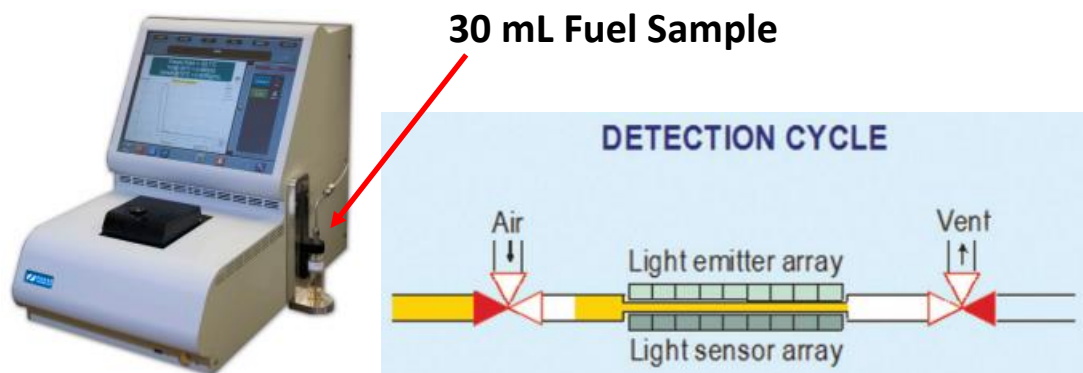


Figure 31: JFA-70XI AS 3-in-1 Jet Fuel Analyzer (Gordon Chiu 2018)

The JFA-70 Xi AS cools a 30 mL fuel sample in the standard described in ASTM D5773. A cloud point temperature is then obtained where the smallest observable cluster of hydrocarbons (wax) crystals form. At this point, the sample is cooled rapidly, observing the initial crystal formation that is detected based on the rise in signal feedback from the optical system. The JFA then rapidly heats the sample until the wax crystals disappear and cools the sample once more at a slower rate to detect the same optical signal again. At this temperature, the viscosity is determined. The freeze point is also determined using ASTM 5972 test method. For this test, the fuel sample is quickly cooled until solid hydrocarbon crystals are formed. The device then warms the sample until the crystals disappear. This is then recorded as the freeze point (Co. 2017)

4.3.1.3 Shimadzu DTG-60

A thermal gravimetric analysis (TGA) and differential thermal analysis (DTA) are measurement tests performed to determine the fuel samples low temperature oxidation characteristics (TGA) and the exothermic and endothermic reactions that occurs over a temperature range (DTA). The TGA and DTA results are valuable for better understanding the volatility of fuel at low temperatures. Research shows high volatility fuels result in a more homogenous fuel-air mixture (Yousufuddin 2016, Kalvakala et al. 2022). The Shimadzu DTG-60 was used to perform the TGA-DTA analysis on Jet A and F24.

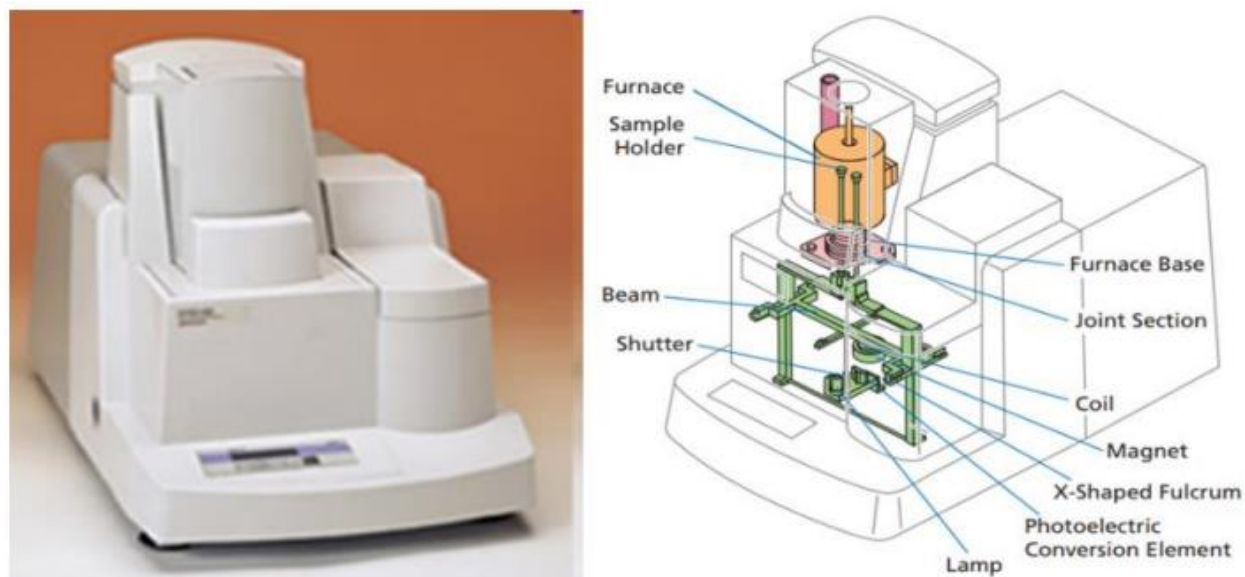


Figure 32: Shimadzu DTG-60 ((Shimadzu 2023))

This instrument can be used to better understand the physical and chemical properties of sample fuel such as transition temperature, melting point, temperature of reaction, and the change in mass of a sample through a varied temperature range. The temperature range for this analysis was conducted from 23°C to 600°C with a temperature increase at 20°C per minute. A constant nitrogen flow rate of 15 mL/min is used to purge the fumes generated by the fuel oxidation. An inert alumina powder was used as a reference to measure the change in mass of the fuel sample over the temperature range. As the temperature in the furnace is increased, the mass loss of the fuel can be measured using the accurate reference of the alumina powder. This correlates to the vaporization of the fuel. The heat release is also measured throughout the temperature range to show the endothermic and exothermic reactions that occur.

4.3.1.4 Malvern MIE Scattering He-Ne Laser

The combustion of fuel is highly dependent on the droplet size and frequency of the fuel injected. Measuring the droplet formation of different fuels is a valuable piece of information that can provide important insight into combustion efficiency and emissions. As previously discussed, the size of the fuel

droplet injected into the combustion chamber can have significant effects on the combustion efficiency and emissions, where larger droplets produce inefficient combustion and results in higher concentrations of soot and total hydrocarbons. The Malvern MIE Scattering He-Ne Laser was used to analyze the droplet distribution, mixture formation, and spray atomization of Jet A and F24. This laser uses the Fraunhofer diffraction theory and Mie scattering is used to analyze the data. Using these methods, the Sauter Mean Diameter of the fuel spray as diffracted by the laser can be interpreted (Engineering 2023). The equation used to determine the SMD can be seen below in Eq. 20.

$$I(\theta) = \frac{I_o}{2k^2a^2} * ([S_1(\theta)]^2 + [S_2(\theta)]^2) \quad \text{Eq. 20}$$

In this equation above, $I(\theta)$ represents the light intensity as a function of the angle the light hits the droplets. The parameters $S_1(\theta)$ and $S_2(\theta)$ represent the dimensionless complex function that represent the change in amplitude from the perpendicular and parallel polarized light. The distance between the light detector and emitter is represented by a . The wavenumber is represented by k can also be express as $\frac{2\pi}{\lambda}$. The Fraunhofer diffraction theory equation can be seen in the equation below.

$$I(\theta) = \frac{I_o}{2k^2a^2} * a^4 * \frac{J_1\alpha \sin(\theta)}{\alpha \sin(\theta)} \quad \text{Eq. 21}$$

This diffraction theory was chosen due to its synonymous treatment of droplets of varying shapes and sizes without reference to the optical properties. The terminology as described for the Mie Scattering equation also applies to this equation, with the addition of α , which can be represented by $\pi x/\lambda$ where x is the particle size. The experimental setup for the SprayTec can be seen in Figure 33 below.

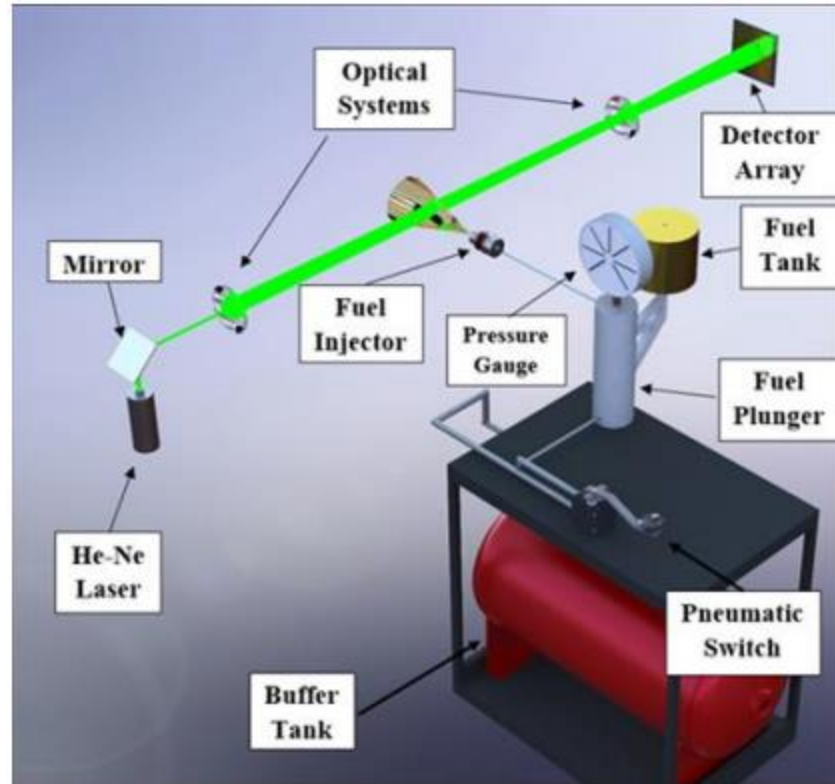


*Figure 33: Malvern Spraytec with Mie & Fraunhofer Scattering, He-Ne Laser Experimental Setup
(Valentin Soloiu 2024)*

This instrument uses light detectors that sample at 10 kHz, and a laser beam that has fuel sprayed through it with a Bosch pintle-type fuel injector. The fuel injector is positioned 100mm away from the laser beam and begins collecting data using a trigger set to collect data 0.1 ms before the injection, and up to 5 ms after injection. The injection pressure is set at 180 bar and uses an electric actuator to ensure repeatable sprays. The light receiver is made up of 36 light detectors with a 300 mm diameter. This allows for the measurement of droplet sizes as small as 900 μm . As the spray breaks the laser beam, the diffraction of the light allows for the measurement of the pattern and magnitude of the light intensity as it impacts the receiver (Engineering 2023). This allows for the calculation of the SMD and droplet size distribution. The Spraytec software is used to setup and process the experiment and data.

4.3.1.5 Petroleum Analysis Company CID 510

Aside from the inferences that can be made from investigation the fuel properties like viscosity, density, and droplet size, the combustion properties of fuels can also be examined using the PAC DID 520 Constant Volume Combustion Chamber. The PAC CVCC measures the ignition delay, combustion delay, and pressure inside the chamber after fuel injection to mathematically determine the Cetane number and the Average Heat Release Rate of the fuels. The values of these parameters can have a significant effect on the combustion efficiency of the fuels. Cetane number refers to the proclivity of a fuel to ignite, where the standard for diesel fuel is between 40-45 generally speaking (Dianne Luning Prak 2021). The range of Cetane numbers is between 0-100, where 0 is the least reactive, and 100 would be most reactive. Therefore, lower cetane fuels allow for a more controlled and efficient combustion, which improves the engine efficiency as well as reducing production of harmful emissions (EIP 2022).

The PAC CVCC uses a Petroleum Analysis Company CID 510 combustion chamber. A LAUDA Alpha RA chiller is used to heat and cool the system as needed. Ultra-High Purity compressed N₂ and O₂ gases are used to fill the combustion chamber. Approximately 160 mL of fuel is used to conduct the testing and is injected into the combustion chamber at a pressure and temperature of approximately 1000 bar and 600°C respectively. The pulse-width duration of the injection is 2.5 ms. Figure 34 below shows the internal components of the measuring device. It is comprised of a common rail fuel injection system (1 on the right) which supplies fuel to the Bosch 6 high pressure fuel injector (2 on the right). The constant volume combustion chamber (2 on the left) is fully heated to a nominal temperature and the pressure inside the chamber is controlled and monitored. A pressure sensor (3 on the left) is used to measure the pressure before, after, and during the fuel testing, and the fuel line pressure is measured with a different pressure senso (4 on the left).

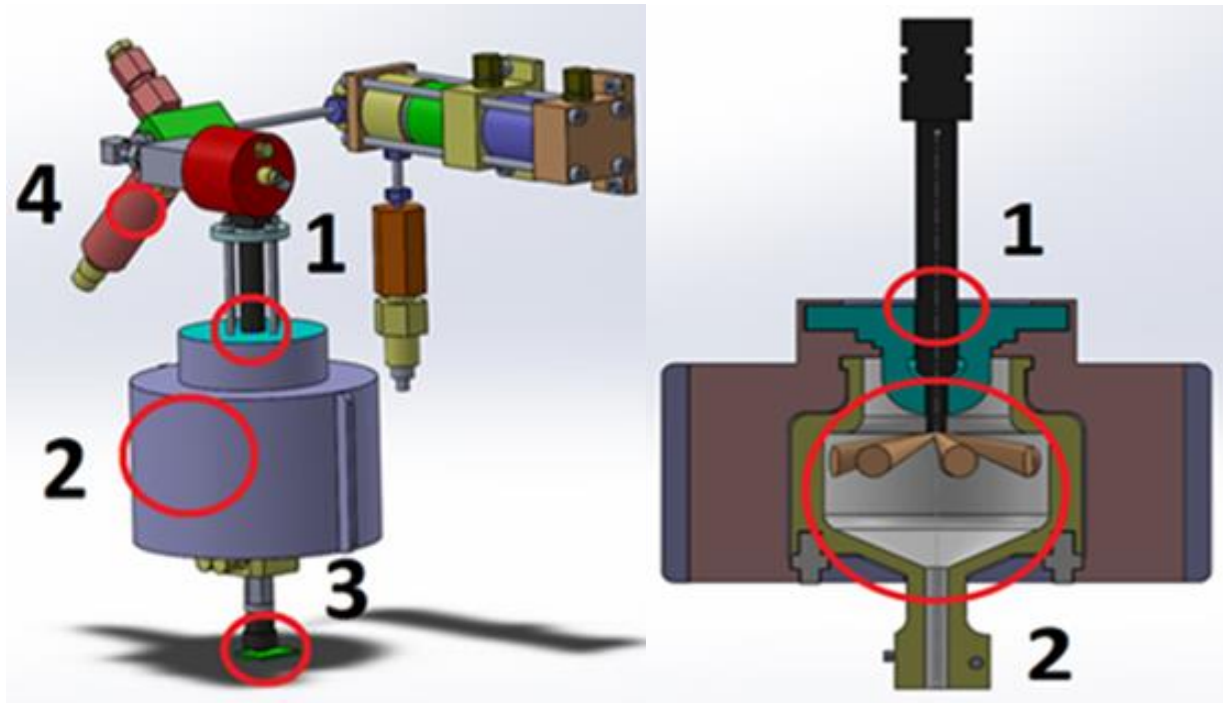


Figure 34: Constant Volume Combustion Chamber Schematic (Valentin Soloiu 2024)

The testing of the fuels is conducted by first conditioning the pressure and temperature inside the chamber to match the ASTM D7667-14A test standards seen in Table 3 below. The device performs 5 cycles of injection, combustion, and exhaust to condition the chamber to a nominal level. Measurements are then taken for 15 combustion cycles. Pressure data is averaged across all tests.

Table 3: ASTM D78668-14a Standard Testing Parameter in the Constant Volume Combustion Chamber

ASTM Reference Parameters	
Combustion Chamber Wall Temperature	595.5°C
Chamber Pressure	20 Bar
Injection Pulse Width	2500 μ s
Injection Pressure	1000 Bar
Coolant Temperature	50°C

The PAC CVCC uses the injection delay and combustion delay to determine the Derive Cetane Number of the fuel. The equation for determining these values can be found in the equation below.

$$DCN = 13.028 + \left(\frac{-5.3378}{ID}\right) + \left(\frac{300.18}{CD}\right) + \left(\frac{-12537.90}{CD^2}\right) + \left(\frac{3415.32}{CD^3}\right) \quad Eq. 22$$

4.3.1.6 Parr 1341 Constant Volume Calorimeter

The energy density of fuel is an important component of fuel chemistry that greatly effects the fuel injection process and emissions produced from burning fuels. One method of describing energy density in fuels is the lower heating value of the fuel. This LHV describes the amount of calorific energy that exists in a fuel after removing the energy produced by vaporization of the water produced in the chemical reaction process of oxidation (BYJU 2023). This property of fuel must be taken into account when analyzing the fuel and engine performance. For example, the fuel flow rate of high calorific fuel will be dramatically less for engine to reach a specific engine speed (Energy 2020). It can also have significant effect on the specific fuel consumption, combustion efficiency, and NOx emissions produced (B. Tesfa 2013).

The LHV was determined in this experimentation through the use of the Parr 1341 Constant Volume Calorimeter, a high precision digital calorimeter that is rated by ANSI for the 0.3% precision class. The Parr 1341 includes a plain insulated jacket with the Parr 6772 calorimetric thermometer that is used to monitor and control the device. Figure 35 shows the calorimeter used in the experiment with a cross sectional view of the device.

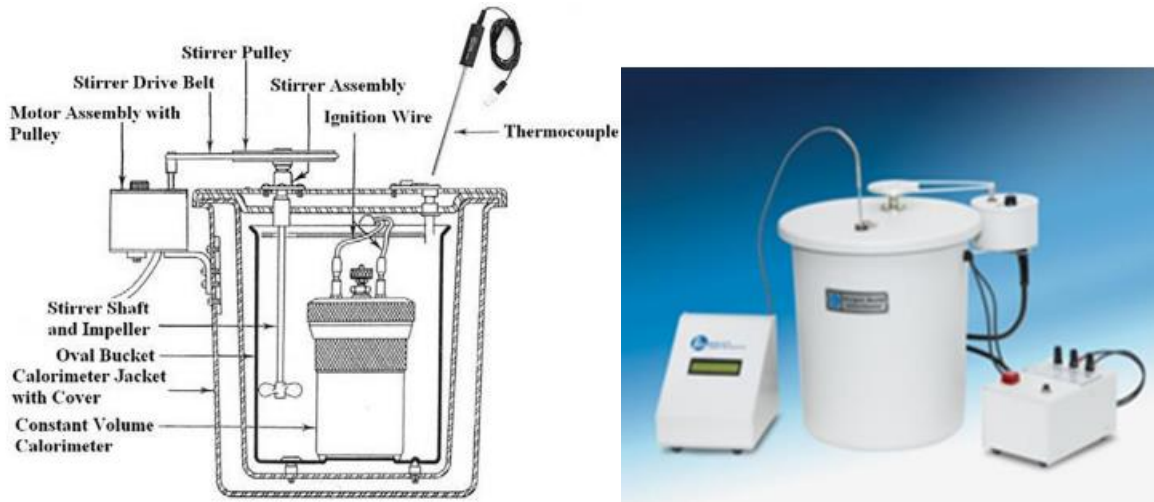


Figure 35: Parr 1341 Calorimeter with cross-sectional schematic(Parr_Instrument_Company 2021, 2014)

To conduct the test, the fuel sample of approximately 500 mg is placed inside the constant volume crucible. A Ni-alloy fuse wire with a commonly known energy density was placed between 2 electrodes and was used to ignite the fuel. The inner chamber was then sealed and pressured using 25atm of O_2 and inserted into a chamber filled with 2kg of deionized water. A k-type thermocouple measures the temperature of the water, and a stirring shaft circulates the water to ensure an even temperature distribution throughout the DI water. The heat produced from the ignition of the fuel transfers through the wall of the constant volume chamber and increases the temperature of the water. Based on the gross heating value (H_c) and the hydrogen percentage of the sample (H), the net heating value (H_{net}) can be calculated using the formula below.

$$H_{net} = 1.8HH_c - 91.23H \quad \text{Eq. 23}$$

4.3.2 Experimental Methods Overview of the Turbojet Engine Fueled with Jet-A and F24

4.3.2.1 Gas Turbine Experimental Setup

The experimental testing of the small-scale turbojet engine was conducted using the Minilab gas turbine power system developed by and purchased from Turbine Technologies. This small-scale turbojet engine is an ideal option for fuel and engine performance testing due to the low fuel consumption, noise pollution, and external requirements of the small-scale engine as compared to full scale models. The engine is comprised of a bell mouth inlet, a centrifugal compressor, reverse annular combustion chamber, a single turbine stage, and converging exhaust. The specifications of the engine can be found in Table 4 below.

Table 4: SR-30 Small-scale Turbojet Engine Specification

Maximum Engine Speed	87,000 rpm
Maximum Thrust	40lbs
Max Exhaust Gas Temperature	720°C
Mass Flow	0.5 kg/s
Pressure ratio	3.4:1
Specific Fuel Consumption	1.22 lb/lb-hr

This fully integrated testing system comes outfitted with numerous sensors and a data acquisition system to measure and collect the required data. This data can be monitored in real time and stored by using the LabView software developed and provided by Turbine Technologies. The testing system uses 5 K-type thermocouples and 5 Setra Model 209 OEM pressure transducers distributed throughout the engine. Each section of the engine (inlet, compressor, combustion chamber, turbine, and exhaust) has a fully dedicated sensor to collect the data. A Futek model LLB400 button type load cell is mounted to the base of a frame that is used to collect thrust data, and the fuel flow rate is calculated using 2 Max Machinery P213 Piston type flow meters – one before fuel injection and the second after fuel injection. These two flow meters determine the flow differential, and the actual fuel flow rate is determined from these measurements. Finally, a pulse type tachometer is used to measure engine speed. All analog sensor signals are processed using a National Instruments USB-6218 Multifunction I/O DAQ, which feeds the digitized signals to the

MiniLab LabView program on the provided laptop and displays the data. The laptop is connected to the DAQ via a USB A-B cable and is placed a safe 6 feet away from the turbine perpendicular to the flow path. A schematic of the engine sensors and locations can be found in Figure 36 below.

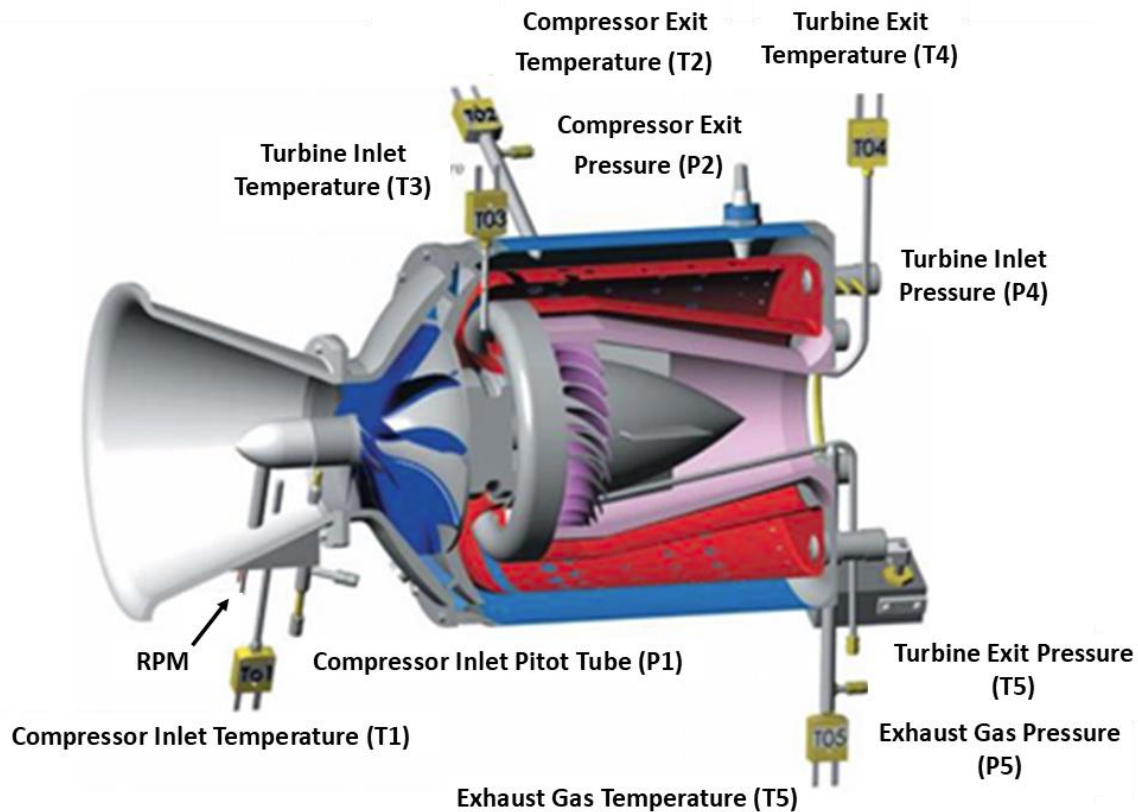


Figure 36: Location of each temperature and pressure sensor in the turbojet engine

(Turbine_Technologies 2011)

4.3.2.2 Emissions Experimental Setup

The emission data was collected using the MKS Multigas 2030 FTIR Gas Analyzer. This instrument can measure over 30 different species and can determine the prevalence of these species as a percentage per volume and part per million. This gas analyzer works by passing the exhaust gases through a high-optical-throughput gas cell and uses a long wavelength, thermoelectrically cooled IR wave to measure the absorption of the gas species (MKS_Instruments_Inc. 2020). Each species absorbs unique

amounts of spectral frequencies in the IR light. The gas analyzer can measure the amount of absorption spectrum of the gas and therefore measures the concentration of each species in the gas.

The Multigas MKS Gas Analyzer is purged with Ultra High Purity (UHP) nitrogen for a minimum of 8 hours prior to the test. After fully purging the system of all impurities in the gas cells, the MKS is moved to the test location to acclimate the gas cells to the ambient temperature and humidity levels. Per the Multigas MKS Gas Analyzer operator's manual, the ideal temperature and humidity operating range is between 50°F-75°F and 20%-60% humidity levels. However, the manual also states it is safe and accurate operating in much wider temperature and humidity ranges (32°F-104°F and 10%-90% humidity levels). Since testing occurred on different days, the ideal temperature levels were achieved, however the natural humidity of Statesboro, GA made reaching the ideal levels difficult. Humidity levels on the day of testing were within the allowed ranges of the testing equipment.

After being moved to the testing zone, liquid nitrogen was poured into the analyzer chamber and the supporting system were powered on. The heated line was then heated to the stable temperature of 191°C to eliminate condensation of the exhaust gases in the gas cells. This heated line was then connected to the turbine heat exchanger. This heat exchanger was employed to lower the exhaust gas temperature down from the average high temperatures of 630°C to 191°C. The temperature of the gas inside the heat exchanger was constantly monitored using PID's at each rung of the heat exchanger. This verified the gas temperature to be approximately 191°C. The heat exchanger was connected to the second fitting from the top of the heat exchanger. The full experimental setup for the emissions data collection can be seen in Figure 37 below.

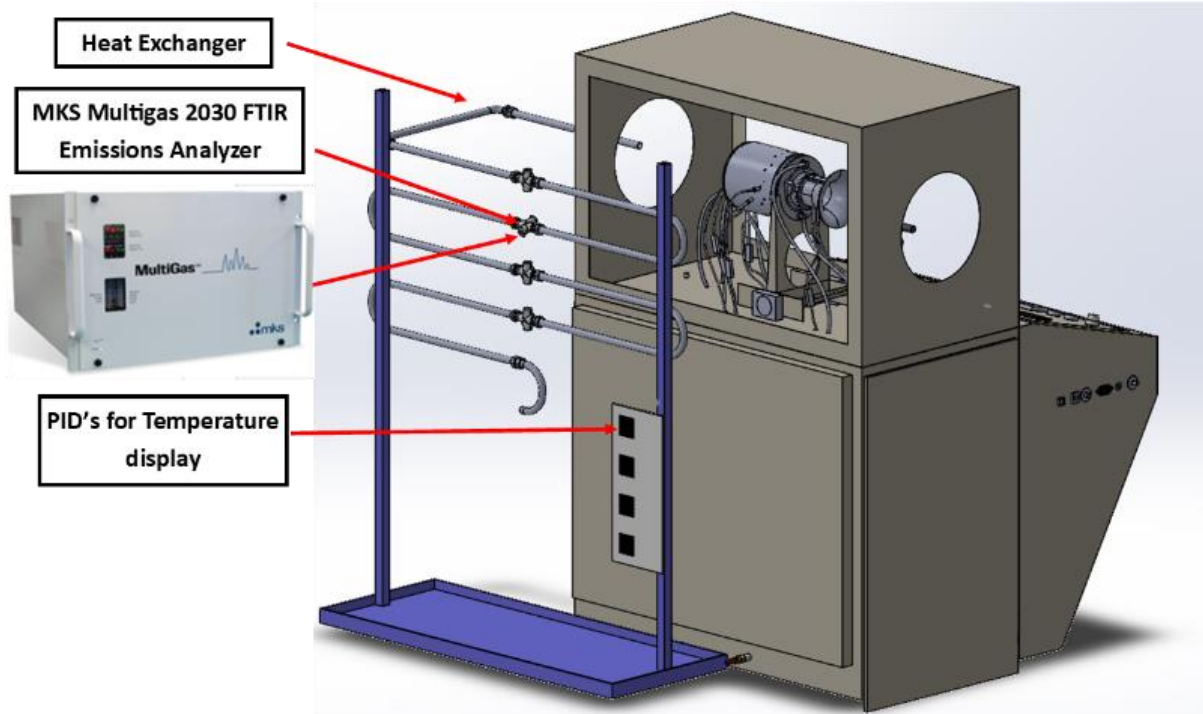


Figure 37: Emissions Experimental Setup

4.3.2.3 Noise and Vibration Experimental Setup

The noise and vibration data were collected using a collection of Hottinger Bruel & Kjaer products developed exclusively for NVH studies. The sound pressure data was measured using the HBK Type 4966 Prepolarized Free field 1/2" microphone and the HBK Type 4961 Multi-field 1/4" microphone. The specifications for each microphone can be found in Table 5 below.

Table 5: Specifications for Microphones

Microphone Type	4961 Multi-field 1/4"	4966 Free-field 1/2"
Temperature (°C)	23	23
Ambient Static Pressure (kPa)	101.3	101.3
Relative Humidity (%)	50	50
Frequency (Hz)	251.2	251.2

Polarization Voltage, external (V)	0	0
Combined Sensitivity (dB re 1 V/Pa)	-24.5	-27.2
Uncertainty 95% Confidence Level (dB)	0.3	0.2

The microphones were positioned in methods ideal to their design. The multi-field microphone performs best in more chaotic sound environments, while the free field microphone performs best when there is a single sound source. Therefore, the free field microphone was positioned 1 meter perpendicular from the combustor section of the turbine, while the multifield microphone was positioned 1 meter away and at a 45° angle from the exhaust section of the turbine. The microphones were fixed on tripods at a height of approximately 1.2 meters to be near the geometric center of the turbine engine. The experimental tests were performed in an outdoor test environment to minimize the effects of the sound reflection. A diagram of the microphones for the experimental test can be found in Figure 38 below.

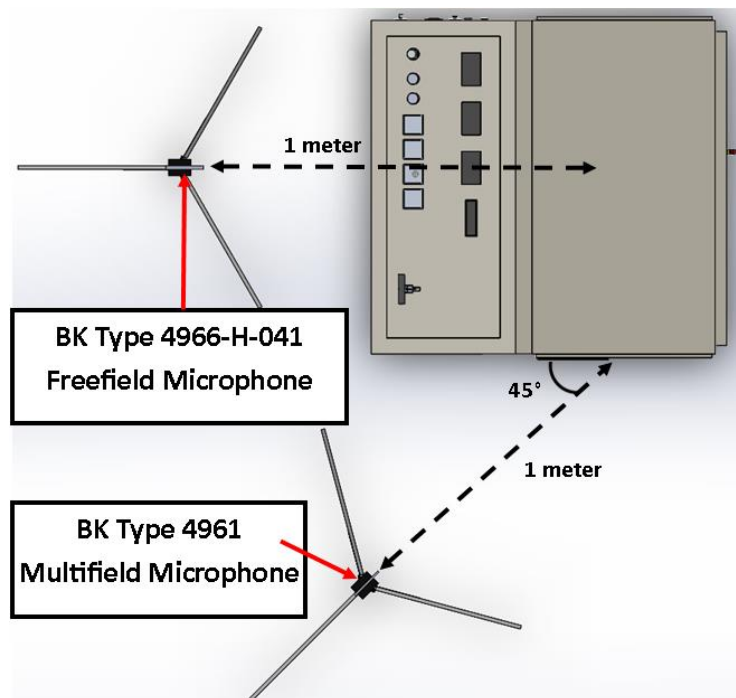


Figure 38: Microphone layout in the experimental setup.

The vibration of the turbine was measured in the X, Y, and Z axis using a HBK Type 4527 Triaxial Deltatron Accelerometer. The Triaxial Accelerometer was fixed to the turbine frame using a small supporting magnetic base. The accelerometer was mounted approximately 2 inches from the top of the turbine frame. The magnetic base was more thoroughly fixed with the assistance of a negligible amount of tape to secure the accelerometer to the frame. Finally, the accelerometer was positioned so that the X direction was parallel to the flow path of the engine. The accelerometers' location on the engine frame can be seen in Figure 39 below.

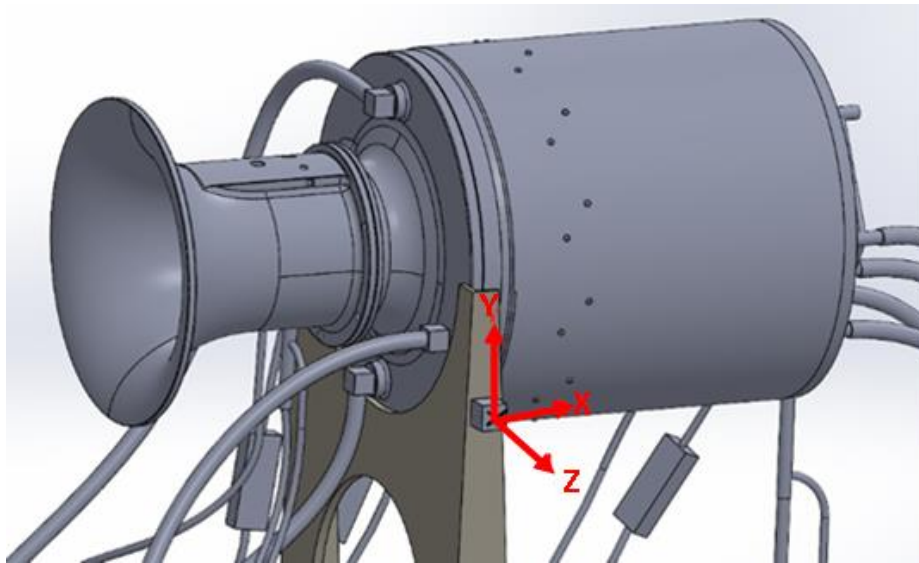


Figure 39: Location and orientation of the Triaxial Accelerometer

All noise and vibration equipment were connected to the HBK LAN-XI Data Acquisition System with a 6-channel input module. The accelerometer connected to the BNC connection on the DAS with a 3-way split cable to capture each direction of vibration, and the microphones were connected via a SMB microphone to coaxial cable. The HBK LAN-XI DAS was connected to the BK supplied Dell Laptop with the BK Connect software installed. This software allowed for the monitoring and recording of the sound pressure and vibration data. A model of the full experimental setup can be seen in Figure 40 below and the actual experimental setup including the emissions apparatus can be found in Figure 72 in Appendix A

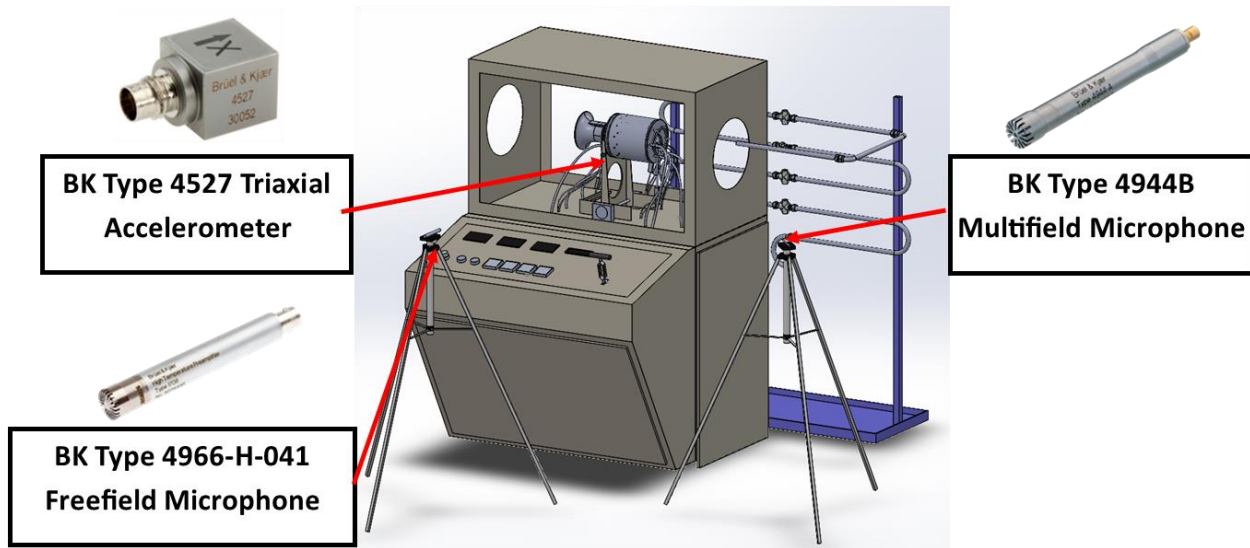


Figure 40: Noise and vibration data collection experimental setup.

4.3.3 Experimental Methodology and Data Processing

For this testing, the sound pressure, vibration, emissions, temperature, pressure, engine speed, and other engine characteristics were measured and collected at 3 different engine speeds: 60,000 rpm, 65,000 rpm, and 70,000 rpm for both Jet-A and F24. The experimental test setup as previously described and seen in Figure 72 was used to collect the data. Compressed air provided by Georgia Southern University was used to spool the compressor stage, thereby increasing pressure inside the combustion chamber. A rich fuel-air mixture ratio and a spark plug was used to fuel injector to encourage ignition. Once ignited, the engine idles at approximately 8,000-10,000 rpm. The engine speed was slowly increased to test speeds (the first being 60,000 rpm). After a stabilization period, data was recorded for a time period of 90 seconds. This time frame was determined based on the required data collection period of the MKS 2030 Multigas emissions analyzer. After the data was recorded, the engine speed was increased up to 70,000 rpm by increment of 5,000 rpm and the data recording process repeated. Once data was recorded at 70,000 rpm, the process was repeated by decreasing engine speed down to 60,000 rpm by increments of 5,000 rpm. Once data was collected 2 independent times at each of the 3 engine speeds. The turbine engine speed was slowly decreased down to 10,000 rpm and the engine power turned off.

All data for the engine characteristics (temperature, pressure, engine speed, fuel flow rate, and thrust) were processed through the NI USB-6218 Multifunction I/O DAQ and communicated with the MiniLab LabView software using the USB A-B cable. The software allowed for live monitoring and recording of all engine characteristics and data was recorded continuously throughout the test. This data was recorded into a text file that was copied and pasted into a master excel spreadsheet to perform post-processing. The emission data was monitored and recorded using the MG2000 software within the Multigas FTIR Spectrometer. This data was recorded for time periods of 90 seconds at each engine test speed to efficiently utilize the storage space of the data. This data was exported as an excel file and required little post-processing. Finally, the sound and vibration data were monitored and recorded using the BK Connect software. This data was also recorded in 90 second intervals at each engine test speed to reduce computational storage costs. Post processing of the data included the use of a constant percentage bandwidth filter for the sound pressure data, and a Fourier transform analysis to evaluate the vibration data, all of which was done in the BK Connect software. The frequency range used for the sound pressure and vibration data was 0-16 kHz and 0-25.6 kHz respectively. When post-processing the sound and vibration data, the harmonics were also examined and identified. The fundamental frequency for the turbine is represented by the shaft, which resonates at a frequency of approximate 1 kHz. The harmonics represented in this system include the 12 centrifugal compressor blades (oscillating at a frequency of approximately 12 kHz) and the 24 turbine stage blades (oscillating at a frequency of approximately 24 kHz). The combustion of the fuels can be categorized at a frequency of approximately 200-500 Hz.

CHAPTER 5

DATA AND RESULTS ANALYSIS

5.1 Fuel Characterization

5.1.1 Overview

The fuel characterization results can be found in the following sections. These results are used to provide transparency in the fuel and the properties used in the analysis of the engine performance. The fuel used in this experiment was Jet-A (POSF 10325) and F24 (POSF 13664). Each fuel was provided by the United States Air Force.

5.1.2 Viscosity and Density

As previously discussed, the viscosity and density of different fuels can play a significant role in the performance of the fuel in the engine. Temperature of the fuel also plays a role in the viscosity and density of the fuel. Therefore, these parameters were evaluated at a varying temperature range to determine the expected impact of the fuel on the engine. The viscosity testing was conducted in three trials and an average viscosity value was derived from the curve. A curve was generated out of a temperature range between 25°C and 90°C and can be seen below as Figure 41.

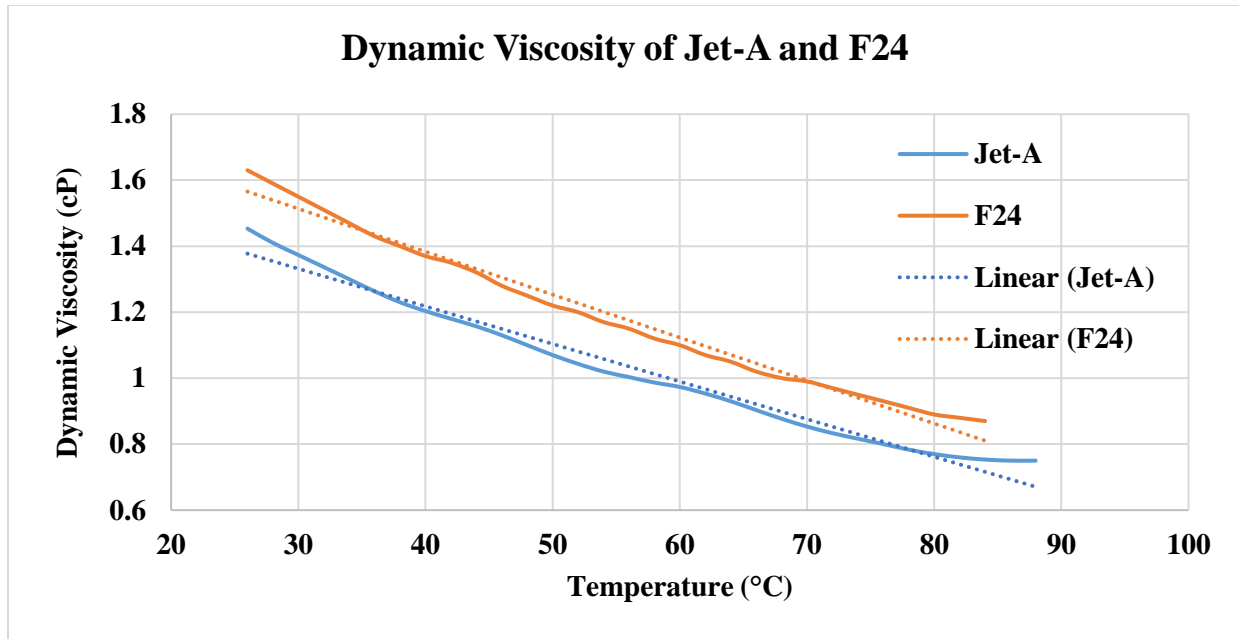


Figure 41: Dynamic Viscosity vs Time for Jet-A and F24

The kinematic viscosity, freeze point, and density was also examined using the JFA -70Xi. This device uses a similar process to determine kinematic viscosity, though the performance of 3 trials of viscosity measurements ranging from -40°C to 90°C. The viscosity value is taken 2 different temperature points and averaged across each 3 trials. The same process occurs for the density and freezing point. The result of the test can be found in the Table 6 below.

Table 6: Kinematic Viscosity and Density

Parameter	Jet-A	F24
Density@15°C (g/mL)	0.8033	0.8113
Freezing Point (°C)	-50.6	-46.8
Temperature @KV=12cSt (°C)	-46.0	-38.2
KV@-20°C (cSt)	4.421	5.805
KV@-40°C (cSt)	9.124	13.11

In comparing the fuel properties of Jet-A and F24, F24 clearly shows a higher density and viscosity. This difference in fuel characteristics should result in F24 having a larger SMD and droplet distribution, which will increase the amount of THC and CO emissions.

5.1.3 Spray Distribution

The results of the spray development testing provide the information to confirm the diagnosis of the viscosity and density conclusions. The droplet and spray testing were conducted by using 5 independent sprays and averaging the results to obtain the final spray and droplet data. The results from the testing can be found below as Figure 42 and Figure 43.

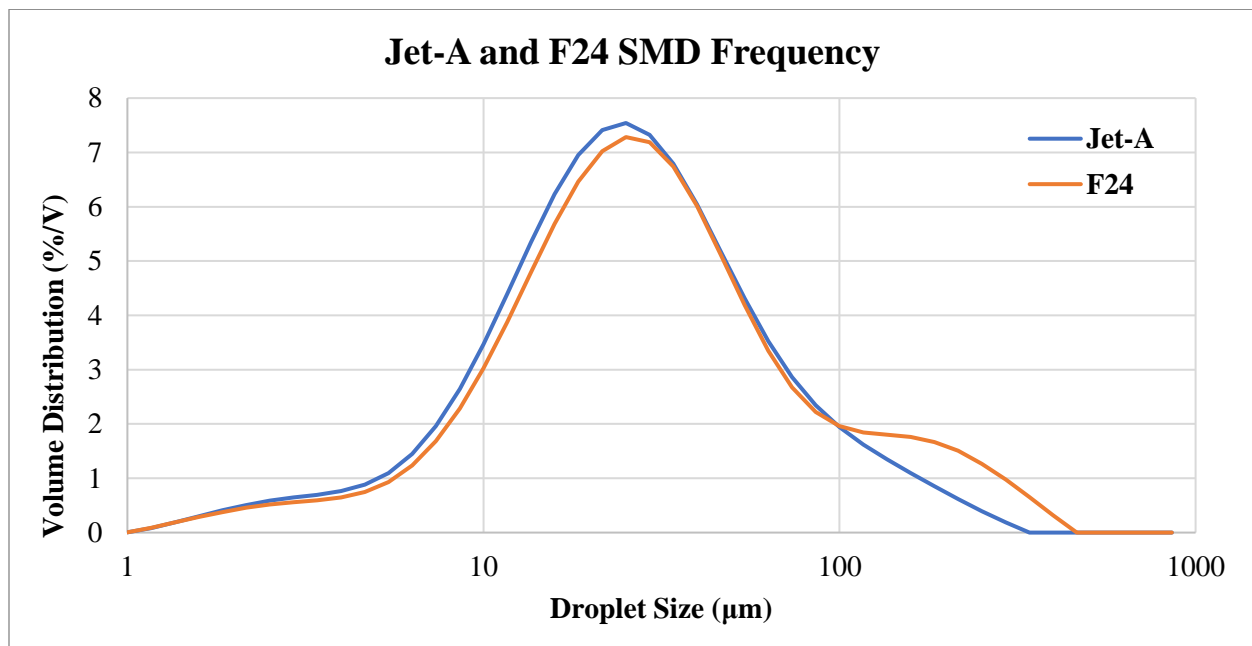


Figure 42: MIE Scattering Laser Droplet Volume Frequency for Jet-A and F24

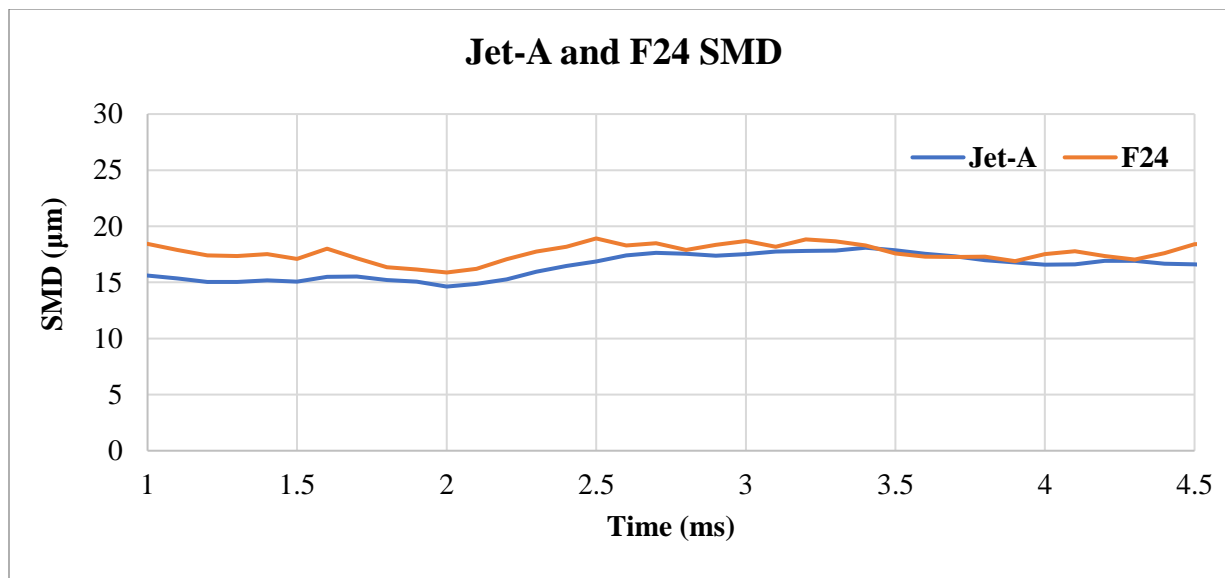


Figure 43: MIE Scattering Laser Sauter Mean Diameter for Jet-A and F24

The above figures show that Jet A and F24 (in blue and orange respectively) both show to follow a very similar profile in comparing the droplet and spray development. In Figure 42, it can be inferred that F24 has a slightly greater mean average droplet size based on a slight shift of the F24 curve to the right of the Jet A curve. This shift indicates that it can be expected that Jet A will result in more complete combustion, therefore reducing the emission of CO, THC (i.e. soot), and resulting in cooler temperature combustion. This would also result in the reduction of NO_x that would be produced. It would also be expected that Jet A would result in a higher performance of combustion efficiency as well. It can also be seen that F24 has a slightly narrower normal distribution, indicating a greater percentage of droplets from the spray are closer to the mean expected droplet size. However, the presence of such a slight difference may not result in a measurable difference in these parameters. The Sauter Mean Diameter curve in Figure 43 further confirms what was inferred in Figure 42. The SMD for Jet-A was found to be between 15μm and 22.5μm whereas the SMD for F24 can be found to be a much more consistent 22.5μm. The greater droplet size and frequency are most likely due to the greater viscosity of F24 as compared to Jet-A.

5.1.4 Low Temperature Heat Release via Thermogravimetric and Differential Temperature Analysis

As previously discussed, the low temperature heat release was investigated using thermogravimetric and differential temperature analysis (TGA and DTA respectively). This test was conducted to determine the volatility of the fuels. This directly translates the vaporization rate of the fuels and was measured by the mass percentage over the course of a 600°C test cycle. Jet-A and F24 testing was conducted 3 separate times, and the results were averaged to obtain the final data set seen below in Figure 44 and Figure 45.

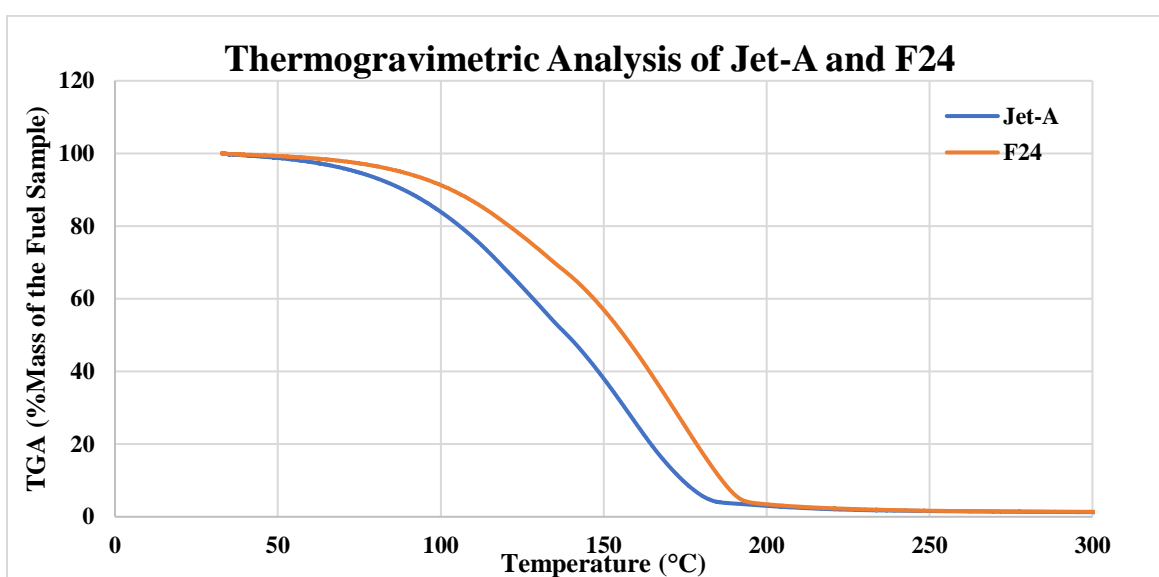


Figure 44: Thermogravimetric Analysis of Jet-A and F24

By examining Figure 44 above, it can be shown that Jet-A vaporizes at a higher rate than F24, indicating that Jet-A is a more volatile fuel. Moreover, both fuels are completely vaporized by the 200°C temperature point. This indicates that Jet-A should mix better with the air and should form a homogeneous mixture at higher rates than F24. It can be expected that the experimental testing with Jet-A will result in a more efficient combustion process. The average temperature and mass percentage of Jet-A and F24 can be seen below in Table 7.

Table 7: Average Temperature and Mass Percentage (TA%) of Jet-A and F24

TA (%)	Average Temperature (°C)	
	Jet-A	F24
TA (10)	88.585	103.22
TA (50)	138.81	156.16
TA (90)	172.24	186.32

The table above reveals the specific temperature and mass percentage over time for Jet-A and F24.

Again, based on this table, it can be inferred that F24 vaporized slightly slower than Jet-A.

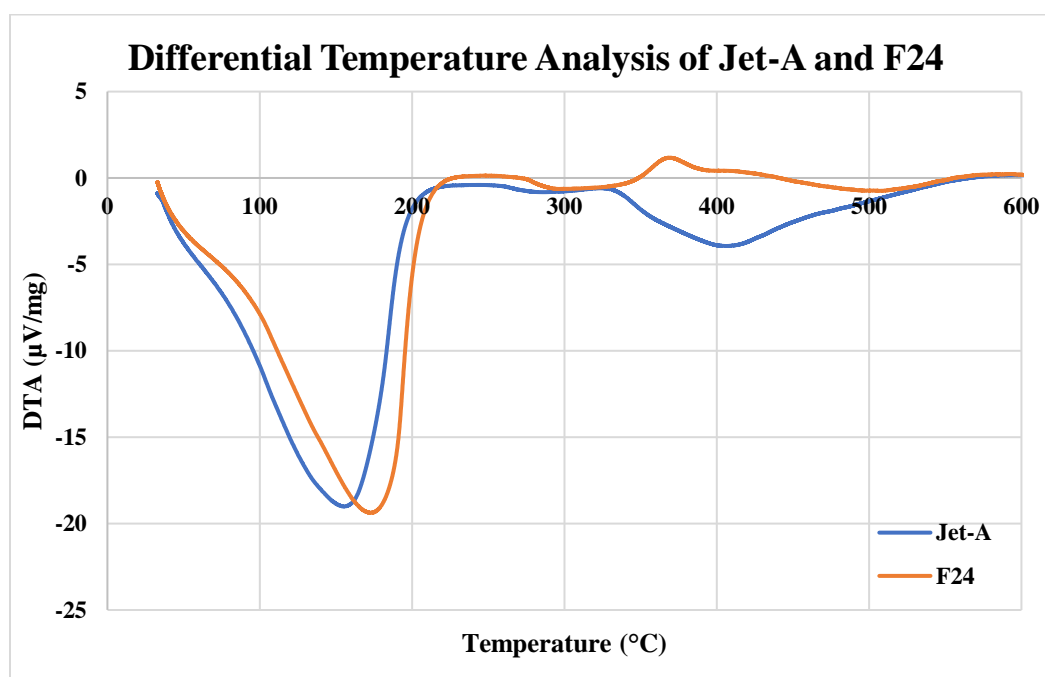


Figure 45: Differential Temperature Analysis of Jet-A and F24

By examining Figure 45 above, Jet-A and F24 follows the expected endothermic and exothermic reaction pattern. The fuel absorbs energy (indicated by the negative slope) from the increase in temperature in the environment and releases this energy in exothermic reaction. This occurs at 155°C for Jet-A, and at

172°C for F24. This indicates that most of the primary oxidation is occurring with the first 90% of the mass of the fuel, as revealed in Table 7. However, the remaining 10% of both fuels follow different subsequential pattern. Jet-A shows another endothermic reaction at 340°C followed by an exothermic reaction at 376°C. F24 on the other hand, shows an exothermic reaction at 340°C followed by an endothermic reaction at 409°C. Both fuels stabilize at approximately 551°C. These results indicate that Jet-A should provide a greater combustion efficiency and reduction in emissions.

5.1.5 Combustion Properties Analysis

The combustion analysis was conducted to better understand the ignition and combustion phenomenon present with Jet-A and F24. It also provides more information on the fuels reactivity and the energy corresponding to the combustion process. Figure 46 shows the average apparent heat release graphs for Jet-A and F24 over time. The apparent heat release rate results help to identify the amount of heat available to perform work. The beginning of the increase in AHRR shows the ignition delay, while the peaks in the AHRR graphs show the fuels with greater potential for work to be done based on thermal potential energy. This data was gathered from the CVCC using the data collection methods previously described.

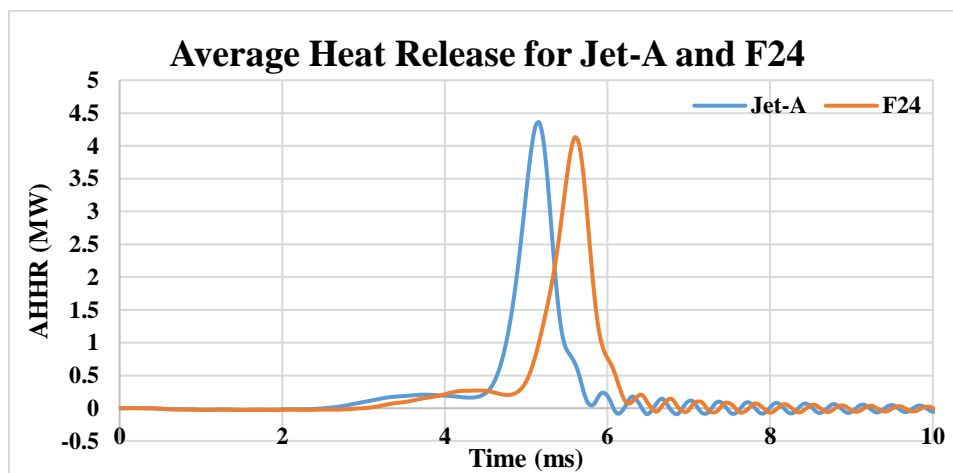


Figure 46: AHRR results for Jet-A and F24

Figure 46 clearly presents many valuable pieces of information about the combustion phenomenon differences between Jet-A and F24. First, Jet-A has an ignition delay of 3.26 ms, while F24 has an ignition delay of 4.09 ms. Secondly, Jet-A clearly has a greater slope than F24 leading up to the high temperature heat release (HTHR). Finally, Jet-A peaks at an AHRR value of 0.28 MW greater than the peak of F24. These results furthermore validate the previous tests that have shown Jet-A is more volatile, atomizes more efficiently, and undergoes a more reactive combustion than F24.

The combustion duration for Jet-A and F24 is 5.01 ms and 5.79 ms respectively. This 0.78 ms shorter combustion duration leads to F24 combusting over a longer period than Jet-A. Therefore, F24 has a flame front that requires a longer combustion duration to burn the entirety of the fuel. However, this slight delay in combustion also produces a smoother flame front, better combustion stability, and a reduction in overall ringing events that occur after combustion. A reduction in this ringing has also shown to reduce overall vibration inside the combustion chamber (Valentin Soloiu 2022, Soloiu et al. 2022), which also lead to more stable combustion. This reduction in overall ringing can be confirmed through examining Figure 47.

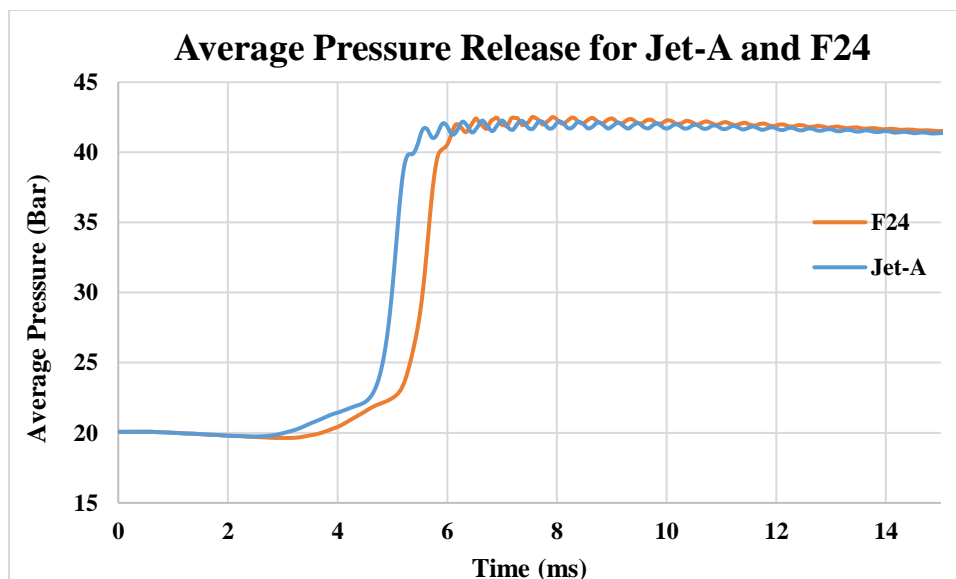


Figure 47: Average Pressure release for Jet-A and F24

Figure 47 provides more evidence for a slower combustion duration, but a reduction in the overall ringing in the system post-combustion. This, again, leads to an enhancement of combustion stability. Another notable data point is the nearly identical peak pressure in the CVCC during combustion of both fuels. This nearly identical peak pressure is a response to the nearly identical LHV value of Jet-A and F24, which can be seen below in Table 8

Table 8: Combustion Properties of Jet-A and F24

Fuel Property	Jet-A	F24
LHV (MJ/kg)	41.51	41.85
Ignition Delay (ms)	3.26	4.09
Combustion Delay (ms)	5.01	5.79
Derived Cetane Number	47.96	43.35

As seen above in Table 8, the Derived Cetane Number was calculated through the use of the ignition delay and combustion delay. These values were averaged from a series of 3 different trials. The DCN of Jet-A can be seen as 47.96, and the DCN of F24 can be seen as 43.35. Therefore, Jet-A is clearly a more reactive fuel and is unable to withstand higher pressure and temperature of a combustion chamber. F24 is therefore clearly more suited for higher performance engines, especially in the context of piston type or compression ignition engines.

5.2 Numerical Simulation Results and Analysis

5.2.1 Numerical Simulation Overview

The results discussed in this section include the numerical results from the simulation of Jet-A and F24. These results compare the results of different fuels at engine speeds of 60,000 RPM, 65,000 RPM, and

70,000 RPM. The simulation is not a perfect representation of the engine for a number of reasons that will be discussed, however, the percentage errors for each simulation is comparable enough to the experimental results to validate the models.

These results have been broken down into their own subcategories. These categories include numerically determined temperature, pressure, velocity, turbulent kinetic energy (TKE), a fuel spray analysis, and emissions contours.

5.2.2 Numerical Engine Temperature

As mentioned in previous sections, the plane of data collection for the numerical contours was oriented so that the axial progression of the fluid can be examined as well as the spray development of the fuel. As shown below in Figure 48.

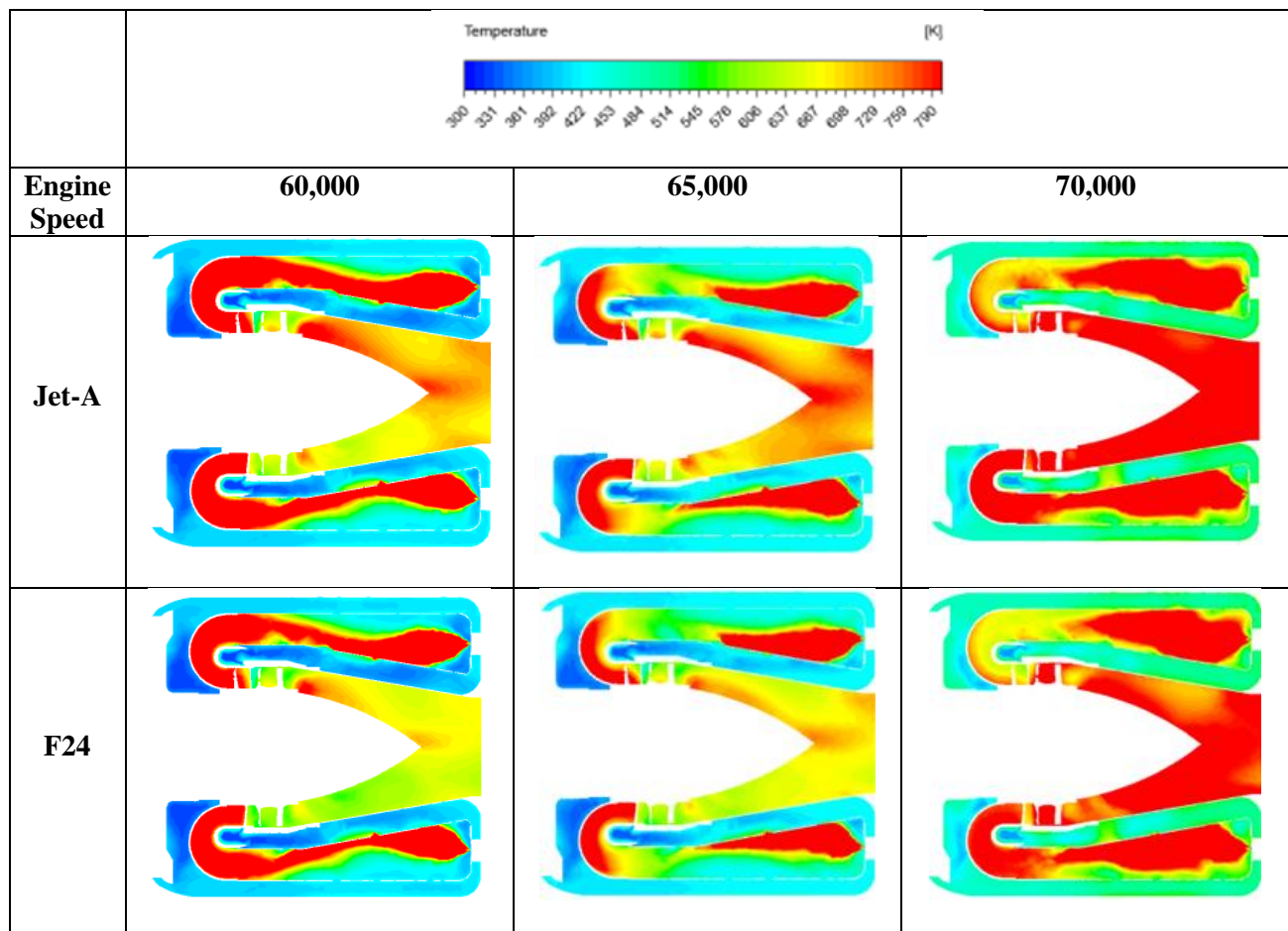


Figure 48: Temperature contours of Jet-A and F24 at each investigated engine speed.

The results first showcase the increase in temperature as the engine speed increases for both fuels. This increase in temperature is expected, and is also prevalent in the experimental results, indicating a correlation between the model and experimental results. Both fuels also experience a drop in the flame front as engine speed increases. This shrinking of the flame front can be explained by two phenomena. First is the enhancement of the mixing due to the guide vanes that are present. The higher compressor speed pulls in more air, resulting in more turbulence. This turbulence enhances mixing, resulting in a better fuel-air ratio and leading to more complete combustion. The second explanation is also a result of the higher engine speeds. Higher engine speeds will correlate to a greater swirl number experienced in the combustion chamber. This greater swirl number can be seen in the front view of Figure 49 below. Since the data was collected on a plane and the swirl number increases with engine speed, the larger flame front generated by greater mass flow rates of fuel is out of range of the data collection plane. This results in the appearance of a decrease in the flame front. However, the larger flame can be seen in the front and isometric view in Figure 49 below.

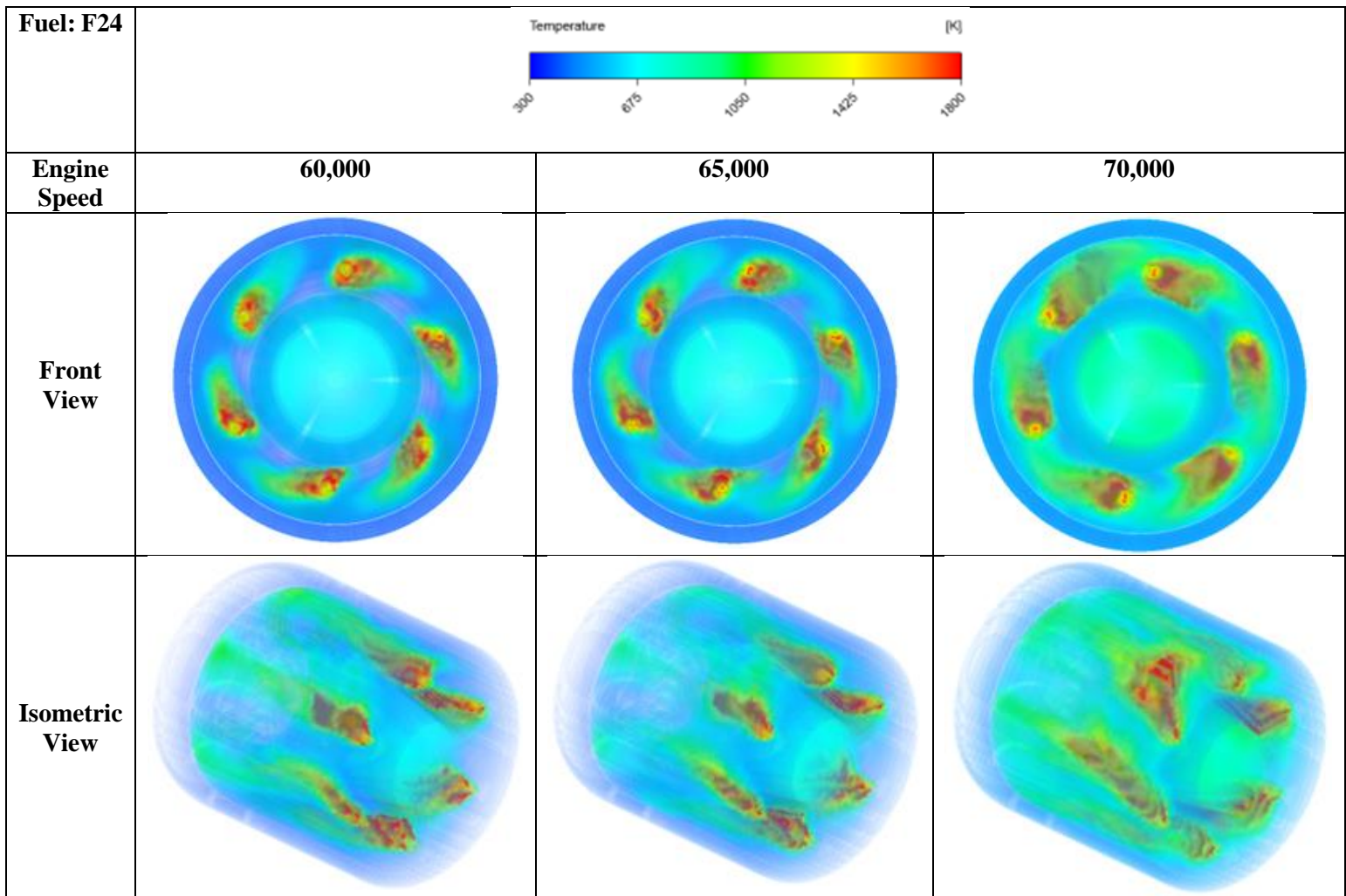


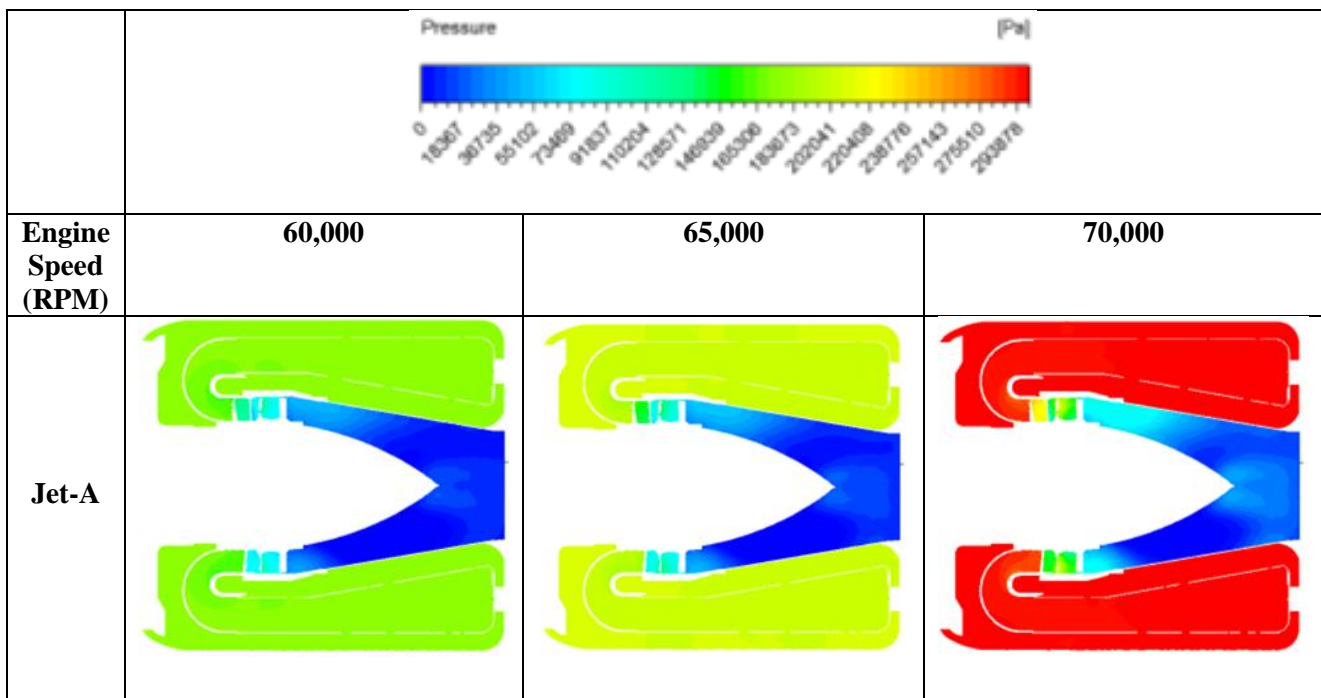
Figure 49: Isometric and Front view of the temperature contour for F24 at each engine speed.

Figure 49 also provides a clear picture of the flow path and demonstrates the enhancement of the swirl number as the engine speed increases. The front view clearly demonstrates the enhancement of the swirl flow in the engine as engine speed increases. Moreover, the front view also shows an increase in exhaust temperature from approximately 675K at 60,000 RPM to 1050K at 70,000 RPM. At this temperature, it is obvious there is not a flame in the exhaust section, since flame temperatures are generally in excess of 2000K. The isometric view shows the enhancement of the flame, clearly demonstrating a growth in flame thickness. This greater flame front and therefore higher temperatures is expected and correlates well with the experimental results.

Despite the similarity in the fuels, F24 appears to burn cooler than Jet-A. This was expected based on the additives used in F24 and based on the fuel analysis. The AHRR graphs showed less amplitude of the heat release in the combustion properties analysis. This has translated both qualitatively and quantitatively based on the temperature contours and the gas temperatures found in Table 10 in the Appendix.

5.2.3 Numerical Engine Pressure

The pressure contours for the numerical simulation of Jet-A and F24 can be found below in Figure 50. Due to the model of the simulation, P1 is assumed based on the experimental results. As found in Table 4 the pressure ratio for this engine as specified by the manufacturer is 3.4:1.



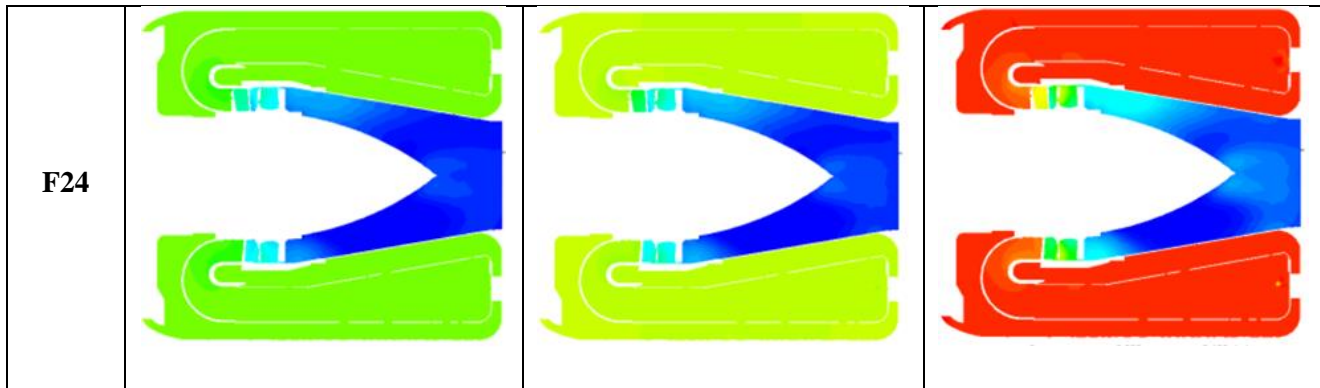


Figure 50: Pressure contours for the numerical simulation of Jet-A and F24

The pressure contours show similar results for both fuels. The high pressure from the ignition process generates areas of high pressure that are accelerating through the flow path of the engine and out the exhaust nozzle. As the flow passes through the turbine stage (also near the location of P4), the pressure drops dramatically. This is due to the expansion of the flow path, allowing the gas to expand and accelerate out of the exhaust section. Both fuels experience a localized high-pressure zone where the gas impacts with the turbine blades. Although a slight pressure increase would be expected due to impact with the turbine blades, this can also be explained due to the lack of rotation in the model. Furthermore, there is a slight increase in pressure at the tip of the exhaust nose cone. As engine speed increases, this zone of high-pressure increases. This can be explained by the impact of the flow against itself at the flow interaction zone.

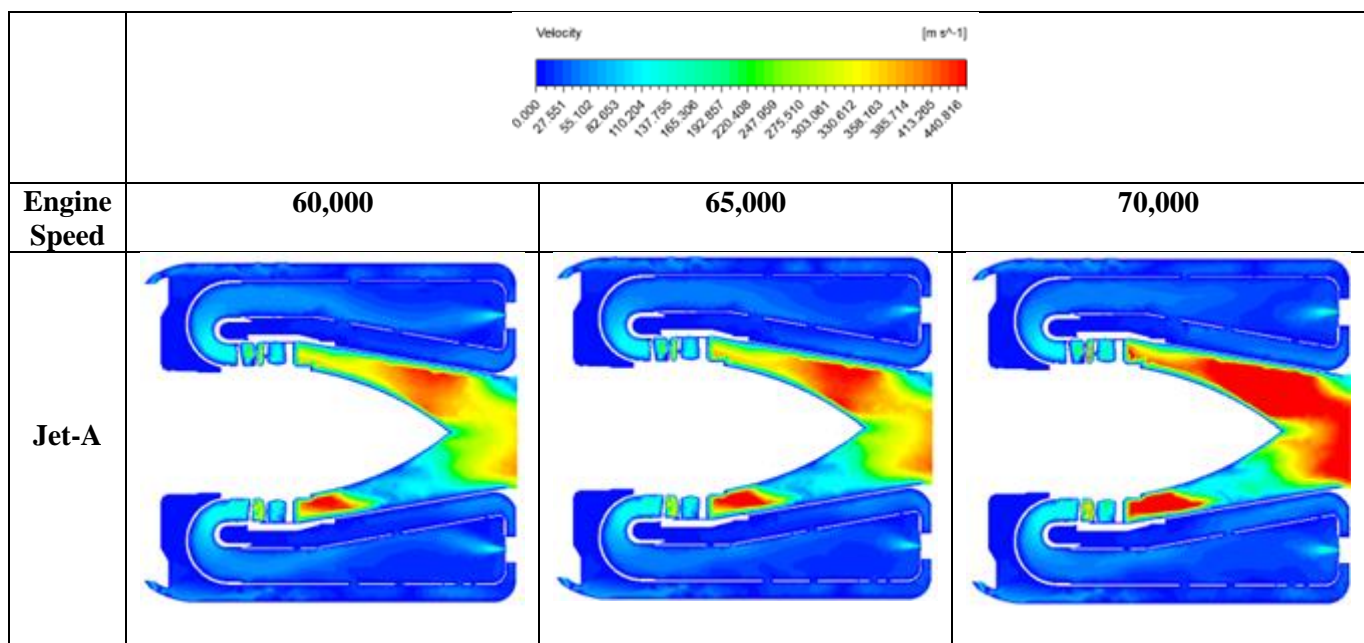
By examining the two fuels together, Jet-A displays a slightly increased pressure at 60,000 RPM. As the engine speed increases, both fuels have approximately the same pressure magnitudes at P3. Table 11 (located in the appendix) displays the experimental and numerical data for the pressure magnitude at each location. These results show a slight increase in pressure across P2 and P3. The maximum pressure for both fuels is located at P3, where at 70,000 RPM, both fuels are approximately 287 kPa. The trends for both fuels at P4 and P5 are very similar. Jet-A continues to output higher pressure magnitudes, and a pressure drop is present as the flow moves towards the exhaust section.

The drastically high pressure found in P2 and P3 is due to two major reasons. As previously discussed, the lack of rotation in the model allows for an increased local pressure near P3. The second

reason for the unexpectantly high pressure magnitudes is due to model assumptions. The model assumes a perfectly adiabatic and sealed model. Therefore, increases in temperature do not escape through the walls of the model, leading to increased pressure. Furthermore, the perfectly sealed model does not allow pressure loss through small gaps where the turbine is assembled. These factors contribute to the higher-than-expected pressure magnitudes in the model.

5.2.4 Numerical Engine Velocity

The velocity contours are valuable for obtaining maximum gas velocity of the turbine as a result of the different fuels used. The result of the numerical simulation can be found in Figure 51



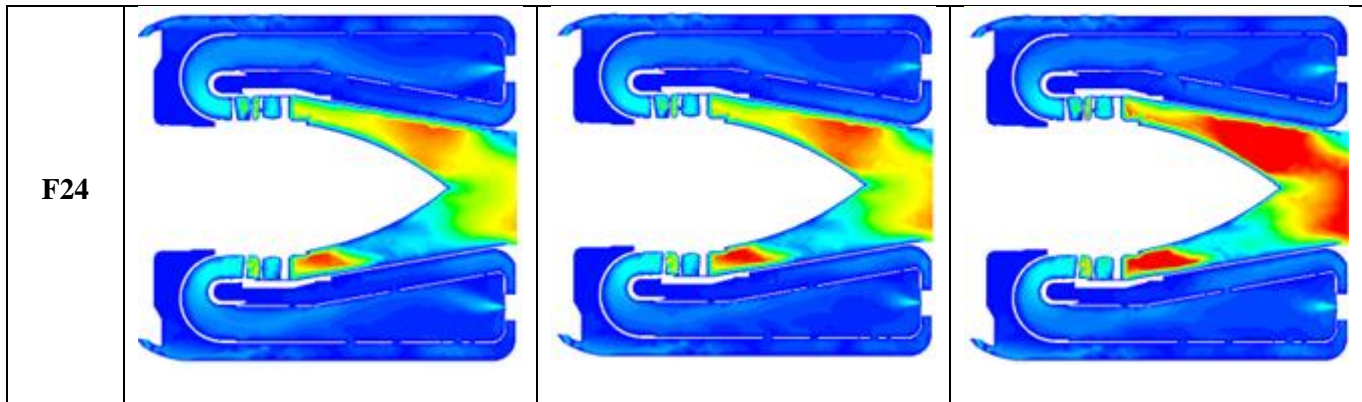


Figure 51: Velocity contours for the numerical simulation of Jet-A and F24

The velocity contours show overall trends that would be expected for a turbojet engine. The observation that can be made is the very small magnitude velocity located in the combustion chamber area (where P2 and P3 would be located). This low velocity flow is accelerated by the pressure wave generated from ignition through the turbine stage and out the exhaust sections. These velocity contours show good correlation with the pressure contours. The high-pressure zones are also the low velocity zones and vice versa. Furthermore, the contours also indicate that as the engine speed increases, the maximum velocity increases as well. This is obviously due to the increase in potential energy in the form of fuel input into the system. Both fuels also show an increase in velocity mid-way through the exhaust section. This increase in velocity is due to the vertical exhaust strut. The swirl of the flow due to the guide vanes and turbine section impinges the flow upon the struts and straightens the flow, increasing the velocity out the exhaust as well as increasing the thrust. The high velocity points located directly after the turbine section are due to the design of the flow path. The inlet guide vanes are designed to decrease the cross-sectional area, allowing for an increase in velocity.

By examining the two fuels together, it can be observed that both fuels exhibit very similar magnitudes of velocity. However, Jet-A demonstrates a slightly increased velocity in the flow exhaust section as measured by the yellow data collection points seen in Figure 29. The maximum velocity for Jet and F24 at 70,000 RPM was found to be and respectively. This can be seen in. This indicates that the thrust of Jet-A will be expected to be slightly greater than that of F24.

The rotation of the flow can be examined through Figure 52 below. Only the streamlines for F24 were provided due to the similarity in the flow path of both models. These streamlines make the swirl flow of the system very clear, as indicated by the groups of streamlines in the compressor exit sections. This swirl is enhanced in the turbine exit stage, where a much sharper increase in swirl can be seen. The work of the exhaust struts can also clearly be seen. As the flow is travelling through the exhaust nozzle, the flow is highly rotational. As the flow exits the exhaust nozzle, the streamlines are clearly oriented much more perpendicular to the exhaust nozzle than is exhibited in the turbine exit stage. This demonstrates the effect of the exhaust struts.

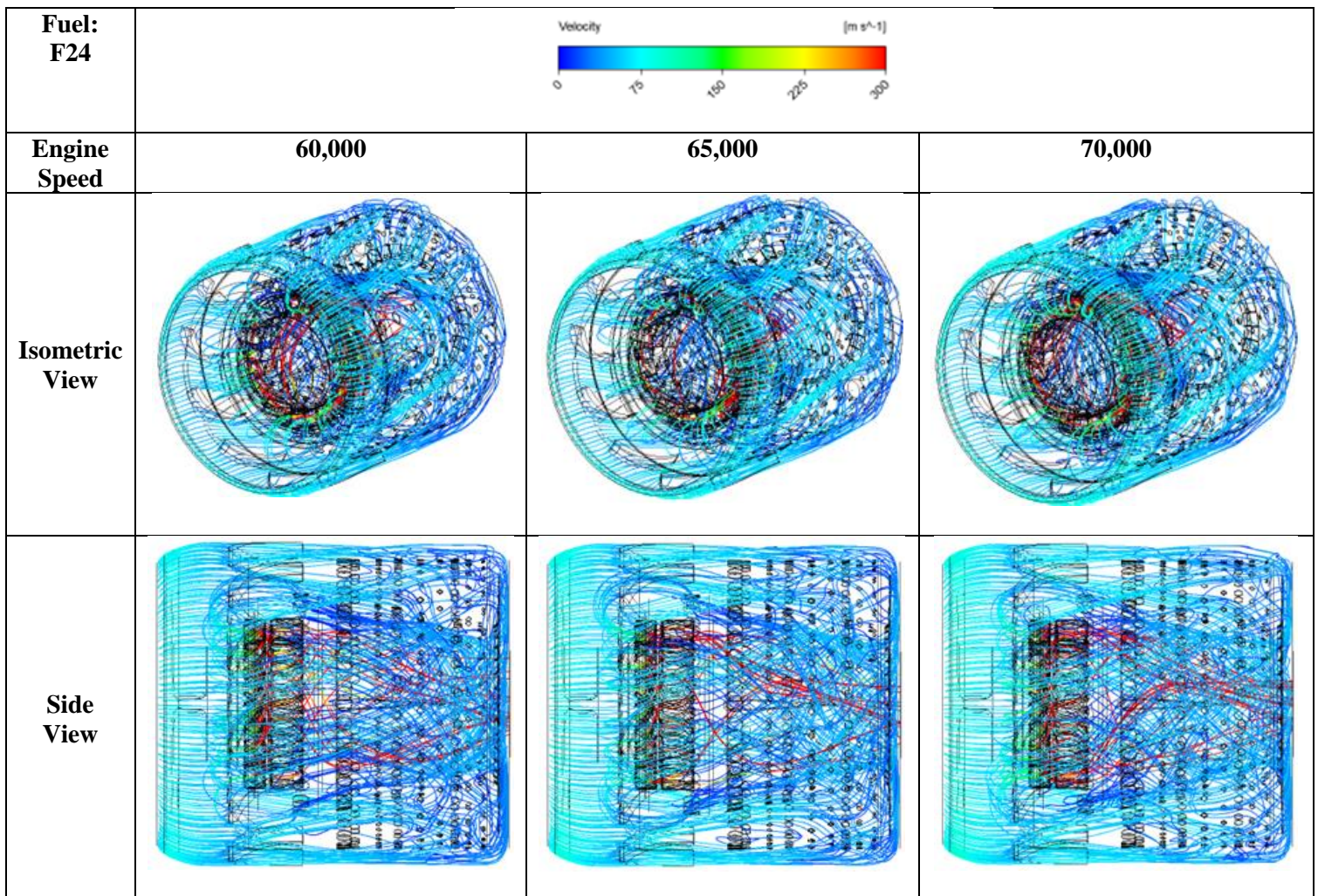


Figure 52: Velocity streamlines for the numerical simulation of F24.

5.2.6 Numerical Engine Turbulent Kinetic Energy (TKE)

The turbulence that occurs inside the combustion chamber can greatly affect the combustion efficiency and performance of an engine. High levels of turbulence inside an engine's flow path will reveal inefficiencies in the flow path design and requires steps to mitigate these effects. Therefore, the turbulent kinetic energy contours, as seen below in Figure 53 were generated and examined to identify areas of high turbulence intensity and their effect on engine performance.

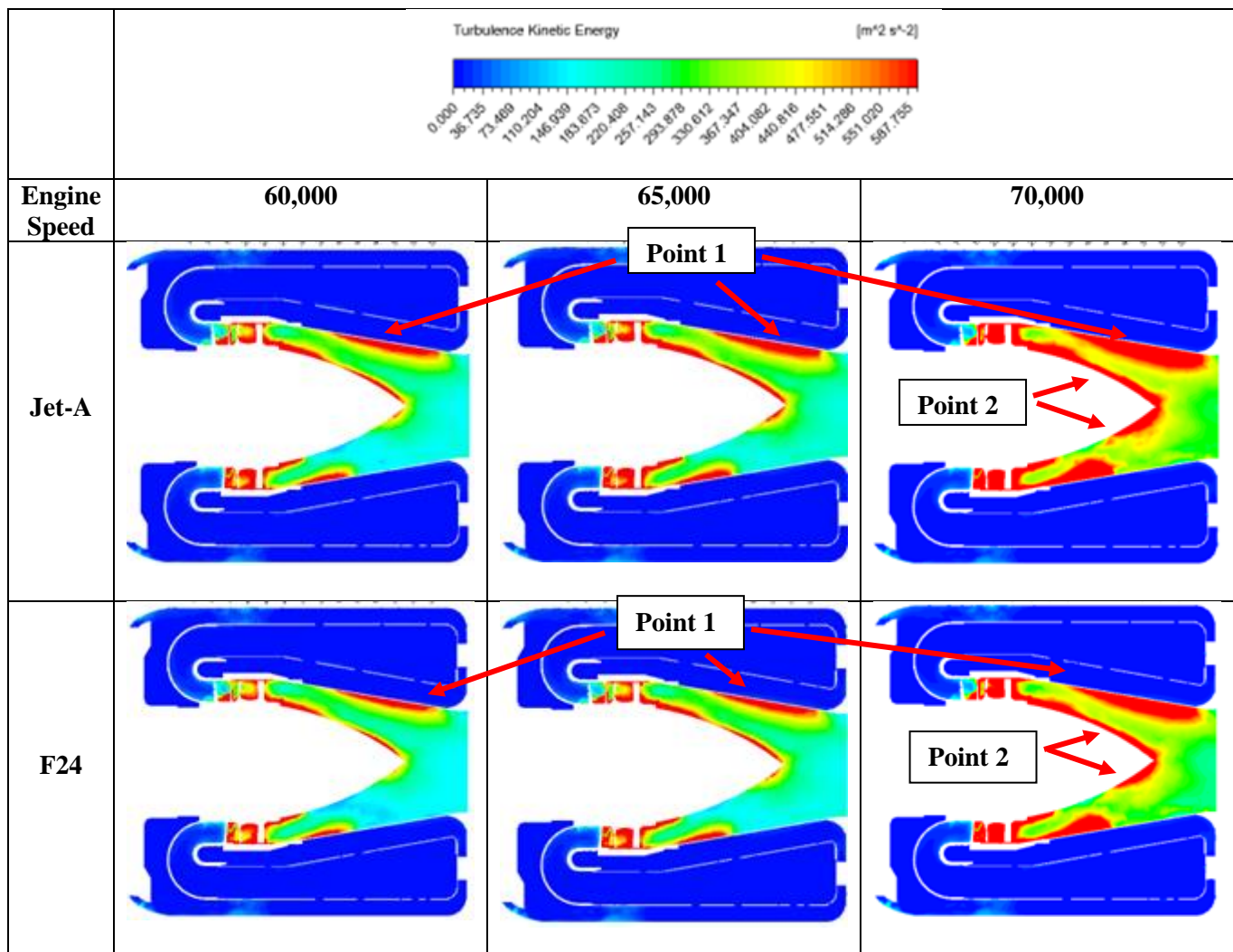


Figure 53: Turbulent kinetic energy for the numerical simulation of Jet-A and F24

First in examining the engine phenomenon that is consistent with both fuels, Figure 53 reveals an increase in the turbulent intensity as the engine speed increases. The areas of high localized turbulent

intensity include the turbine stage and the exhaust stage. As can be expected, the lack of rotation in the model from the turbine blades results in an unexpected flow disruption, which enhances turbulence in the system at this area. Furthermore, the increase in TKE with increases in engine speed is also examined at Point 1 on Figure 53. This increase in TKE is due to the exhaust strut flow impingement. As velocity increases, a greater amount of energy is transferred to the vortices, thereby increasing the TKE intensity. Another interesting phenomenon occurs at Point 2 on Figure 53 for both fuels. As shown, there is a high level of TKE following the path of the Exhaust cone. This high turbulence intensity can be expected to be due to the fluid/surface interaction. Due to factors like the surface roughness, a higher level of turbulence can be expected at these areas along the exhaust cone, especially in areas of high velocity flow. As demonstrated by the ANSYS simulation team, turbulent internal flow maintains a higher velocity near the walls of the enclosure (ANSYS 2020). These higher speeds allow for higher levels of turbulent intensity along the walls. The underside of the exhaust cone also exhibits a drastic decrease in TKE. This is expected to be due to the decrease in velocity, which occurs due to the low-pressure zone in the flow path as the flow impinges the exhaust struts.

When comparing the two fuels together, they both exhibit very similar behaviors. Both reveal an increase in turbulence intensity as engine speed increases. However, it can be seen that Jet-A does result in a higher level of turbulence intensity. Based on the TGA report, the higher volatility of Jet-A may result in higher levels of turbulence intensity throughout the engine. However, the difference between TKE of Jet-A and F24 are very small and may be negligible in comparing engine performance. More information is provided in the experimental noise and vibration results that demonstrate a better understanding of the two fuels turbulence intensities.

5.2.7 Numerical Engine Fuel Spray Analysis

The fuel spray analysis is an important feature of the engine analysis in order to examine changes in the spray as engine speed increases.

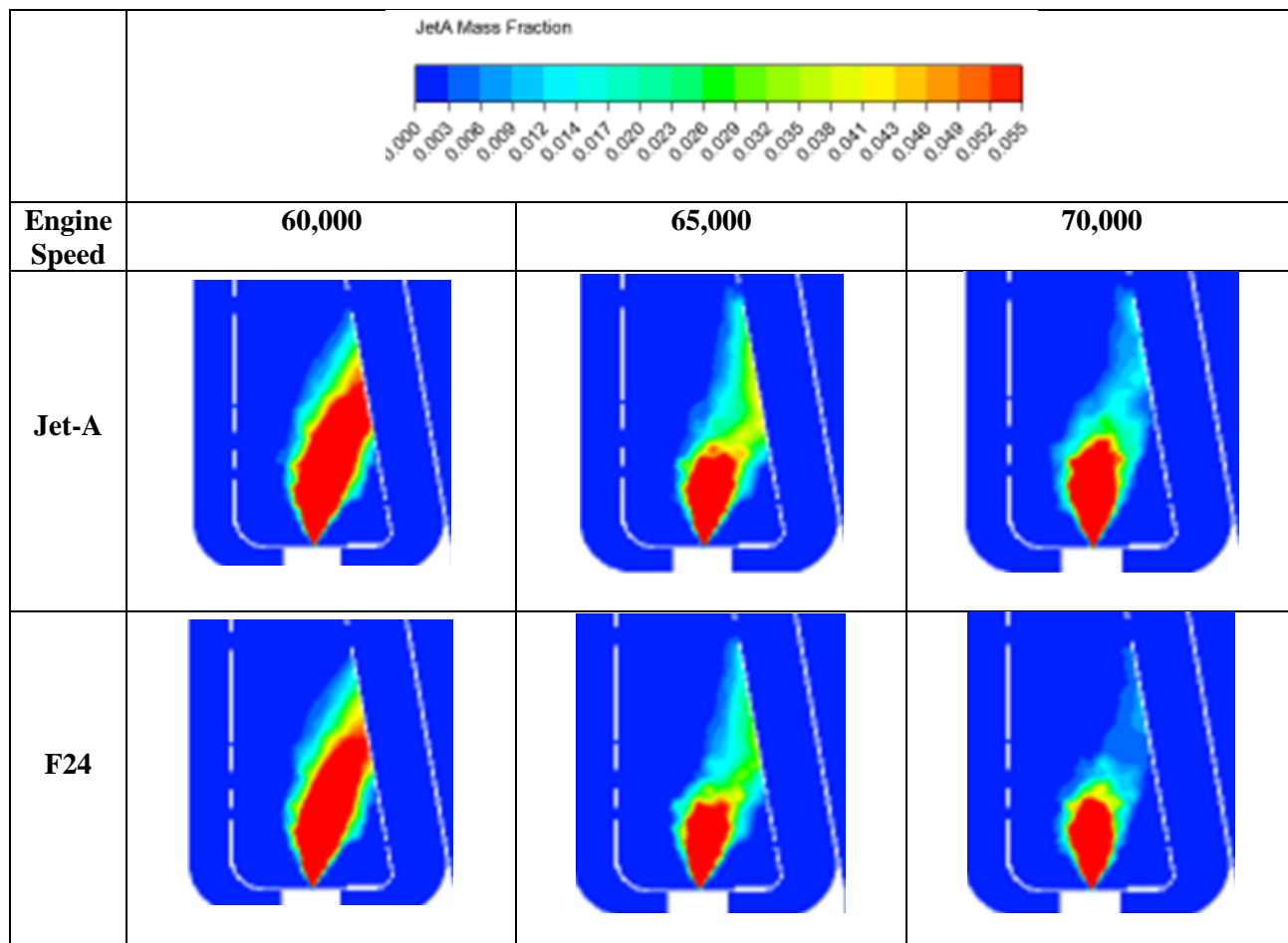


Figure 54: Fuel Spray Mass Fraction for the numerical simulation for Jet-A and F24

As shown above, the increase in engine speed appears to decrease the size of the fuel injection. This is due to the increase in the swirl number as the engine speed increases, taking a portion of the data for the mass fraction of the fuels from the plane of data collection. Between the two fuels, F24 appears to diffuse slightly better than Jet-A. This can be noticed at the 65,000 RPM engine speed, where there is more mass fraction of Jet-A than F24. This seems to indicate that F24 is more conducive to the flow path than Jet-A.

5.2.8 Numerical Engine Emissions

The emissions data was collected for CO, CO₂, H₂O, and NO_x, and planar contours were generated to display the creation of these emissions throughout the flow path of the gases. The purpose of this data is to better understand the creation of these emissions and how these affect the combustion efficiency of the

engine. As previously discussed, the impact of greenhouse gases like H_2O and CO_2 have a significant effect in global warming. H_2O is especially interesting case, due to its ability to trap soot and in the atmosphere and create the reflective crystals that contribute to the greenhouse effect. Therefore, H_2O is a vital emission to study when decreasing the aerospace footprint on harmful emissions. The H_2O mass fraction contours can be found in Figure 55 below.

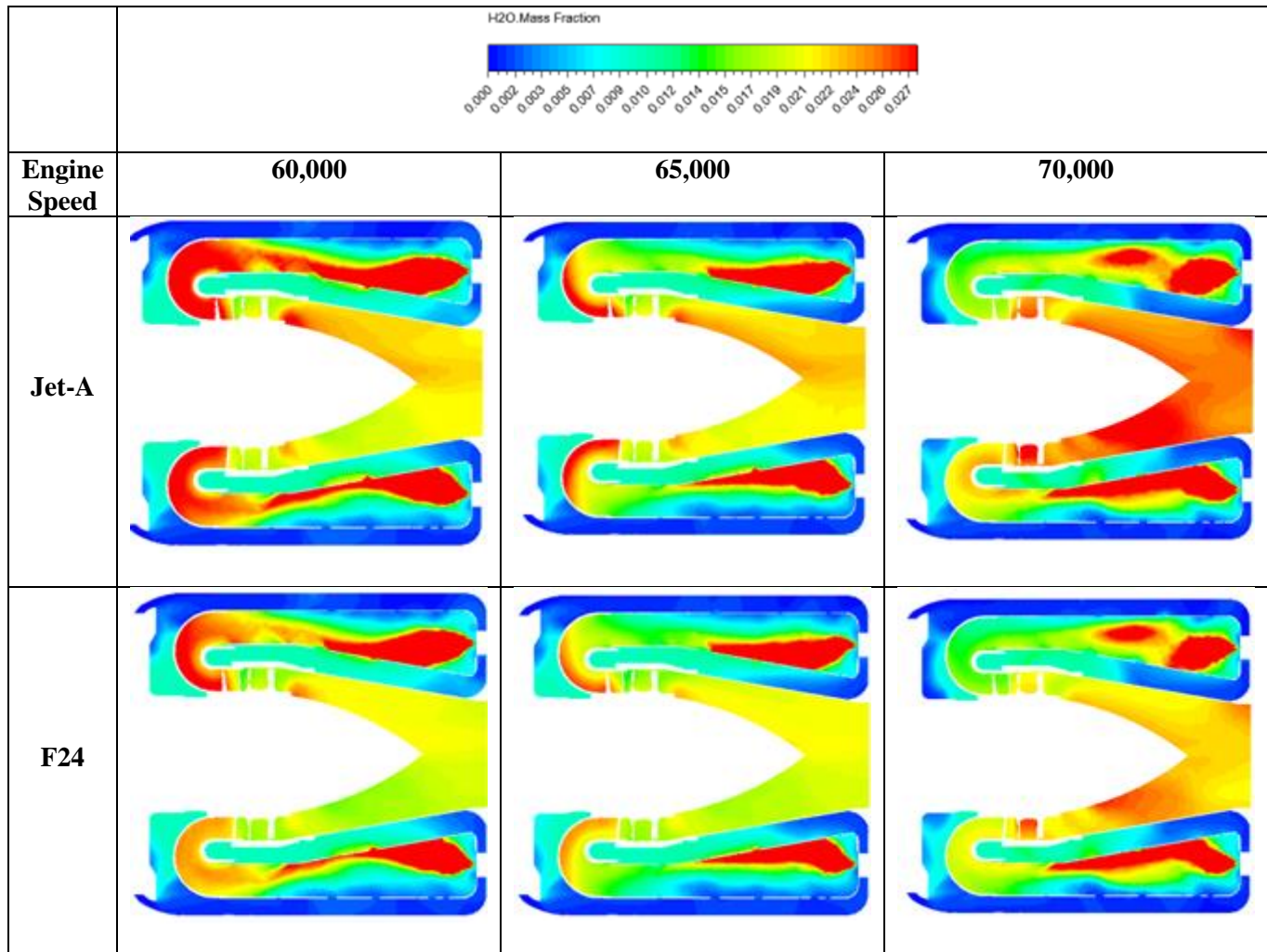


Figure 55: Water Vapor emissions from the numerical simulation of Jet-A and F24

By examining the contours above, it can be seen that as engine speed increases, there is also an increase in the water vapor emissions produced. Water vapor (as well as CO_2) is a natural by-product of complete combustion. Therefore, it is expected to see increases in H_2O with increases in engine. This is due to both the enhancement of complete combustion at higher, more efficient engine speeds, and due to the

injection of more fuel to achieve greater engine speeds. It can also be noticed that most of the products form in the combustion chamber. As the flow progresses through the engine, these gaseous emissions fill the exhaust nozzle and exit the engine. Finally, both fuels display as similar contours in the combustion chamber, indicating the location of H₂O formation is consistent between the two fuels.

When examining the two fuels separately, it can be inferred that Jet-A is producing a greater amount of H₂O emissions at each engine speed. There are multiple reasons for this decrease in emissions for F24. First is due to the additive package that is used in the creation of F24. This addition to the fuels has had significant effects on the emissions produced in burning F24. More specifically, F24 has a greater amount of olefins and cyclohexane's (Valentin Soloiu 2022). Greater amounts of olefins and cyclohexane's has been linked to reducing ignition and increasing combustion delays, and lead to an increase in the NTC region (Rao 2023, Yitao et al. 2009). Finally, increasing the NTC region and extending the LTHR region allows for extension of cool flame formation, which is a period of energy exertion that increases engine performance and decreases hydrocarbon emissions (Harsh and Sanghoon 2019, Soloiu et al. 2017, Yaopeng et al. 2016, Guzman and Brezinsky 2021, Bishop and Elvers 2021). Therefore, the reduction in water vapor formation for F24 is expected.

Since H₂O and CO₂ are both by-products of complete combustion, it would be expected to see a similar trend with H₂O and CO₂. Figure 56 below presents the CO₂ contour results for both fuels at increasing engine speeds.

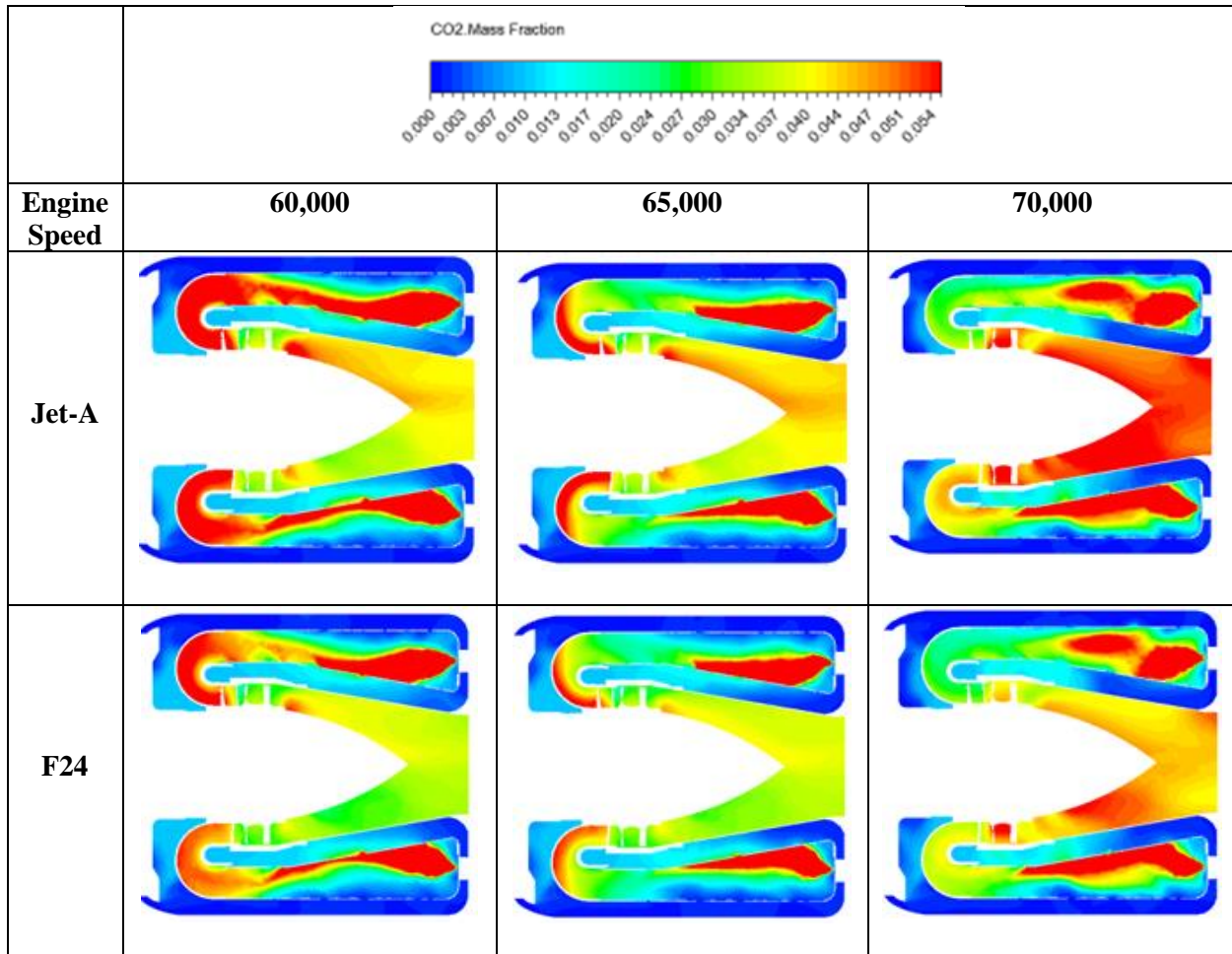


Figure 56: Carbon Dioxide emissions from the numerical simulation of Jet-A and F24

These results indicate a similar contour as that which was seen for the H₂O emissions. As engine speed increases, the CO₂ mass fraction for both fuels also increase. Again, this is due to the increase of complete combustion and the increase of mass fraction of the fuel being injected into the system. For similar reasons, it can also be observed that the combustion of F24 results in less CO₂ emissions. The consistency between CO₂ and H₂O provides validation that the combustion model is performing as expected. These qualitative results will be compared to the quantitative results found in the experimental results section.

Another important emission generated in the combustion of hydrocarbon fuels is carbon monoxide (CO). Carbon monoxide is generated primarily during incomplete combustion. When the air-fuel ratio (AFR) for the engine is not at the stoichiometric level, the breakdown of hydrocarbons leaves some remaining carbon that combines with the oxygen and forms CO. This is a poisonous emission that has a

serous negative effect on the well-being of humans. By examining the CO contours in Figure 57 below, the CO production phenomenon can be determined.

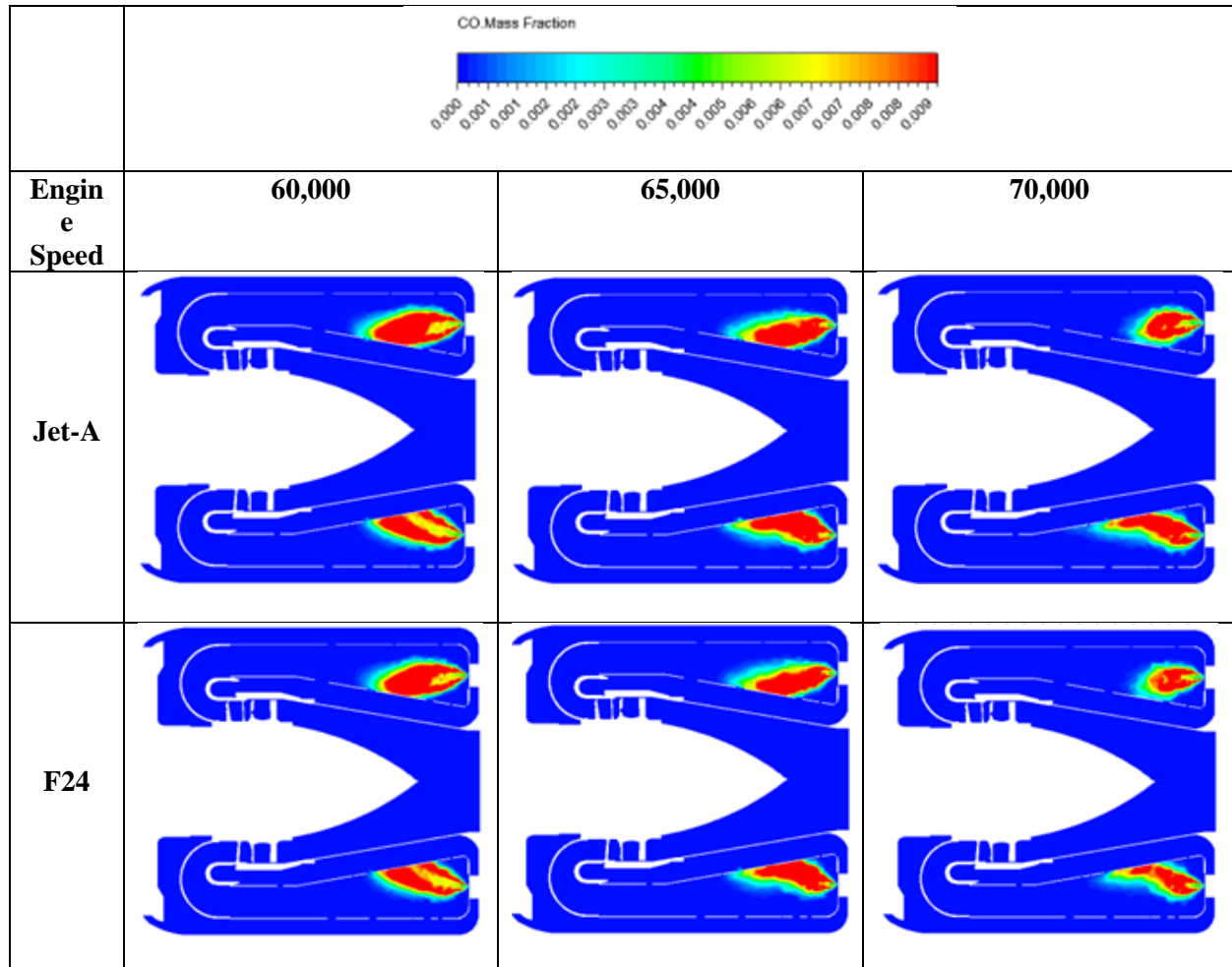


Figure 57: Carbon Monoxide emissions from the numerical simulation of Jet-A and J24

For both fuels, the results indicate that as engine speed increases, there is a reduction in CO production. This demonstrates the decrease of incomplete combustion and further explains the increase of complete combustion as inferred from Figure 55 and Figure 56. Due to the similarity of the fuels, there is not a significant difference between the contours.

Finally, the nitrogen oxides were also examined in the numerical simulation. Nitrogen oxides (NO_x) are the poisonous emission that form when oxygen and nitrogen experience environments of high temperature and high pressure. They typically form in environmental temperatures at or above 1700K,

making a combustion chamber an ideal location for the formation of NO_x. The results for both fuels can be found in Figure 58 below.

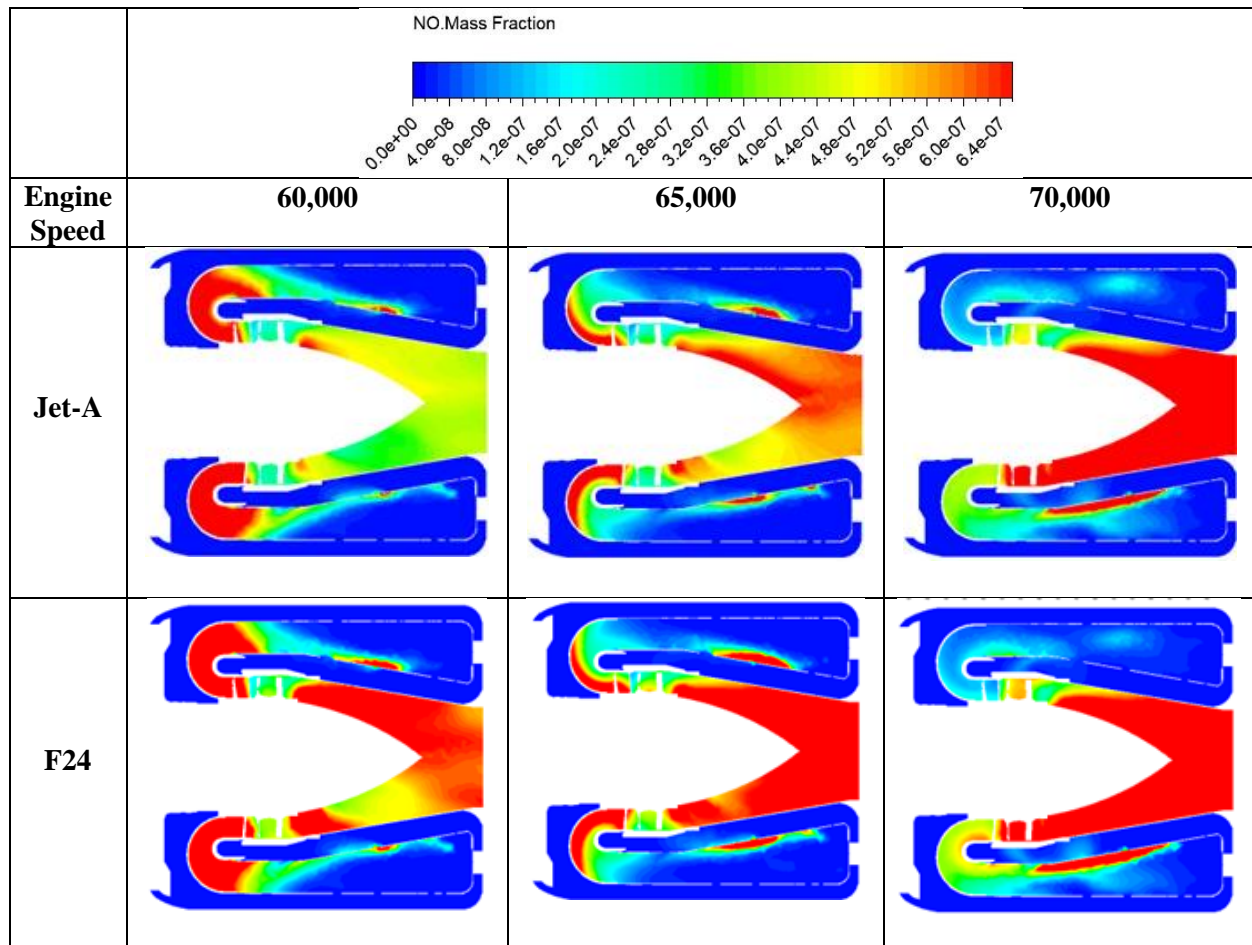


Figure 58: Nitrogen Oxides emissions from the numerical simulation of Jet-A and F24

The results from the NO_x emissions show an increase in NO_x for both fuels as engine speed increases. This is an expected result, with the NO_x contours following the linear trend of the temperature contours as engine speed increases. When comparing the two fuels. It is obvious that F24 shows a much greater mass fraction of NO_x. This is in direct contrast with the temperature contours, which indicate that Jet-A results in higher temperatures inside the combustion chamber and throughout the exhaust section. The best rationalization for this is the additive package in F24. Even though F24 experiences a lower temperature profile than Jet-A, the maximum temperature inside the engine is still greater than the required 1700K for NO_x formation. As previously mentioned, F24 contains greater numbers of cyclohexane than

Jet-A. As discussed in the study conducted by Rao et al. a greater abundance of cyclohexane in a fuel can result in a greater production of OH radicals (Rao 2023). This extra exertion of oxygen into the system could result a greater formation rate of NO_x in the system. Furthermore, when examining the O_2 contours, as shown below in Figure 59, there is more oxygen present the F24 simulation than is present in the Jet-A simulation. There is a particularly high presence of oxygen in the exhaust region, which is similarly where the most NO_x are formed. Therefore, it can be concluded that this greater presence of oxygen in the system is allows for a greater formation rate of NO_x in the F24 simulation as compared to Jet-A.

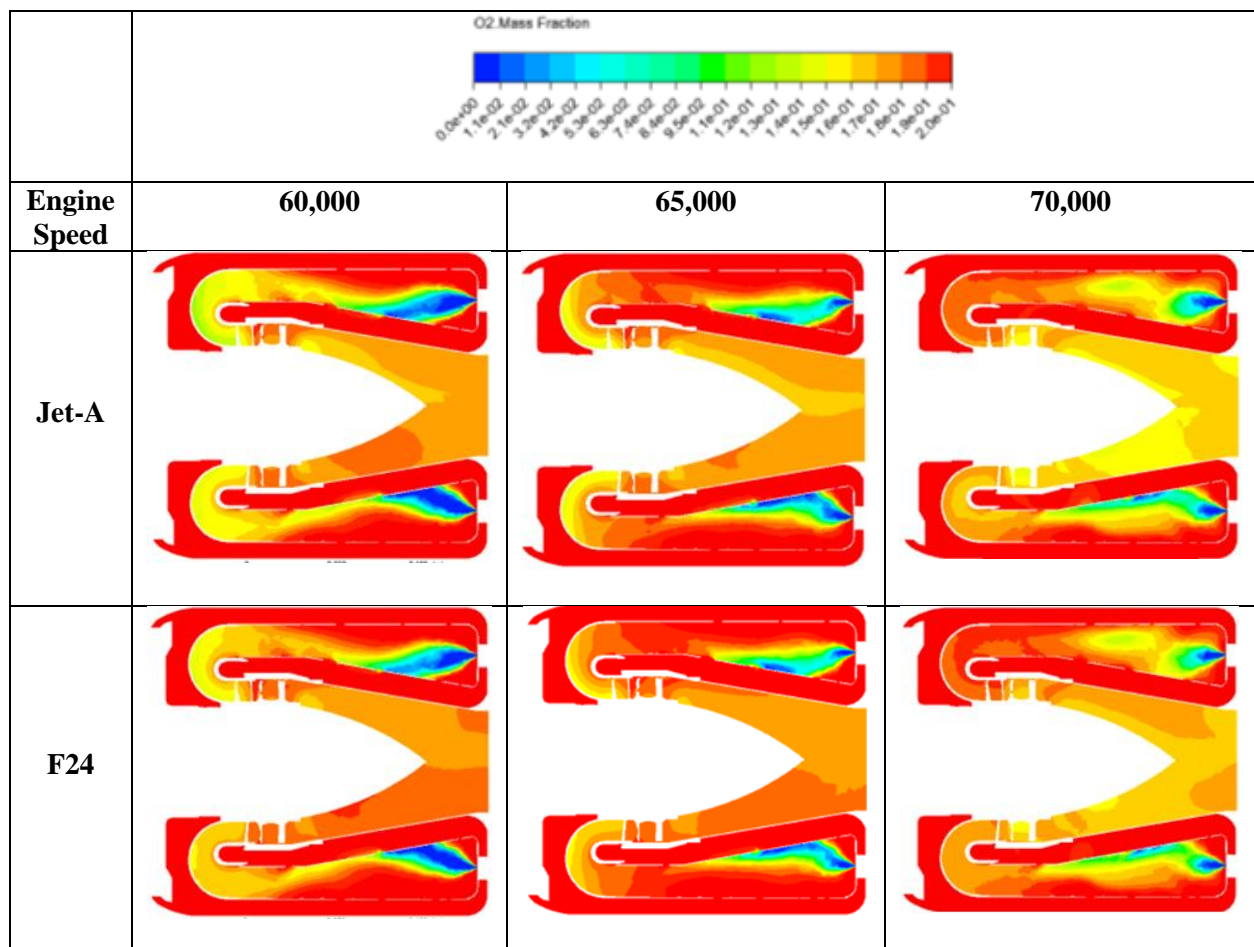


Figure 59: Oxygen mass fraction results from the numerical simulation of Jet-A and F24

5.3 Gas Turbine Experimentation Results

5.3.1 Experimental Engine Overview

The results discussed in this section include the experimental results from the testing conducted for Jet-A and F24. These tests were conducted at 60,000 RPM, 65,000 RPM, and 70,000 RPM. Each test was conducted on days with reasonably similar atmospheric conditions, including humidity and temperature levels, to ensure accuracy in the results. The various transducers used to collect data were zeroed and within a reasonable calibration range based on previous results. The experimental methods mentioned previously were conducted during both testing instances to ensure accuracy in the results.

The data collected during the experimentation include engine characteristics, emissions data, and finally a noise and vibration analysis. Each parameter has been sectioned into appropriate sub-sections for readability. The engine characteristic sections include temperature, pressure, thrust, fuel flow rate, thermodynamic efficiency, air-fuel ratio (AFR), and thrust specific fuel consumption (TSFC). The emissions sections include average H₂O percentage, average CO₂ percentage, average CO, average NO_x, and average THC. Finally, the noise and vibration analysis are sub sectioned into vibrations, multifield sound pressure, and free field sound pressure.

5.3.2 Engine Temperature

The engine temperature data was collected for both the numerical simulation and experimental results and compared for both fuels at all 3 engine speeds. This data is shown below in Figure 60.

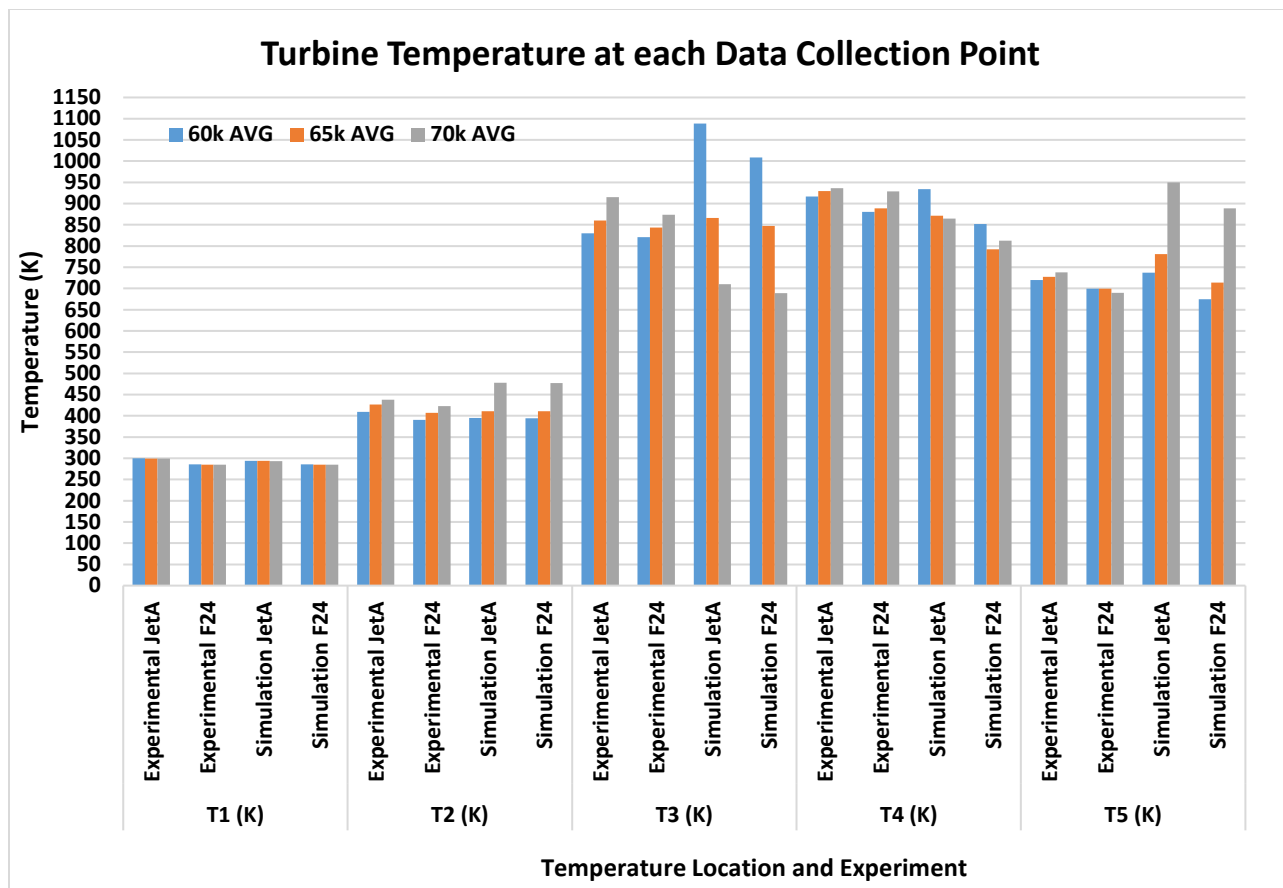


Figure 60: Turbine Temperature at each data collection point in the engine for both experimental and numerical simulation at each engine speed.

As shown above, the data is categorized by the data collection point within the engine, grouping both experimental and numerical results for both fuels in each engine speed range. As mentioned in the methods, the inlet temperature (T1) was not simulated, and therefore is the same as the experimental.

As seen above, the typical trends for the temperature inside the engine apply to the experiments conducted here. As the flow moves from the compressor to the turbine exit, there is a steady increase in temperature, with a maximum recorded temperature at 70,000 RPM of 935K for Jet-A and a maximum temperature of 928 for F24. After the turbine exit, the flow loses energy and begins to slightly cool as the gases move from the combustion chamber to the exhaust section, resulting in a maximum exhaust temperature at 70,000 RPM of 737K for Jet-A and 689K for F24. As engine speed increases, there is a

noticeable increase in the temperatures experienced inside the engine at all sensor locations. This is due to the obvious increase in potential energy in the form of more fuel being injected into the combustion chamber.

When comparing the two fuels, one main difference is the maximum temperature achieved by both fuels. F24 consistently burns cooler at all sensor locations for all engine speeds. This is most likely due to the addition of additives in the fuel. The change to a cooler burning fuel allows for the engine to have an overall increase in life expectancy and requires less maintenance between takeoffs. It also will affect the emissions produced, where it can be expected that F24 will see a reduction in NOx production.

Moreover, comparing the simulation provides a very compelling case for the accuracy of the model produced in this experimentation. The result in T2 provides good accuracy with a maximum percentage error occurring at 70,000 RPM of 9.04% for Jet-A and 12.75% for F24. This accuracy is due to the temperature change in this location being solely due to compression of the air. T3 results in a wider range of results. At the extremes of the engine speed, a greater difference is present, with the maximum percentage error being for Jet-A and 70,000 RPM of 31%. However, for the 65,000 RPM, the percentage differences were much smaller, in the range of less than 1%. This trend is continuous throughout all sensor locations, indicating that 65,000 RPM simulation is the most accurate. The simulation also has a counter-intuitive trend in some locations, where an increase in engine speed results in a decrease in temperature. This may be due to the swirl effect produced by the engine. Since the run time of the simulation was fairly small, the actual temperature in this zone does not have time to equalize throughout the chamber. However, the experimental results are an average of 90 seconds of data collected at 1S/s, allowing for a better average temperature to be obtained. Furthermore, most of the data collected indicates that increasing engine speed results in increases in temperature.

At T4, there is good agreement between simulation and experimental results for each engine speed, with 70,000RPM producing a greater difference of 12.5% for F24 and 7.61% for Jet-A. The same overall trend still exists in the simulation with a decreasing temperature due to the swirl effect and short time of

simulation run. Finally, T5 shows good results at low engine speeds with a maximum temperature difference being 7.35% for Jet-A. However, 70,000 RPM produces greater percentage differences up to 28% for both Jet-A and F24. The trends of decreasing temperature with increasing engine speed changes in this sensor location, producing more accurate trends results. This is because at this point in the engine, the flow has straightened significantly, resulting in swirl flow not affecting the overall temperature in a significant way.

The greatest percentage differences appeared consistently at 70,000 RPM. This can be assumed to be due to the enhanced swirl number inside the engine at the greater engine speeds. The greatest difference in the setup between each engine speed was compressor mass flow rate and fuel flow rate. Because of the increase in swirl number and fuel and air flow rate into the engine, it is expected that when the swirl number is taken out of the equation, the temperature should be greater. This is the effect that can be seen with the higher temperatures in T4.

5.3.3 Engine Pressure

The engine pressure data was collected for both the numerical simulation and experimental results and compared for both fuels at all 3 engine speeds. This data is shown below in Figure 61.

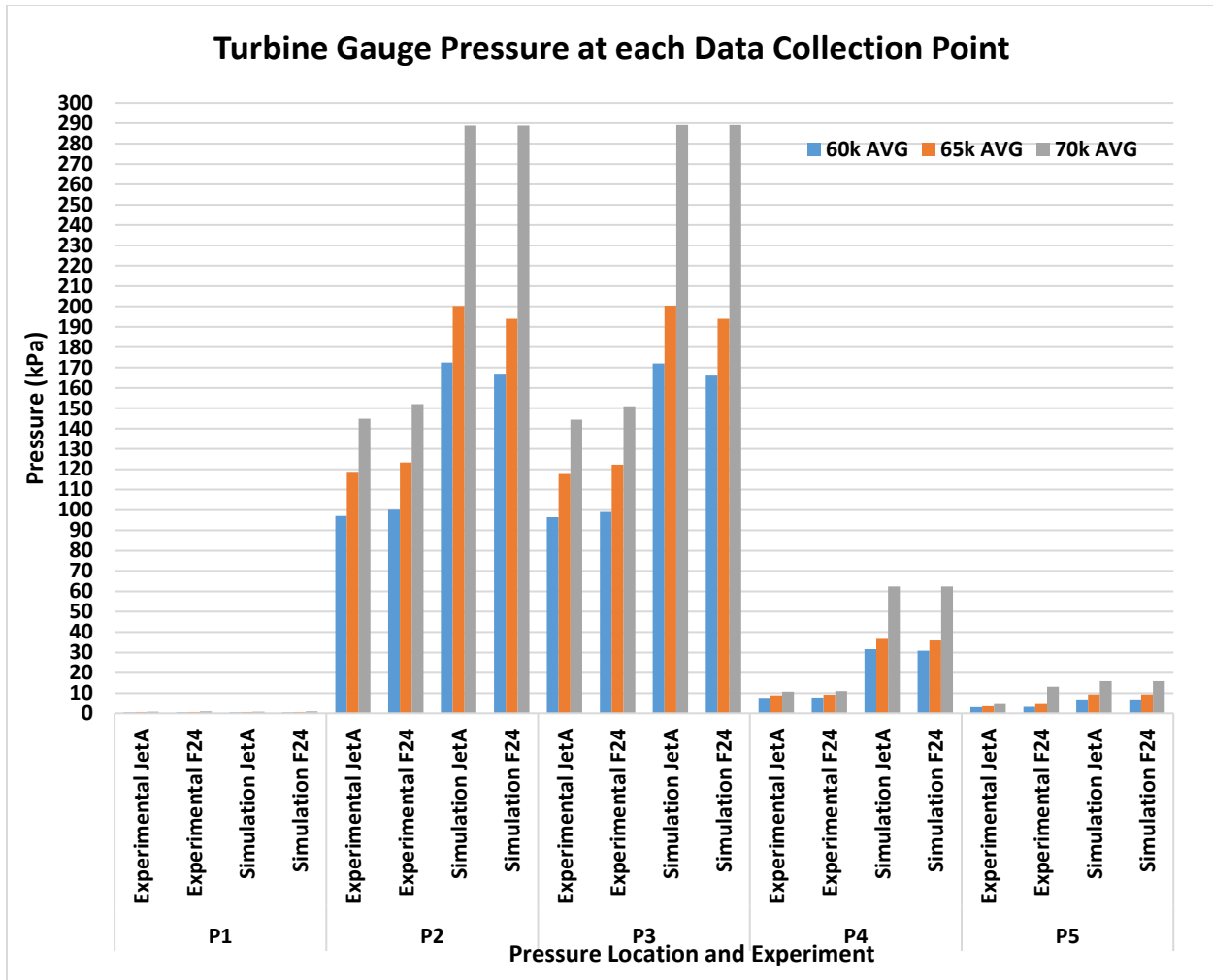


Figure 61: Turbine Pressure at each data collection point in the engine for both experimental and numerical simulation at each engine speed.

When examining the overall trends of the engine, both the simulation and experimental results show good correlation with change in pressure, although the magnitudes differ. Pressure increases from P1 and P2 due to the work from the compressor. At P3, both experimental and simulated pressures remain constant. Finally, as the flow moves out of the engine, there is a significant drop in pressure from P3 to P4 and P5 until the flow reaches near atmospheric levels. Moreover, each section experiences the expected trend of an increase in pressure as engine speed increases.

One slight difference between the two fuels is that F24 experiences slightly higher pressures at all sensor locations despite burning cooler. This slight difference is expected to be a result of the additives that affect the combustion of the fuel. When examining the simulation results, both fuels result in very similar pressure results, very similar to the experimental results. However, the magnitudes of these values were quite different. The drastic increase in pressure is due primarily to a number of numerical simulation assumptions made for the model's success that do not exist in physical experimentation. First, the numerical model is assumed to be perfectly sealed, and therefore, there are no pressure losses experienced in the simulation as a result. Furthermore, the lack of rotation in the model will result in a very drastic back pressure, especially around P3 and will result in higher pressures at other sensor locations. Another reason for the high pressures is the adiabatic assumption of the model. This assumption results in a pressure increase due to the higher temperatures experienced in the engine. The greatest pressure difference is found at 70,000RPM. Due to this large pressure value, other factors that rely on pressure calculations will see an increased percentage error at 70,000 RPM.

5.3.4 Engine Thrust

The engine thrust data was collected for both the numerical simulation and experimental results and compared for both fuels at all 3 engine speeds. As previously mentioned, experimental thrust data was collected using the button type Futek load cell. Simulation thrust data was collected by analyzing pressure data at the exhaust section and gas density. This data is shown below in Figure 62.

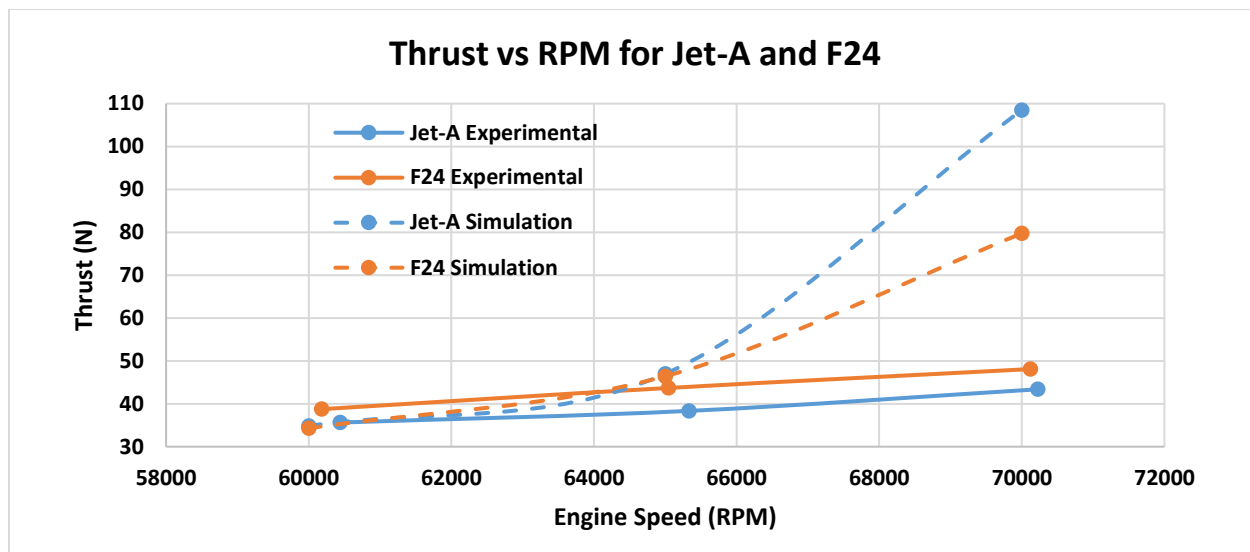


Figure 62: Turbine Thrust for both experimental and numerical simulation at each engine speed.

When examining the thrust data, both experimental and numerical simulation results indicate the expected trend of an increase in thrust as engine speed increases. When comparing the 2 different fuels, F24 produces a larger thrust at each engine speed, with the maximum increase found at 65,000 RPM with a 14% thrust increase. This increase in thrust is most likely due to the larger density of F24 as compared to Jet-A, resulting in a greater thrust output since both fuels lower heating values are approximately the same.

The numerical simulation results show good correlation with the experimental results. Excluding the high pressure resulting in high thrust results at 70,000 RPM, the maximum percentage error for F24 and Jet-A was found to be 11.5% and 22.6% respectively. Jet-A and F24 also have very similar simulation results. This further validates the model's accuracy. Better accuracy is attained at lower engine speeds. This is most likely due to the lower percentage differences of pressure at the lower engine speeds. This allows for a more accurate calculation of thrust.

5.3.5 Engine Fuel Flow

The fuel flow was measured using the inline piston type flowmeter and was calculated internally with a differential. The simulation fuel flow was determined based on the fuel velocity exiting the nozzle and the cross-sectional area of the fuel injectors. The results can be seen below in Figure 63.

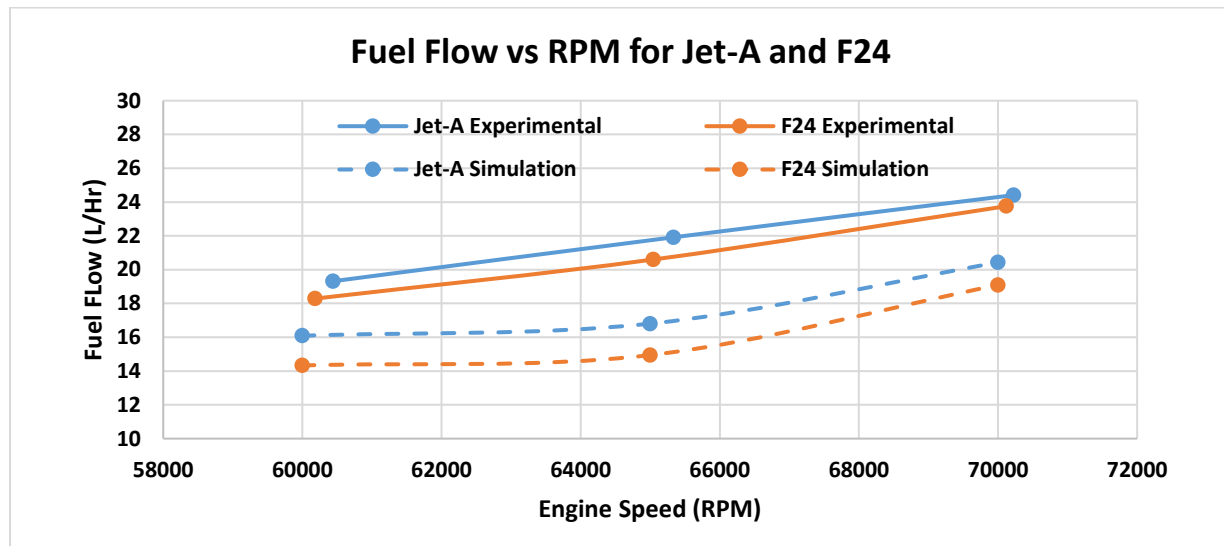


Figure 63: Turbine Fuel Flow rate for both experimental and numerical simulation at each engine speed.

The results of the fuel flow measurements reveal a very close similarity between F24 and Jet-A for both the numerical and experimental results. Since F24 is simply Jet-A with several additives, it is valid for both fuels to experience similar fuel flow rates. The primary reason for Jet-A to have a higher fuel flow rate is the viscosity levels. The higher viscosity of F24 results in a slower moving flow, despite the higher density. These similarities between the experimental results are also valid for the numerical simulation results. Despite the high magnitude difference between the numerical and experimental results, the general trends for both experiments are the same, where an increase in engine speed results in an increase in fuel consumption. The greatest percentage error came at engine speed of 65,000RPM, where Jet-A and F24 experienced a percentage error of 23.3% and 27.5% respectively.

5.3.6 Engine Air-Fuel-Ratio and Equivalence Ratio

The air fuel ratio results for both fuels are shown below in Figure 64 at each engine speed for both the simulated and experimental results. This data was collected experimentally using the compressor speed and the geometric dimensions of the engine to determine the air intake. Fuel flow was determined in previous sections.

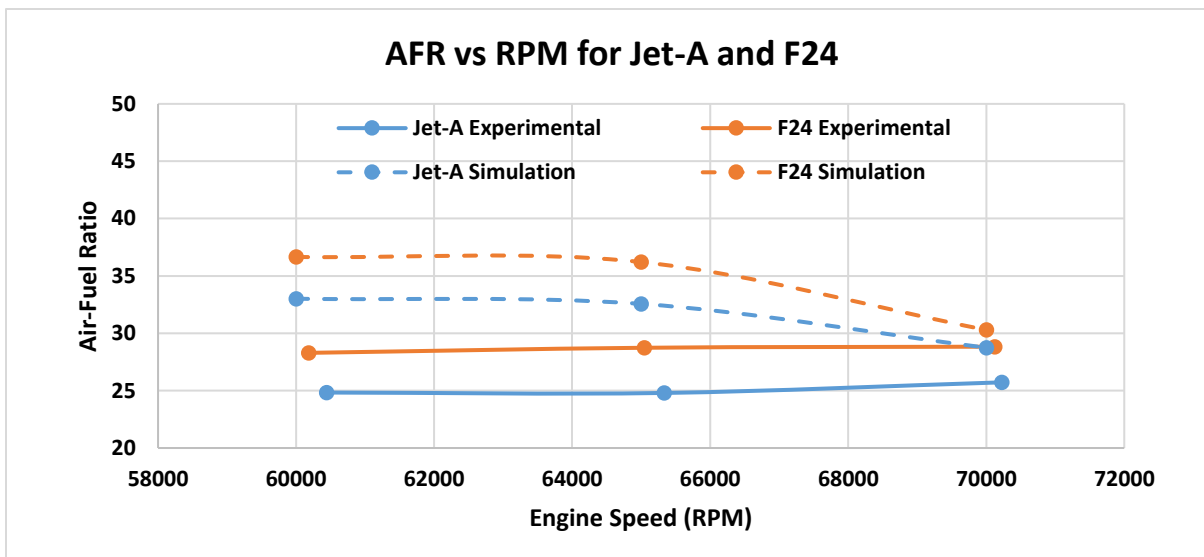


Figure 64: Turbine AFR for both experimental and numerical simulation at each engine speed.

As shown above, there are several conclusions to be made from the AFR comparisons. First, when analyzing the experimental results, there is a general trend of AFR increasing with engine speed. This change is very minimal, which is an expectation for this engine. Increasing speed requires an increase in fuel flow which results in the compressor doing more work. It is also obvious that F24 runs at a leaner AFR than Jet-A. This is primarily due to the fuel flow rate, which is affected by fuel characteristics, however coupling the leaner mixture with enhanced thrust performance results in F24 being more economical.

The simulated results show similar trends up to engine speed of 65,000 RPM and drop significantly at 70,000 RPM. It can also be observed that the simulated results are leaner than experimental. This can most likely be due to the losses the experimental compressor experiences in practice. The simulation sets

the compressor inlet mass flow rate, resulting in no losses and therefore pushing more air into the engine than would be experimentally provided. Another significant point in the simulated results is the relationship between the two fuels is the same as the experiment, where F24 is running leaner than Jet-A. Similar trends of the simulation to the experimental provide further evidence for the model validation.

The equivalence ratio results were compiled and presented in Figure 65 below for all cases.

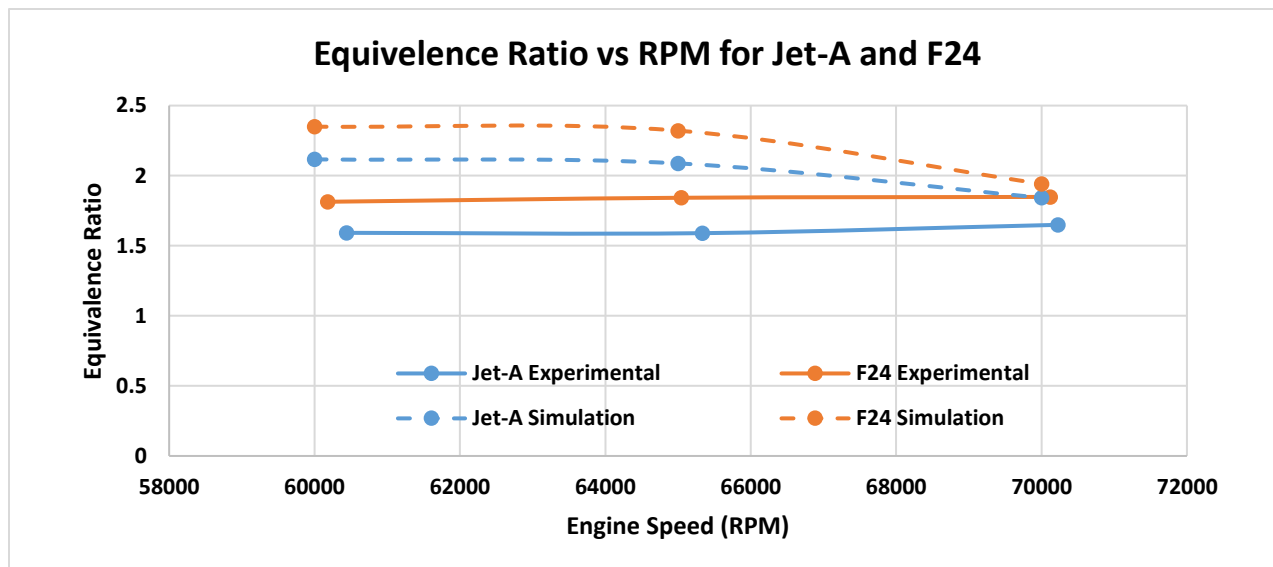


Figure 65: Turbine Equivalence ratio for both experimental and numerical simulation at each engine speed.

The equivalence ratio shows similar trends to that of the AFR due to the similarity in calculating the data. However, equivalence ratio allows for interpretation of how the engine is performing in reference to the expected AFR of the fuel itself. This results in a clearer idea of how the fuel is performing depending on its application. These experimental results indicate that this engine with both fuels ran leaner than the expected AFR, with F24 again being leaner than Jet-A. This may result in poor NO_x results, as there exists more oxygen and nitrogen to form NO_x even though F24 generally runs cooler.

5.3.7 Engine Thrust Specific Fuel Consumption

The thrust specific fuel consumption for each fuel at each engine speed and for both experimental and simulated results can be found in Figure 66 below. These results were calculated based on the ratio between fuel flow and thrust output.

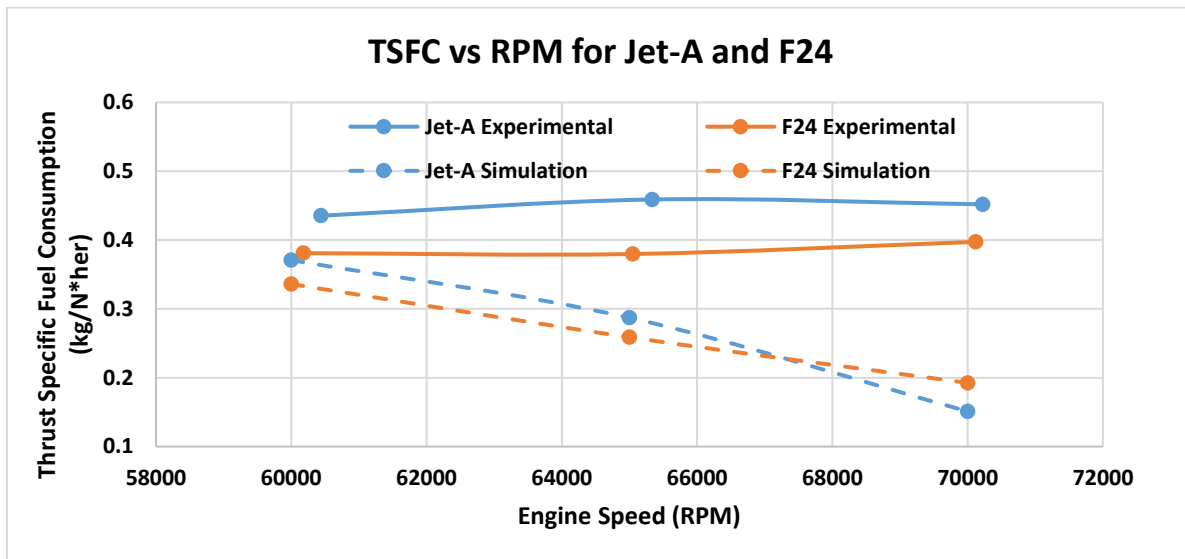


Figure 66: Turbine Thrust specific fuel consumption for both experimental and numerical simulation at each engine speed.

The results of the TSFC show experimentally that Jet-A has less efficiency than F24. This is primarily due to both the greater fuel flow rate of Jet-A and the lower thrust that is produced by Jet-A. Both factors again contribute to the fact that F24 is a more economical choice for fuel. These results indicate that engine speed has little effect on the TSFC, which is in line with the thermodynamic efficiency results gathered in this work. The simulation results are similar to the experimental results especially at lower engine speeds. This is a consistent trend seen throughout this work. Again, the lack of pressure loss and rotation in the turbine stage of the simulation has resulted in larger pressure spikes at higher engine speeds, which is currently affecting the TSFC. The trends for the simulated and experimental results are fairly similar as well, both showing Jet-A having a greater TSFC. However, Jet-A has greater TSFC at an engine

speed of 70,000 RPM. This is due to the reduction in difference between fuel flow rate of the two fuels at higher engine speeds coupled with the drastically larger thrust of Jet-A at 70,000 RPM in the simulation.

5.3.8 Engine Emissions Analysis

The emission analysis for these results were conducted as previously discussed in the methodology. The FTIR emissions gas analyzer was used to identify the 5 major species of interest when examining the harmful emissions produced from burning fossil fuels. These results were gathered for a sampling time of 90 seconds at each engine speed for each fuel. The results for all emissions as a PPM or percentage of total species present can be examined in table format in Table 13 in the Appendix. The results are also graphically represented for H₂O % and CO₂ % in Figure 67 below.

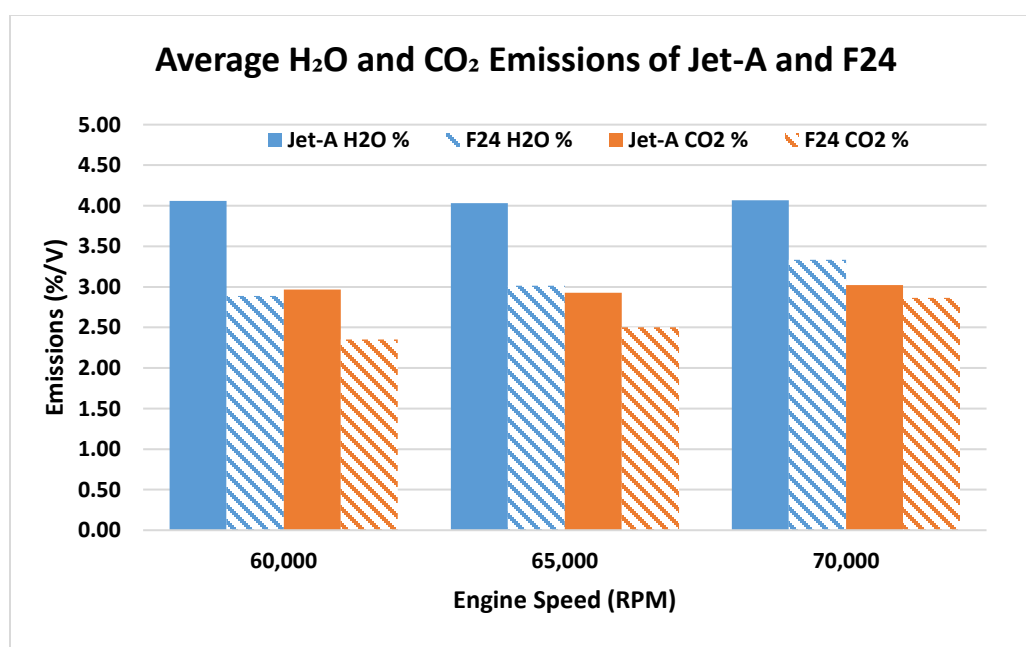


Figure 67: Average H₂O and CO₂ Percentage for Jet-A and F24

The results from the experimental emissions testing showcases the constant representation of H₂O and CO₂ in Jet-A combustion for each engine speeds. There is very little variation in these emissions results as compared to F24, which showcases a positive relationship between engine speed and emissions.

However, F24 has significantly lower levels of emissions as compared to Jet-A at all engine speeds. F24 showcases a decrease of H₂O emissions as great as 40.53%. Furthermore, CO₂ emissions are also significantly less for F24 than Jet-A, with a maximum percentage difference of 26.26% improvement. These starkest differences come from the lower engine speeds. This is likely due to the greater fuel flow rate of Jet-A as opposed to F24, as the difference in fuel flow rate decreases at higher engine speeds.

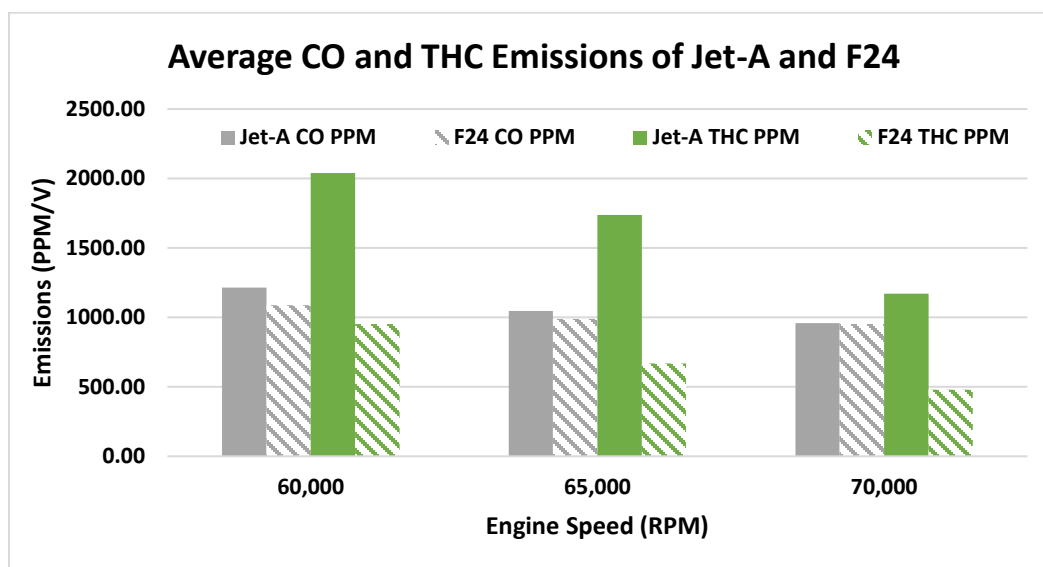


Figure 68: Average CO and THC PPM for Jet-A and F24

The emission results for the CO and THC can be viewed above in Figure 68. These results indicate that Jet-A has a greater production of CO and THC at all engine speeds as compared to F24. CO and THC are a product of incomplete combustion that occurs in the combustion chamber, indicating that Jet-A has a slightly greater amount of incomplete combustion despite the more favorable viscosity properties of Jet-A. It is possible that the slight difference in viscosity doesn't have significant enough effects to drastically improve the combustion. This is evident by the nearly equivalent CO production at 70,000 RPM. It can also be shown that there is a much greater amount of THC produced by Jet-A than F24, where Jet-A produces a maximum of 160% more THC than F24. The likely reason for this difference is the increased fuel flow rate of Jet-A as compared to F24. This would explain the massive difference between the THC (which correlates to the soot that is produced in combustion). As expected, the increase in engine speed decreases

the overall emissions produced for both Jet-A and F24. Jet-A does experience a greater improvement in CO production than F24 does resulting in a 26.47% improvement between engine speeds 60,000 to 70,000 RPM. This is likely due to the more favorable viscosity of Jet-A for combustion.

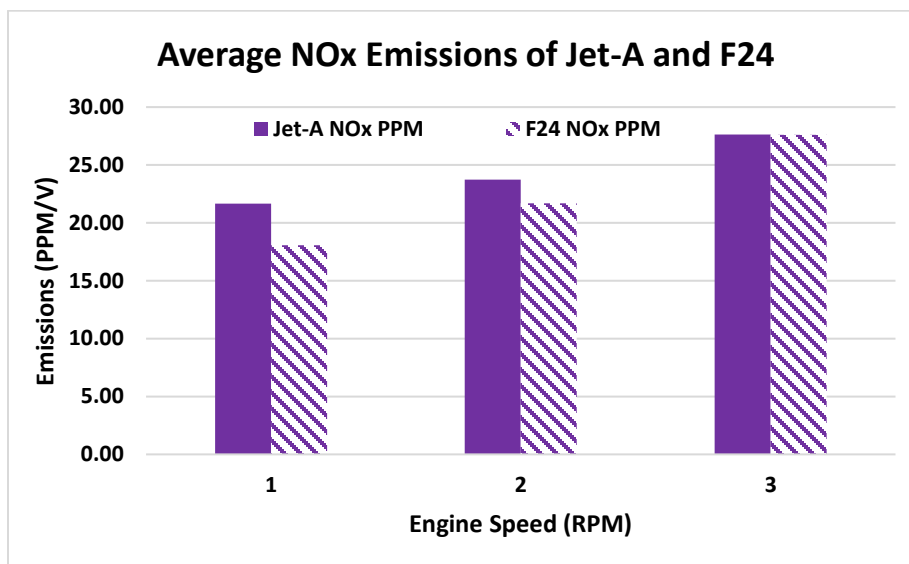


Figure 69: Average NOx PPM for Jet-A and F24

The results for the NOx emissions can be found in Figure 69 above. Nitrogen oxides are a product of nitrogen combining with oxygen at high temperatures, generally around 1700 K, which is well within the combustion flame temperature. Therefore, the availability of nitrogen and oxygen as well as flame temperature and combustion chamber temperature will drastically affect the NOx results. Based on the experimental results gathered, F24 generates 19.96% less NOx at an engine speed of 60,000 RPM. At the maximum engine speed, there is practically no difference in the NOx produced. Based on the temperature profile gathered experimentally, these values are expected, since F24 burns cooler than Jet-A. This leads to cooler engine temperatures throughout the engine and reduces the prime environment to form NOx.

The thrust specific emission data was also collected and analyzed to provide a more contextualized understanding of the emissions production. The thrust specific emissions data for H₂O and CO₂ can be found below in Figure 70.

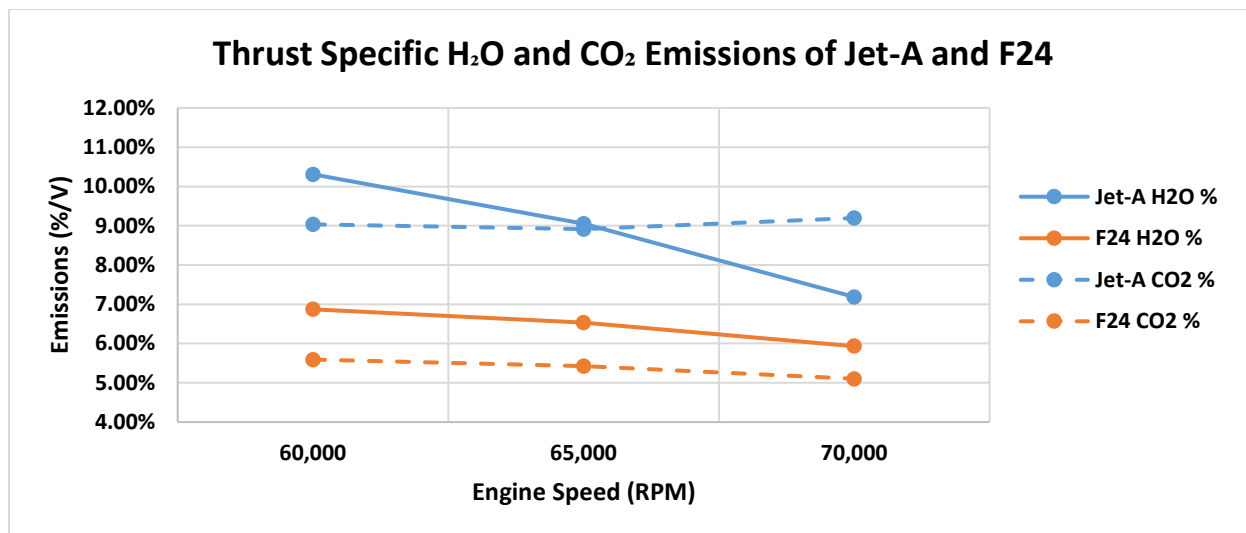


Figure 70: Thrust Specific H₂O and CO₂ percentage emissions for Jet-A and F24

Based on the results above and previous results, F24 has produced a greater amount of thrust least number of emissions across all parameters. These factors contribute to an increasing gap between the thrust specific emissions between Jet-A and F24. As shown above, Jet-A produces a greater percentage of H₂O and CO₂ at all engine speeds. As engine speed increases, Jet-A reduces the amount of H₂O produced due to the nearly constant H₂O output and the increase in thrust as engine speed increases. This change is much more drastic than F24 due to the slight increase of H₂O production by F24 with increasing engine speed. Jet-A also shows a positive relationship between thrust specific CO₂ and engine speed, while F24 shows a negative relationship. This is due again to the near constant output of CO₂ of Jet-A with increasing engine speeds. Overall, these results indicate that in most cases, increases in engine speed result in the production of less emissions.

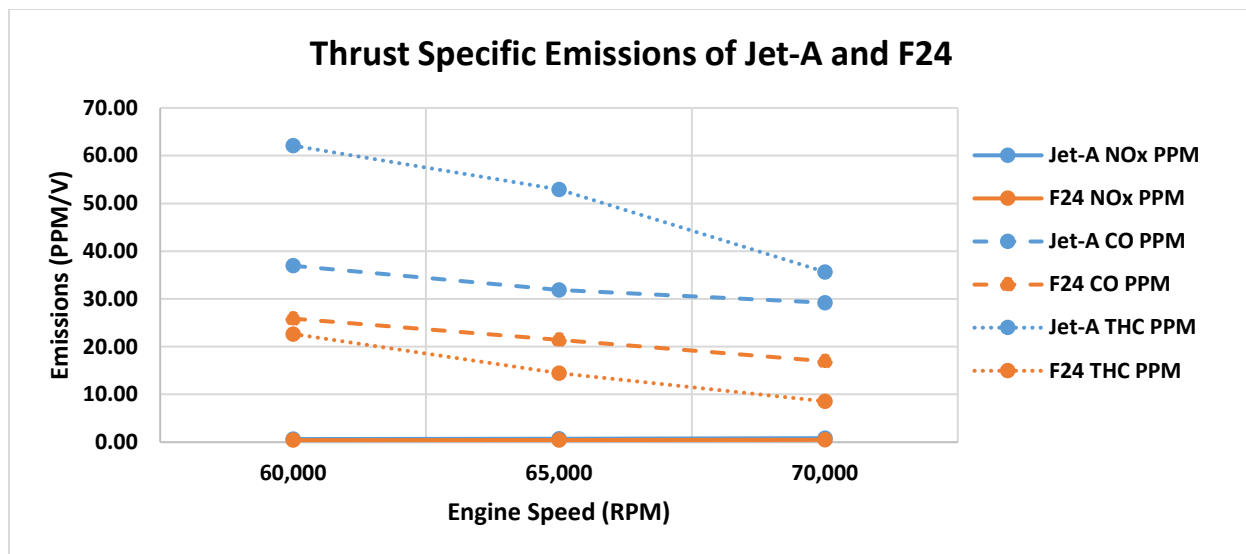


Figure 71: Thrust Specific CO, THC, and NOx PPM emissions for Jet-A and F24

The thrust specific emissions for NOx, CO, and THC were also compiled and analyzed. For similar reasons as previously mentioned, F24 performs better than Jet-A in terms of emissions produced at different engine speeds. As shown in Figure 71 above, F24 produces significantly less CO, NOx, and THC as engine speed increases and subsequently thrust increases. Both fuels also exhibit a negative relationship between engine speed and emissions, resulting in a decrease in thrust specific emissions with increasing engine speeds.

5.3.9 Engine Noise and Vibration Analysis

The noise and vibration analysis for Jet-A and F24 were performed at the 3 engine speeds of 60,000, 65,000, and 70,000 RPM, with the data collection period occurring for a minimum of 90 seconds to collect average values in the range. Sound pressure levels (SPL) were taken for both fuels and was collected using both the free field and multfield microphone to obtain the most accurate results available. As previously mentioned in the experimental methods, the free field microphone provides more accurate information when there is a single sound source with very little impact, and the multfield microphone is valuable in more noise chaotic areas. The data was collected with a frequency range of 16 kHz and was post-processed using the constant pressure bandwidth filter (CPB). This allowed the separation of the sound pressure levels

to the basic frequencies and enhanced the analysis process. Special attention will be placed in the frequency range of 200-500Hz, as this range defines combustion (Soloiu et al. 2021). The sound level results for each microphone and engine speed can be found between Figure 76 - Figure 81.

The first observation made by examining these figures is the increase in SPL as engine speed increases. As engine speed increases, both Jet-A and F24 experience an overall maximum increase in SPL of 7.4% and 3.5% respectively. As previously discussed, Jet-A was seen as a more volatile fuel. This more rapid increase in SPL seems to further validate the conclusions drawn from the fuel analysis. It was also observed that F24 generally has a larger magnitude of SPL over the full range from 0Hz – 16kHz. This result is understandable based on the work conducted by Strahle and Sharma, both approaching the reason for F24's higher SPL from a different perspective. Strahle found that fuels with longer combustion delays generally have a greater SPL profile than those with shorter combustion delays (Strahle 1972). F24 has a longer combustion delay and ignition delay, therefore, for F24 to exhibit greater magnitudes of SPL is expected. Meanwhile, Sharma also investigated the SPL, but from the perspective of the molecular content of the fuel. Sharma found that fuels with lower aromatic content would generally result in greater levels of noise pollution (Sharma et al. 2020). The higher aromatic content provides a dampening to the SPL values of the fuel. Based on these findings, it would be expected to see F24 having greater SPL values. This can be clearly examined by investigating the combustion chamber magnitude and increase with respect to engine speed. F24 has consistently louder combustion chamber SPL levels and increases at a greater rate than Jet-A, where F24 increases by 12.1% and Jet-A increases by only 6.6%. It is also examined that the Freefield graphs have a more parabolic shape than the linearity of the Multifield graphs. This is most likely due to the placement of the microphones. There is more likely more interference with the multifield microphone being placed near the exhaust section of the turbine. The free field microphone is placed perpendicular to the flow of the gas, allowing for a more focused sound wave. This may also explain why the free field results exhibit a maximum SPL of 107 dB for Jet-A. Full sound pressure data can be found in Table 15.

The vibration analysis was conducted under the same methods discussed for the SPL. A triaxial accelerometer was used to collect the raw acceleration data, and a Fast Fourier Transform (FFT) was used to convert the signal from the time domain to the frequency domain. Data was processed up to 25.6kHz, with special emphasis placed on the engine's natural frequencies, including the shaft rotation, exhaust struts, compressor blades, and turbine blades. The FFT was unable to capture results based on the previously identified range of frequencies. Therefore, the turbine blades will not be analyzed at this time. The frequencies of interest can be found in Table 9 below and the results from the experiments can be found in Figure 73 - Figure 75.

Table 9: Vibration properties of the engine with corresponding component frequency

Parameters	Average Noise and Vibration		
	RPM	60,000	65,000
Shaft Rotation (kHz)	1	1.083	1.167
3 Exhaust Struts (kHz)	3	3.250	3.501
12 Compressor Blades (kHz)	12	13	14
24 Turbine Blades (kHz)	24	26	28

The primary observations when examining the FFT results for the two fuels are the general trends in the engine with increasing engine speed and the difference in vibrational amplitude between the two fuels. Starting with the compressor section, both fuels exhibit a general trend of increasing in vibrational amplitude over time. As engine speed increases, air mass flows into the engine increases. This results in greater potential for non-uniformity in the concentric air-dynamics impressed upon the compressor blades. Furthermore, increasing the engine rotation speed can have a significant effect on the wake dynamics that each blade has on the others (Tereshchenko et al. 2015). This increased wake effect coupled with the increased potential for non-uniformity air-dynamics that affect the compressor blades explains the general

increase in vibrational amplitude as engine speed increases for both fuels. When examining the differences between the two fuels, F24 clearly has a much larger vibrational amplitude than that of Jet-A, where F24 and Jet-A exhibit a maximum of approximately $340 \text{ m}^2/\text{s}^2$ and $140 \text{ m}^2/\text{s}^2$ respectively. This larger difference in the vibration can be explained by a few different phenomena in the engine. When examining the equivalence ratio of the two fuels, F24 clearly runs leaner than Jet-A. This, coupled with the enhanced thrust of F24, indicates that the compressor may be working harder and bringing in more air than when Jet-A is being used. Therefore, greater levels of dynamic non-uniformity and wake interactions can be expected, leading to higher magnitudes of vibration. Moreover, studies have shown to link the aromatic content of fuels to the combustion stability in an engine (Wijesinghe, Ling, and Khandelwal 2019). Since the aromatic content of Jet-A (including but not limited to Naphthalene, Xylene, Benzene, Toluene, etc.) is significantly greater than that of F24 (Guzman and Brezinsky 2021), this may very likely be one of the sources of the higher vibrational amplitude of F24.

A vibration analysis can also be conducted for the exhaust struts. Based on the FFT results, there is a general decreasing trend as engine speed increases. This trend for both fuels is most likely due to the increased velocity of the flow in this section. The increase in velocity results in a decrease in the size of the wake produced by the struts. Therefore, increasing the engine speed results in a reduced wake interference between the struts, and leading to less vibration in this subsection of the system. It can also be observed that F24 exhibits greater levels of vibration than Jet-A, with a maximum vibration of $122 \text{ m}^2/\text{s}^2$ and $100 \text{ m}^2/\text{s}^2$ respectively. The difference between these two vibrational amplitudes is most likely due to the higher pressure in this section of the engine for F24. As previously reported by Mir et al, an increase in the pressure in a vessel will result in an increase in the vibrational amplitude inside the vessel (Mir, Shakouri, and Ashory 2019). Therefore, the higher vibrational amplitude seen in the exhaust struts of F24 is an expected phenomenon.

Finally, when examining the shaft, Jet-A and F24 exhibit a divergence in vibrational amplitude as engine speed increases. Jet-A increases in vibration acceleration while F24 decreases. This difference could

be due to the difference in the combustion phenomenon of both fuels. As discussed in Soloiu et al (Valentin Soloiu 2022), the elongation of the CD and ID of F24 combustion as compared to Jet-A results in less pressure ringing after combustion. This results in smooth combustion and less vibration, which could affect both the trends of these fuels and explains why F24 demonstrates a lower vibrational amplitude than Jet-A.

CHAPTER 6

FINDINGS, CONCLUSIONS, AND RECOMMENDATIONS

6.1 Conclusions

This research comprehensively examined the differences between military F24 fuel and commercial jet fuel Jet-A through a multifaceted approach. First the thermochemical and physical properties of both fuels was analyzed to provide a detailed understanding of the fuel and was used to help predict the engine performance characteristics. This was done using a multitude of fuel analysis equipment, including a Brookfield viscometer, Phase One Jet Fuel Analyzer, Shimadzu DTG-60, Malvern MIE Scattering He-Ne laser, Constant Volume Calorimeter, and a Constant Volume Combustion Chamber. Engine performance was analyzed using a small-scale turbojet engine instrumented with K-type thermocouples, pressure transducers, tachometers, load cells (for thrust), and flow meters into high-speed data acquisition system. Noise data was collected using a free-field and multifold microphone, and vibration data collected using a triaxial accelerometer. This data was processed using the FFT function in the BK Connect software. Emissions data was collected using the FT-IR gas emissions analyzer and emphasized the investigation of CO₂, H₂O, CO, THC, and NO_x. Finally, a numerical simulation was developed using CFX. The existing Jet-A fuel library data was modified to include various in-house validated properties (like viscosity and density) and researched F24 Nasa Polynomial information to generate an experimental F24 surrogate fuel in the software. By creating the F24 surrogate fuel in CFX the flow field patterns, the combustion flame front of and the emissions generated by combustion could all be examined for both fuels for the purpose of validating the CFX model. Experimentation was conducted at 3 different engine speed (60,000, 65,000, 70,000)

In comparing the two fuels, it was found that F24 proves to be the more economical, provides greater performance, and is a more environmentally friendly fuel as compared to Jet-A. This conclusion is based on several critical data points, including the full lower engine temperature of using F24 than that of

using Jet-A. This lower temperature will improve engine life and result in less maintenance required on the engine over time. Moreover, F24 produces greater thrust at a lower fuel flow rate, resulting in a greater thrust specific fuel consumption and resulting in a more cost-effective fuel despite the higher thermodynamic efficiency of Jet-A. This is further visualized in the AFR, where F24 runs leaner than Jet-A. The emissions of the two fuels also demonstrate the efficiency of F24. F24 was shown to produce less emissions for every species investigated at every engine speed investigated. The use of F24 resulted in a maximum of 40.53% decrease in H₂O, a decrease of 26.26% in CO₂ emissions, a decrease of 11.56% in CO emissions, a decrease of 160% in THC emission, and a decrease of 19.96% in NO_x emissions. The drastic decrease in emission produced coupled with the increased thrust per engine speed results in a much-improved thrust specific emissions result as well for F24 as compared to Jet-A. For the engine noise and vibration of F24 as compared to Jet-A, F24 generally has a greater sound pressure levels and vibration amplitude levels than that of Jet-A. The greater SPL for F24 would require ATC teams to be better equipped with PPE to reduce the harmful effect of the higher SPL. The greater vibration results would also result poorly for the maintenance of F24 run engines, where greater fatigue would be experienced in the same engine running F24 as compared to Jet-A. However, the longer injection delay and combustion delay of F24 results in smoother combustion and less vibration, specifically in the shaft frequency zones. Based on these results and maintenance decisions on different components of the engine, F24 may result in more positive factors that would encourage the use of the fuel.

The results from this numerical simulation found many encouraging results for the validation of the numerical model when using F24 fuel. Across all parameters, the Jet-A and F24 numerical models followed very similar trends as the experimental results. Increases in engine speed resulted in increases in thrust, fuel consumption, temperature and pressure profiles, and emissions. This indicates accuracy in the model to predict the trends of the engine. When examining the accuracy of the model, the temperature profiles for both fuels provided agreeable results for T2 and T4, with percentage errors lower than 12.75% for both fuels. T3 and T5 showed some inconsistency depending on the engine speed. For example, T3 and

T5 had high accuracy of less than 7.35% at 65,000RPM. However, a percentage error of 31% was recorded at the 2 outer extreme engine speeds. This trend was similar for the pressure profile, exhibiting large percentage errors due to the assumption that were required for the model. The pressure profile at 70,000RPM resulted in some large percentage errors for other parameters at that engine speed, whereas lower engine exhibited accurate results. The numerical model provided valuable information on the internal and immeasurable parameters that could not be determined experimentally. Velocity profiles showcased the increased swirl flow at higher engine speeds and the turbulent kinetic energy contours providing location of high energy turbulent eddies inside the engine. This information on the flow path provides valuable data on how to improve these flow paths to reduce turbulence inside the exhaust and turbine sections and enhance the turbulence where air-fuel mixing is required. Furthermore, the emissions contours (specifically H₂O and CO₂) showcased the difference in molecular structure of F24 through the reduction of H₂O and CO₂ emissions.

6.2 Future Work

The examination of engine performance is a necessary step in developing a more economical and environmentally friendly engine. Research in this area will help reduce the large dependence of fossil fuels in the aviation industry and move towards the goals of airline and aviation company achieving a net-zero carbon footprint on the environment. For this experimentation and setup, there are a several improvements that can be made to enhance the data collected. The incorporation of a hot-wire anemometer would be a valuable step in enhancing the data collected. This air velocity measurement would further validate and confirm the air intake of the engine and enhance the precision of data collected. This enhancement has been developed and instrumented into the engine; however, integration of the anemometer data signals into the high-speed data acquisition system would greatly improve the setup. The implementation of more differential pressure transducers in the form of pitot tubes into the circumference of the engine would allow for a real improvement in data collection capability, as this information would help characterize the swirl number inside the engine directly before the combustion chamber.

In future research both experimentally and numerically, more investigation should be centered on the implementation of alternative and synthetic fuels. Experimentally, this would provide good information on how these different fuels perform under similar conditions. Numerically, the expansion of this work by using alternative and synthetic fuels would enhance the current scientific community's database on the combustion of these fuels. Despite the importance of these fuels for reducing harmful emissions, there is very little public numerical simulation research published on the implementation of these alternative fuels like IPK and S8. This represents a significant opportunity to make real contributions not only to internal labs, but to the general scientific community.

Finally, more investigation should be undertaken to improve the pressure and differences between the experimental and numerical results. Improvement in this area represents a significant step towards further validating the model. This may be done through altering the fuel injection rate of the model to match more closely to that of the experimental results. It may also be done through implementing more boundary conditions to take into account pressure losses experienced through seals, and compressor work loss. By identifying leaks in the engine, the location of boundary conditions can be placed. The adiabatic settings on the model should also be altered to reduce both temperature and pressure increases that were seen when comparing experimental and numerical results. These enhancements would require an improvement in computing power and/or will require more time for computation and are dependent on resources. Finally, improvement in grid resolution would be a significant improvement, as the current grid is the best available option when considering computational resources.

6.3 Special Thanks

A special thanks goes to the sponsor of this research, the Aerospace NSF-DoD Award #1950207

REFERENCES

2020. "Kinematic Viscosity." [Webpage]. Engineering Clicks, accessed December 15. <https://www.engineeringclicks.com/kinematic-viscosity/#:~:text=Rheopectic%20fluids%20%E2%80%93%20these%20increase%20in%20viscosity%20when,decrease%20in%20viscosity%20when%20shaken%2C%20e.g.%20tomato%20ketchup.>
- Academic. 2023. "Turbofan." [Webpage], accessed 03/15/2024. <https://en-academic.com/dic.nsf/enwiki/9560>.
- Acharya, Sanjay. 2008. A General Electric J85-GE-17A turbojet engine (1970). This engine was used in a Cessna A-37 attack aircraft for ground-support missions during the Vietnam War. Wikipedia.
- Administrators, Mech4Study. 2017. "Difference between Impulse and Reaction Turbine." [Webpage], accessed 03/15/2024. https://www.mech4study.com/fluid-mechanics/difference-between-impulse-and-reaction-turbine.html/#google_vignette.
- Administrators, Mech4Study. 2023. "Turbojet Engine : Construction, Working, Advantages and Disadvantages." [Webpage], accessed 03/15/2024. <https://www.mech4study.com/thermal-engineering/turbojet-engine-construction-working-advantages-and-disadvantages.html/>.
- Almohammadi, Bandar Awadh, Paramvir Singh, Saurabh Sharma, Sudarshan Kumar, and Bhupendra Khandelwal. 2021. "Experimental investigation and correlation development for engine emissions with polycyclic aromatic blended formulated fuels." *Fuel* 303:121280. doi: <https://doi.org/10.1016/j.fuel.2021.121280>.
- Altarazi, Yazan S. M., Abd Rahim Abu Talib, Ezanee Gires, Jianglong Yu, John Lucas, and Talal Yusaf. 2021. "Performance and exhaust emissions rate of small-scale turbojet engine running on dual biodiesel blends using Gasturb." *Energy* 232. doi: 10.1016/j.energy.2021.120971.
- Amezcuca, Eri R., Kenneth Kim, David Rothamer, and Chol-Bum Kweon. 2022. "Ignition Sensitivity Analysis for Energy-Assisted Compression-Ignition Operation on Jet Fuels with Varying Cetane Number." *SAE International Journal of Advances and Current Practices in Mobility* 4 (5):1651-1666. doi: 10.4271/2022-01-0443.
- Anna Snakowska, Henryk Idczak. 2008. "PREDICTION OF TURBOFAN ENGINE NOISE CONSIDERING DIFFRACTION AT THE DUCT OUTLET." *Archives of Acoustics* 33.
- ANSYS. 2011a. ANSYS CFX-Solver Theory Guide. ANSYS.
- ANSYS. 2011b. Ansys CFX Solver Modeling Guide. ANSYS.
- ANSYS. 2020. "Fully Developed Internal Turbulent FLoWs in Ducts and Pipes." [Webpage]. ANSYS, accessed 02/09/2024. <https://courses.ansys.com/wp-content/uploads/2020/09/Lesson-2-Fully-Developed-Internal-Turbulent-Flows-in-Ducts-and-Pipes-Handout.pdf>.
- ArkSolo. 2017. Boeing 777X General Electric GE9X Aircraft Engine. favepng.com.
- B. Tesfa, F. Gu, R. Mishra, A.D. Ball. 2013. "LHV predication models and LHV effect on the performance of CI engine running with biodiesel blends,." *Energy Conversion and Management* 71:217-226. doi: <https://doi.org/10.1016/j.enconman.2013.04.005>.
- Badami, M., P. Nuccio, D. Pastrone, and A. Signoretto. 2014. "Performance of a small-scale turbojet engine fed with traditional and alternative fuels." *Energy Conversion and Management* 82:219-228. doi: 10.1016/j.enconman.2014.03.026.

- Badami, M., P. Nuccio, and A. Signoretto. 2013. "Experimental and numerical analysis of a small-scale turbojet engine." *Energy Conversion and Management* 76:225-233. doi: 10.1016/j.enconman.2013.07.043.
- Baskharone, Erian A. 2006. "Principles of Turbomachinery in Air-Breathing Engines." [Webpage]. Global Spec, accessed 03/15/2024. <https://www.globalspec.com/reference/74140/203279/chapter-nine-axial-flow-compressors>.
- Benini, Ernesto, Sergio Pandolfo, and Serena Zoppellari. 2009. "Reduction of NO emissions in a turbojet combustor by direct water/steam injection: Numerical and experimental assessment." *Applied Thermal Engineering* 29 (17-18):3506-3510. doi: 10.1016/j.applthermaleng.2009.06.004.
- Bishop, Geoff J., and Barbara Elvers. 2021. "Aviation Turbine Fuels*." In *Handbook of Fuels*, 503-527.
- BYJU. 2023. "Heat of Combustion." [Webpage]. BYJU, accessed 12/22/2023. <https://byjus.com/chemistry/heat-of-combustion/>.
- Chiariello, F., C. Allouis, F. Reale, and P. Massoli. 2014. "Gaseous and particulate emissions of a micro gas turbine fuelled by straight vegetable oil–kerosene blends." *Experimental Thermal and Fluid Science* 56:16-22. doi: 10.1016/j.expthermflusci.2013.11.013.
- Co., Phase Analyzer. 2017. JFA-70XiAS COLD FLOW PROPERTIES FUEL AUTOSAMPLER ANALYZER SYSTEM USER GUIDE.
- Dianne Luning Prak, Jay Cooke, Terrence Dickerson, Andy McDaniel, Jim Cowart,. 2021. "Cetane number, derived cetane number, and cetane index: When correlations fail to predict combustibility." *Fuel* Volume 289 (Fuel). doi: <https://doi.org/10.1016/j.fuel.2020.119963>.
- Dubovas, Andrius, and Domantas Bručas. 2021. "Research on Characteristics of Turbo Jet Engine Combustion Chamber." *Aviation* 25 (1):65-72. doi: 10.3846/aviation.2021.14398.
- Economics, Airline. 2018. "GE'S AFFINITY TO POWER THE AERION AS2 SUPERSONIC BUSINESS JET." [Webpage], accessed 03/15/24. <https://www.aviationnews-online.com/technology/ges-affinity-to-power-the-aerion-as2-supersonic-business-jet/>.
- EIP. 2022. "Gasoline Explained." [Webpage]. U.S. Energy Information Administration, accessed 12/22/2023. <https://www.eia.gov/energyexplained/gasoline/octane-in-depth.php>.
- Energy, Clark. 2020. "Heating Value." [Webpage]. Kohler Company, accessed 12/22/2023. <https://www.clarke-energy.com/heating-value/>.
- Engineering, Georgia Southern University Department of Mechanical. 2023. Biofuels testing Instruction Manual. Statesboro, GA: Georgia Southern University.
- FAA. 2014. Special Airworthiness Information Bulletin Engine Fuel - NATO Grade F-24 Jet Fuel. edited by Federal Aviation Administration.
- flight-mechanic. 2023. Exhaust Systems with Turbocharger (Part 2). Pintrest.
- Gawron, B., and T. Bialecki. 2017. "Impact of a Jet A-1/HEFA blend on the performance and emission characteristics of a miniature turbojet engine." *International Journal of Environmental Science and Technology* 15 (7):1501-1508. doi: 10.1007/s13762-017-1528-3.
- Gawron, Bartosz, Tomasz Bialecki, and Urszula Kaźmierczak. 2016. "Performance and Emission Characteristic of Miniature Turbojet Engine Fed Jet a-1/Alcohol Blend."

- Journal of KONES. Powertrain and Transport* 23 (1):123-130. doi: 10.5604/12314005.1213540.
- Gonzalez, C., K. C. Wong, and S. Armfield. 2007. "Computational study of a micro-turbine engine combustor using Large Eddy Simulation and Reynolds Averaged turbulence models." *ANZIAM Journal* 49:407-422. doi: 10.21914/anziamj.v49i0.338.
- Gordon Chiu, Charles Clutter, Larry Spino, PAC. 2018. IS MEASURING JET FUEL VISCOSITY MORE ACCURATE THAN FREEZING POINT? : Petro Industry News.
- Grall, Drake. 2021. "NUMERICAL AND EXPERIMENTAL ANALYSIS OF COMBUSTION AND EMISSIONS CHARACTERISTICS OF A SINGLE-STAGE JET ENGINE USING JET-A."
- Gürbüz, Habib, Hüsameddin Akçay, Mustafa Aldemir, İsmail Hakkı Akçay, and Ümit Topalçı. 2021. "The effect of euro diesel-hydrogen dual fuel combustion on performance and environmental-economic indicators in a small UAV turbojet engine." *Fuel* 306. doi: 10.1016/j.fuel.2021.121735.
- Guzman, Juan, and Kenneth Brezinsky. 2021. "Experimental and modeling study of the oxidation of F-24 jet fuel, and its mixture with an iso-paraffinic synthetic jet fuel, ATJ." *Combustion and Flame* 224:108-125. doi: 10.1016/j.combustflame.2020.12.008.
- Hamit Solmaza, Hasan Yamık, Yakup İçingüra & Alper Calam. 2014. "Investigation of the effects of civil aviation fuel HetA1 blends on diesel engine performance and emissions characteristics." *Indian Journal of Engineering & Materials Science* 21.
- Harsh, Goyal, and Kook Sanghoon. 2019. "Ignition process of gasoline compression ignition (GCI) combustion in a small-bore optical engine." *Fuel* 256:115844. doi: <https://doi.org/10.1016/j.fuel.2019.115844>.
- Hoxie, A., and M. Anderson. 2017. "Evaluating high volume blends of vegetable oil in micro-gas turbine engines." *Renewable Energy* 101:886-893. doi: 10.1016/j.renene.2016.09.054.
- Hunecke, Klaus. 1997. *Jet Engines Fundamental of Theory, Design and Operation*. Ramsey Marlborough: Airlife Publishing.
- John Wesley, Dr G. Jims, and Swati Chauhan. 2019. "Modeling and Performance Simulation of a Micro Turbojet Engine Using FlowNex." *Indian Journal of Science and Technology* 12:1-5. doi: 10.17485/ijst/2019/v12i22/131030.
- Kalvakala, Krishna C., Pinaki Pal, Jorge Pulpeiro Gonzalez, Christopher P. Kolodziej, Hee Je Seong, Goutham Kukkadapu, Matthew McNenly, Scott Wagnon, Russell Whitesides, Nils Hansen, and Suresh K. Aggarwal. 2022. "Numerical analysis of soot emissions from gasoline-ethanol and gasoline-butanol blends under gasoline compression ignition conditions." *Fuel* 319:123740. doi: <https://doi.org/10.1016/j.fuel.2022.123740>.
- Khandelwal, Bhupendra, Swapneel Roy, Charles Lord, and Simon Blakey. 2014. "Comparison of Vibrations and Emissions of Conventional Jet Fuel with Stressed 100% SPK and Fully Formulated Synthetic Jet Fuel." *Aerospace* 1 (2):52-66. doi: 10.3390/aerospace1020052.
- Lei Qui, Xi Zeng, Shiming Ji, Fengfei Xi, Wenbin Qiu, Qianqian Zheng. 2018. "Research on Combustion Chamber Structure Improvement and Ignition System of Missile Turbojet Engine for Diesel Fuel." *Tehnicki vjesnik - Technical Gazette* 25 (6). doi: 10.17559/tv-20180807223114.
- Malar, Mekaniz. 2012. Turboprop Engine. Youtube.
- Marines, US. 2014. USMC Policy on converting Conus Aviation and Ground/Tactical Equipment from JP-8 to F-24. edited by JAMES SEIPPEL. Washington.

- Matthaiou, Ioannis, and Ifigeneia Antoniadou. 2016. *Towards a condition monitoring scheme for thermoacoustic instability detection and fuel blend performance classification using machine learning*.
- Matthaiou, Ioannis, Bhupendra Khandelwal, and Ifigeneia Antoniadou. 2017. "Vibration Monitoring of Gas Turbine Engines: Machine-Learning Approaches and Their Challenges." *Frontiers in Built Environment* 3. doi: 10.3389/fbuil.2017.00054.
- mechanical-engg. 2023. Comparison of Gas Turbine with I.C. Engine. Pinterest.
- Mind, Experts. 2024. "Centrifugal flow - compressors in aircraft." [Webpage], accessed 03/15/24. <https://www.expertsmind.com/questions/centrifugal-flow-compressors-in-aircraft-30111554.aspx>.
- Mir, Omid, Meisam Shakouri, and M. R. Ashory. 2019. "Gas pressure and density effects on vibration of cylindrical pressure vessels: analytical, numerical and experimental analysis." *SN Applied Sciences* 2 (1):134. doi: 10.1007/s42452-019-1916-z.
- MKS_Instruments_Inc. 2020. Model 2030 CEM MultiGas FTIR Gas Analyzer. MKS Instruments Incorporated.
- Nemeth, R. 2017. "COMBUSTION PROCESS IN THE GAS TURBINE ENGINE COMBUSTORS." 2017.
- Nicholas Cumpsty, Andrew Heyes. 2015. *Jet Propulsion: a simple guide to the aerodynamics and thermodynamic design and performance of jet engines*. 3 ed. New York: Cambridge University Press.
- Notes, Aerospace. 2021. "CLASSIFICATION OF COMBUSTION CHAMBER." [Webpage], accessed 03/15/2024. <https://aerospacenotes.com/classification-of-combustion-chamber/>.
- Ohad Gur, Jacob Feldman. 2023. "Engine-Propeller Matching." Israel Annual Conference on Aerospace Sciences, Tel-Aviv, Israel, 03/2023.
- Parr_Instrument_Company. 2014. "Series 1341 Plain Jacket Oxygen Combustion calorimeters." [Webpage]. Parr Instrument Company, accessed 12/22/2023.
- Parr_Instrument_Company. 2021. "6772 Calorimetric Thermometer." Parr Instrument Company, accessed 12/22/2023. <https://www.parrinst.com/products/oxygen-bomb-calorimeters/6772-calorimetric-thermometer/>.
- Praga. 2016. "Praga News." [Webpage], accessed 03/15/2024. <https://pragaglobal.com/ge-h80-turboprop-engine-by-ge-aviation-czech/>.
- Rao, Shunlu, Zhaolei Zheng, and Chao Yang. 2023. "Effect of Cyclohexane on the Combustion Characteristics of Multi-Component Gasoline Surrogate Fuels." *Molecules* 28 (11). doi: <https://doi.org/10.3390/molecules28114273>.
- Roylance, David. 2000. "Shear and Torsion." Massachusetts Institute of Technology. https://ocw.mit.edu/courses/3-91-mechanical-behavior-of-plastics-spring-2007/7cef9270278ccb2fef0671826f176a6b_07_torsion.pdf.
- Rui Xu, Hai Wang, Med Colket, Tim Edwards. 2015. Thermochemical Properties of Jet Fuels.
- Ryder, R., R. C. Hendricks, M. L. Huber, and D. T. Shouse. 2010. "Computational Analysis of Dynamic SPK(S8)-JP-8 Fueled Combustor-Sector Performance." *13th International Symposium on Transport Phenomena and Dynamics of Rotating Machinery 2010, ISROMAC-13*:603-613.
- Ryu, Je Ir, Keunsoo Kim, Kyungwook Min, Riccardo Scarcelli, Sibendu Som, Kenneth S. Kim, Jacob E. Temme, Chol-Bum M. Kweon, and Tonghun Lee. 2021. "Data-driven chemical kinetic reaction mechanism for F-24 jet fuel ignition." *Fuel* 290. doi: 10.1016/j.fuel.2020.119508.

- Ryu, Je Ir, Austen Motily, Tonghun Lee, Riccardo Scarcelli, Sibendu Som, Kenneth Kim, and Chol-Bum Kweon. 2020. "Ignition Enhancement of F-24 Jet Fuel by a Hot Surface for Aircraft Propulsion Systems." In *AIAA Scitech 2020 Forum*.
- Sajesh, Sanker, Prakash, Das. 2014. "Performance analysis of a micro turbojet engine." *Transactions on Engineering and Sciences 2* (2).
- Sallevelt, J. L. H. P., J. E. P. Gudde, A. K. Pozarlik, and G. Brem. 2014. "The impact of spray quality on the combustion of a viscous biofuel in a micro gas turbine." *Applied Energy* 132:575-585. doi: <https://doi.org/10.1016/j.apenergy.2014.07.030>.
- Sharma, Saurabh, Paramvir Singh, Bandar Awadh Almohammadi, Bhupendra Khandelwal, and Sudarshan Kumar. 2020. "Testing of formulated fuel with variable aromatic type and contents in a compression-ignition engine." *Fuel Processing Technology* 208:106413. doi: <https://doi.org/10.1016/j.fuproc.2020.106413>.
- Shimadzu. 2023. Thermal Analysis Instruments 60 Series.
- Soloiu, Valentin, Remi Gaubert, Martin Muinos, Jose Moncada, Thomas Beyerl, Gustavo Molina, and Johnnie Williams. 2017. "Performance of an Indirect Injected Engine Operated with ULSD#2 Blended with Fischer-Tropsch Synthetic Kerosene."
- Soloiu, Valentin, Lily Parker, Richard Smith, III, Amanda Weaver, Austin Brant, Aidan Rowell, and Marcel Ilie. 2022. "Development of a Synthetic Surrogate for F-24 From Blends of Iso-Paraffinic Kerosene (IPK) and Fischer-Tropsch Synthetic Kerosene (S8) in a Constant Volume Combustion Chamber (CVCC)." ASME 2022 ICE Forward Conference.
- Soloiu, Valentin, Camille J. Phillips, Cesar Carapia, Aliyah Knowles, Drake Grall, and Richard Smith. 2021. "Exploratory Investigation of Combustion and NVH Signature of a Drone Jet Engine Fueled with IPK." *AIAA Scitech 2021 Forum*. doi: 10.2514/6.2021-1347.
- Strahle, W. C. 1972. "Some results in combustion generated noise." *Journal of Sound and Vibration* 23 (1):113-125. doi: [https://doi.org/10.1016/0022-460X\(72\)90792-4](https://doi.org/10.1016/0022-460X(72)90792-4).
- Sturesson, Peter. 2018. "Sense, Actuate and Survive - Ceramic Microsystems for High-Temperature Aerospace Applications." Doctor of Philosophy in Engineering, Faculty of Science and Technology, Uppsala University.
- Tereshchenko, Yu M., E. V. Doroshenko, A. Tehrani, and J. Abolhassanzade. 2015. "Aerodynamic Factors of Influence on the Resonance Vibration of Gas Turbine Compressor Blades." *Strength of Materials* 47 (5):711-718. doi: 10.1007/s11223-015-9708-1.
- Turbine_Technologies. 2011. Minilab Gas Turbine Power System Operator's Manual. Chetek, WI: Turbine Technologies.
- Valentin Soloiu, Amanda Weaver, Lily Parker, Austin Brant, Ribchard Smith III, Marcel Ilie, Gustavo Molina, Cesar Carapia. 2022. "Constant volume combustion chamber (CVCC) investigations of aerospace F-24 and Jet-A in low-temperature heat release and negative temperature coefficient regions " *Energy Conversion and Management* 263. doi: <https://doi.org/10.1016/j.enconman.2022.115687>.
- Valentin Soloiu, John McAfee, Marcel Ilie, Aidan Rowell, James Willis, Nicholas Dillon. 2024. "Experimental and Numerical Investigation of Combustion and Noise, Vibrations, and Harshness Emissions in a Drone Jet Engine Fueled with Synthetic Paraffinic Kerosene." *SAE Journal of Aerospace* 17 (1). doi: <https://doi.org/10.4271/01-17-01-0006>.

- Vladimir Balepin, Chris Osselo. 2002. "NO_x emission reduction in commercial jets through water injection." American Institute of Aeronautics and Astronautics, Indianapolis, Indiana.
- Wijesinghe, C. J., and B. Khandelwal. 2021. "Impact of aromatic species selection and micro and bulk properties of alternative fuels on atomisation." *The Aeronautical Journal* 125 (1288):1013-1033. doi: 10.1017/aer.2021.6.
- Wijesinghe, Charith J., Yuxiao Ling, and Bhupendra Khandelwal. 2019. "Effect of low aromatic HEFA fuel on effect of gas turbine vibration and instability."
- Wild, Thomas W. 2018. *Aircraft Powerplants*. 9 ed. United States: McGrall-Hill.
- Yaopeng, Li, Jia Ming, Chang Yachao, Xie Maozhao, and D. Reitz Rolf. 2016. "Towards a comprehensive understanding of the influence of fuel properties on the combustion characteristics of a RCCI (reactivity controlled compression ignition) engine." *Energy* 99:69-82. doi: <https://doi.org/10.1016/j.energy.2016.01.056>.
- Yitao, Shen, Shuai Shijin, Wang Jianxin, and Xiao Jianhua. 2009. "Optimization of gasoline hydrocarbon compositions for reducing exhaust emissions." *Journal of Environmental Sciences* 21 (9):1208-1213. doi: [https://doi.org/10.1016/S1001-0742\(08\)62405-5](https://doi.org/10.1016/S1001-0742(08)62405-5).
- Yousufuddin, Syed. 2016. "EFFECT OF COMBUSTION DURATION ON THE OPERATING AND PERFORMANCE CHARACTERISTICS OF A HYDROGEN-ETHANOL DUAL FUELED ENGINE: AN EXPERIMENTAL ANALYSIS." *International Journal of Advances on Automotive and Technology*. doi: 10.15659/ijaat.16.07.323.
- Zheng, Lukai, Paramvir Singh, James Cronly, Emamode A. Ubogu, Ihab Ahmed, Chenxing Ling, Yang Zhang, and Bhupendra Khandelwal. 2021. "Impact of Aromatic Structures and Content in Formulated Fuel for Jet Engine Applications on Particulate Matter Emissions." *Journal of Energy Resources Technology* 143 (12). doi: 10.1115/1.4049905.

APPENDIX A

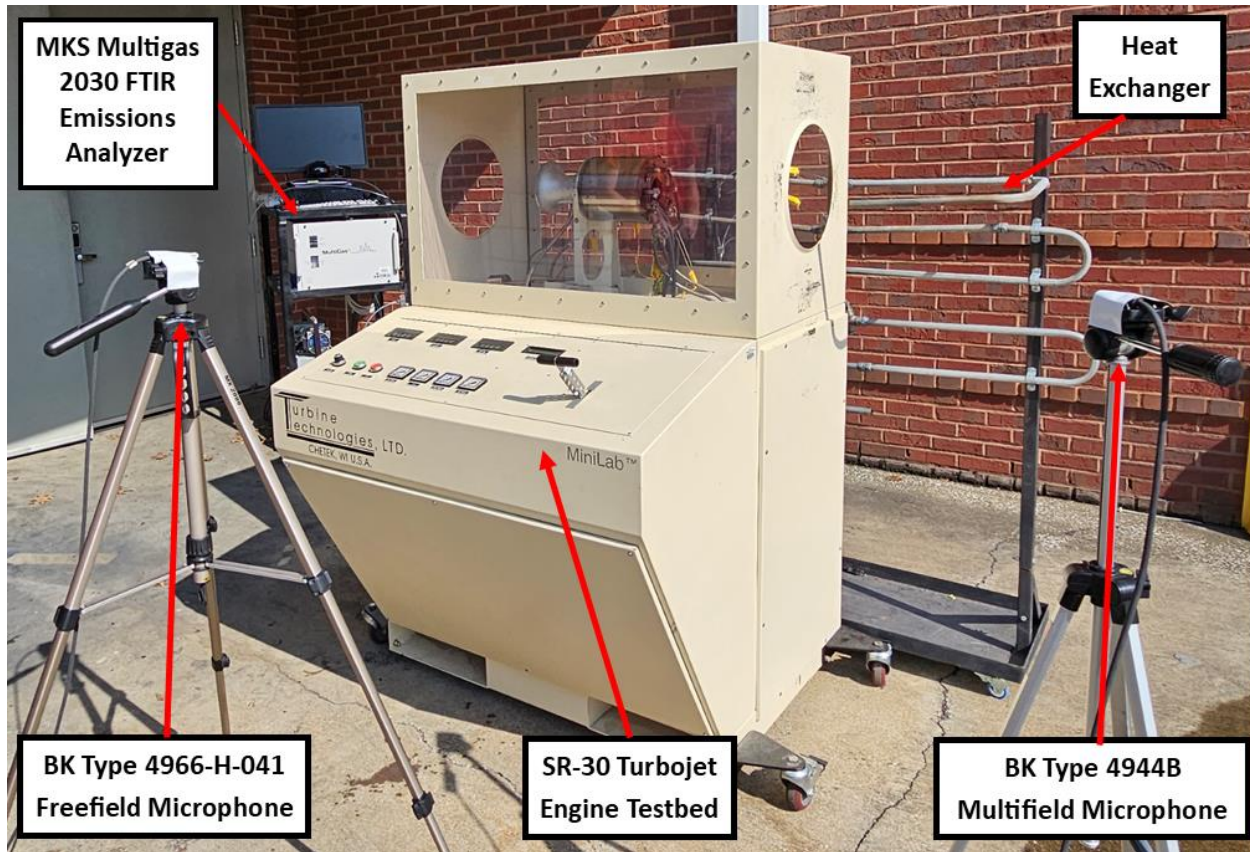


Figure 72: Experimental setup for the noise, vibration, emissions, and gas turbine testing.

Table 10: Temperature for the experimental and numerical simulation of Jet-A and F24

Experiment Type	Fuel	Engine Speed (RPM)	T2 (K)	T3 (K)	T4 (K)	T5 (K)
Experimental Results	Jet-A	60,000	409.1293	830.2309	916.8492	720.1765
		65,000	426.8847	860.3455	929.6301	727.715
		70,000	438.0115	914.9836	935.9014	737.926
	F24	60,000	390.6223	821.1307	880.0839	699.2159
		65,000	406.8063	843.2653	889.0463	699.2234
		70,000	422.9157	873.5551	928.4515	689.8766
Numerical Results	Jet-A	60,000	394.65	1088.34	933.67	737.26
		65,000	411.1	865.85	871.31	781.18
		70,000	477.6	710.05	864.66	949.60
	F24	60,000	394.246	1008.87	851.73	674.73
		65,000	410.78	847.18	791.9	713.69
		70,000	476.84	688.76	812.39	888.61

Table 11: Pressure for the experimental and numerical simulation of Jet-A and F24

Experiment Type	Fuel	Engine Speed (RPM)	P2 (kPa)	P3(kPa)	P4 (kPa)	P5 (kPa)
Experimental Results	Jet-A	60,000	97.02	96.52	7.60	3.06
		65,000	118.66	118.18	8.83	3.59
		70,000	144.75	144.38	10.73	4.66
	F24	60,000	100.14	99.05	7.88	3.21
		65,000	123.30	122.26	9.21	4.65
		70,000	151.92	150.86	11.01	13.18
Numerical Results	Jet-A	60,000	172.51	171.95	31.62	6.97
		65,000	200.27	200.31	36.71	9.40
		70,000	299.86	299.96	64.78	21.70
	F24	60,000	167.00	166.54	30.80	6.86
		65,000	193.95	193.88	35.88	9.29
		70,000	288.87	289.10	62.46	15.94

Table 12: Engine Characteristic for the experimental and numerical simulation of Jet-A and F24

Experiment Type	Fuel	Engine Speed (RPM)	Thrust (N)	Fuel Flow Rate (L/Hr)	AFR	TSFC (kg/N*Hr)
Experimental	Jet-A	60000	35.63	19.32	24.83	0.44
		65000	38.34	21.92	24.80	0.46
		70000	43.38	24.41	25.73	0.45
	F24	60000	38.75	18.29	28.29	0.38
		65000	43.69	20.60	28.74	0.38
		70000	48.09	23.76	28.83	0.40
Simulation	Jet-A	60000	34.83	12.92	33.01	0.37
		65000	47.01	13.49	32.56	0.29
		70000	108.48	16.40	28.74	0.15
	F24	60000	34.29	11.52	36.66	0.34
		65000	46.43	12.02	36.21	0.26
		70000	79.72	15.35	30.29	0.19

Table 13: Experimental emission results for Jet-A and F24

Fuel	Engine Speed (RPM)	Average H ₂ O (%)	Average CO ₂ (%)	Average NO _x (PPM)	Average CO (PPM)	Average THC (PPM)
Jet-A	60000	4.06	2.97	21.67	1213.34	2039.20
	65000	4.03	2.93	23.73	1047.45	1737.35
	70000	4.07	3.02	27.63	959.36	1171.41
F-24	60000	2.89	2.35	18.07	1087.82	952.42
	65000	3.01	2.50	21.69	989.52	667.76
	70000	3.33	2.87	27.61	952.62	480.69

Table 14: Experimental TSFC emission results for Jet-A and F24

Fuel	Engine Speed (RPM)	TSFC Average H ₂ O (%)	TSFC Average CO ₂ (%)	TSFC Average NO _x (PPM)	TSFC Average CO (PPM)	TSFC
Jet-A	60000	10.31%	9.04%	0.66	36.94	62.08
	65000	9.05%	8.91%	0.72	31.89	52.89
	70000	7.19%	9.20%	0.84	29.21	35.66
F-24	60000	6.87%	5.59%	0.43	25.87	22.65
	65000	6.53%	5.42%	0.47	21.45	14.47
	70000	5.93%	5.10%	0.49	16.96	8.56

Table 15: SPL for Jet-A and F24 at each engine speed

Fuel	Engine Speed (RPM)	Parameter	SPL (dB)
Jet-A	60000	Combustion Chamber Max	83.75
		Shaft Max	87
		Maximum	91.25
	65000	Combustion Chamber Max	86.25
		Shaft Max	86.25
		Maximum	95.75
	70000	Combustion Chamber Max	89.25
		Shaft Max	87.5
		Maximum	98
F-24	60000	Combustion Chamber Max	82.5
		Shaft Max	87
		Maximum	92.5

	65000	Combustion Chamber Max	87.5
		Shaft Max	86.25
		Maximum	96.75
	70000	Combustion Chamber Max	92.5
		Shaft Max	90
		Maximum	95.75

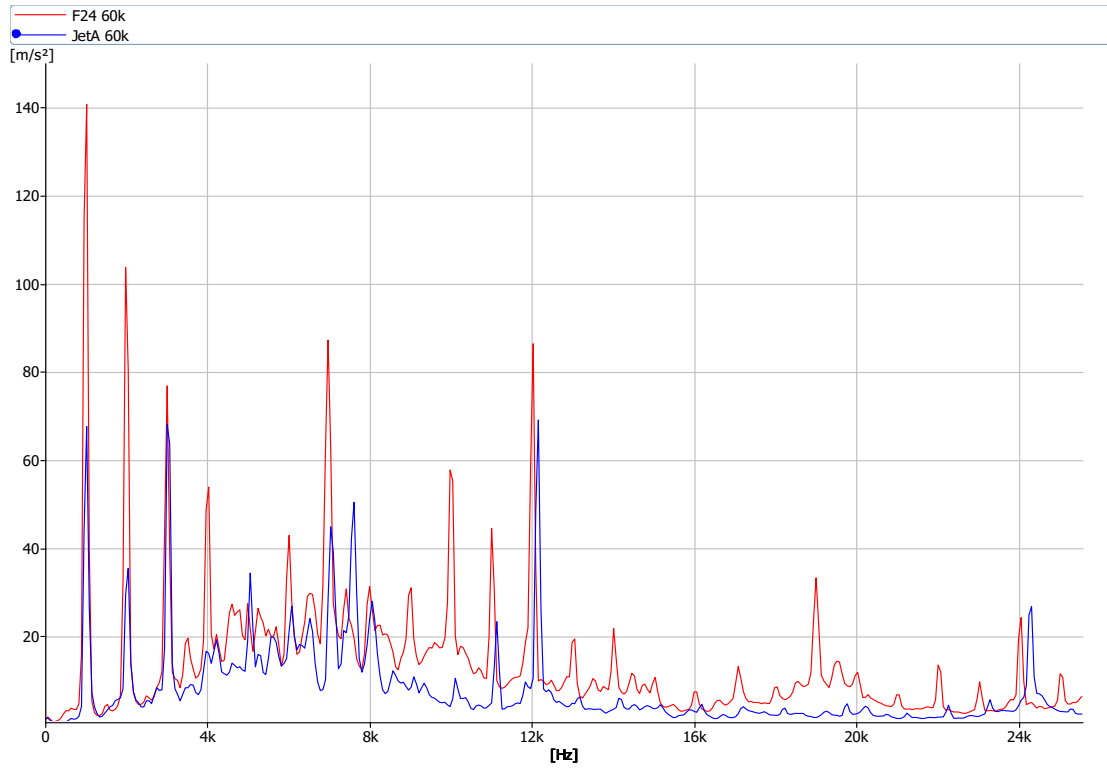


Figure 73: Vibration results for Jet-A and F24 at 60,000RPM.

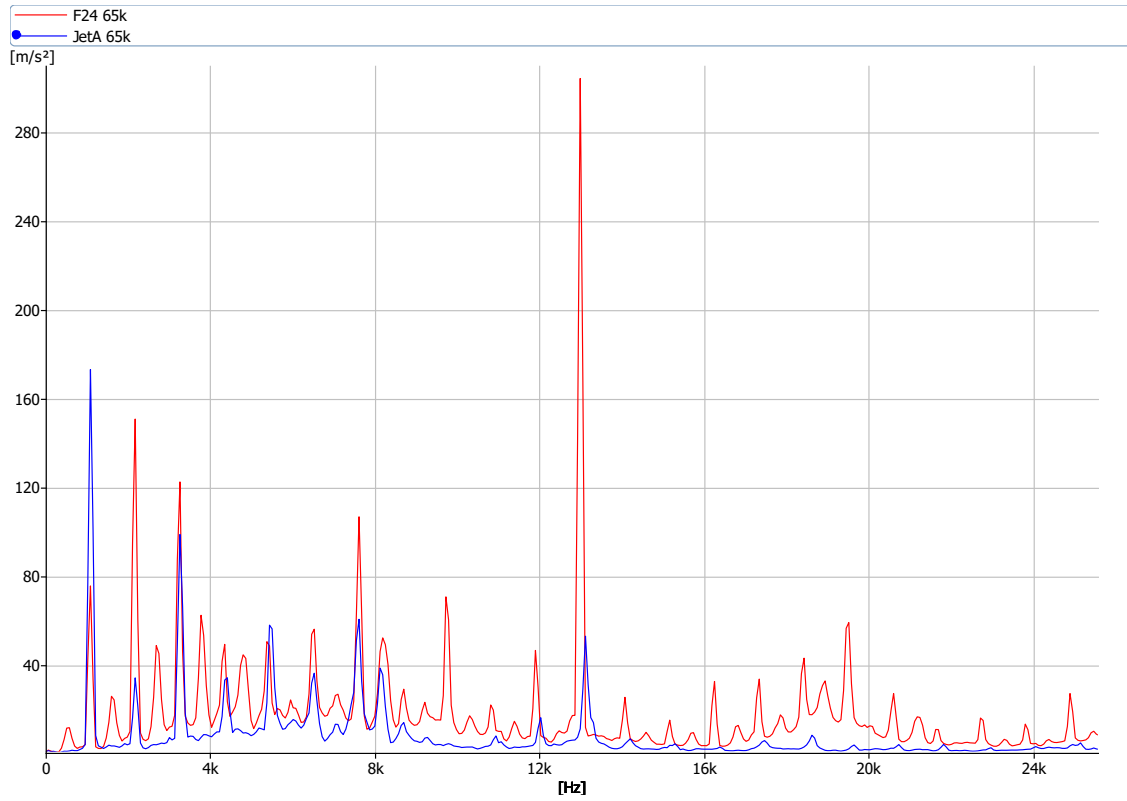


Figure 74: Vibration results for Jet-A and F24 at 65,000RPM.

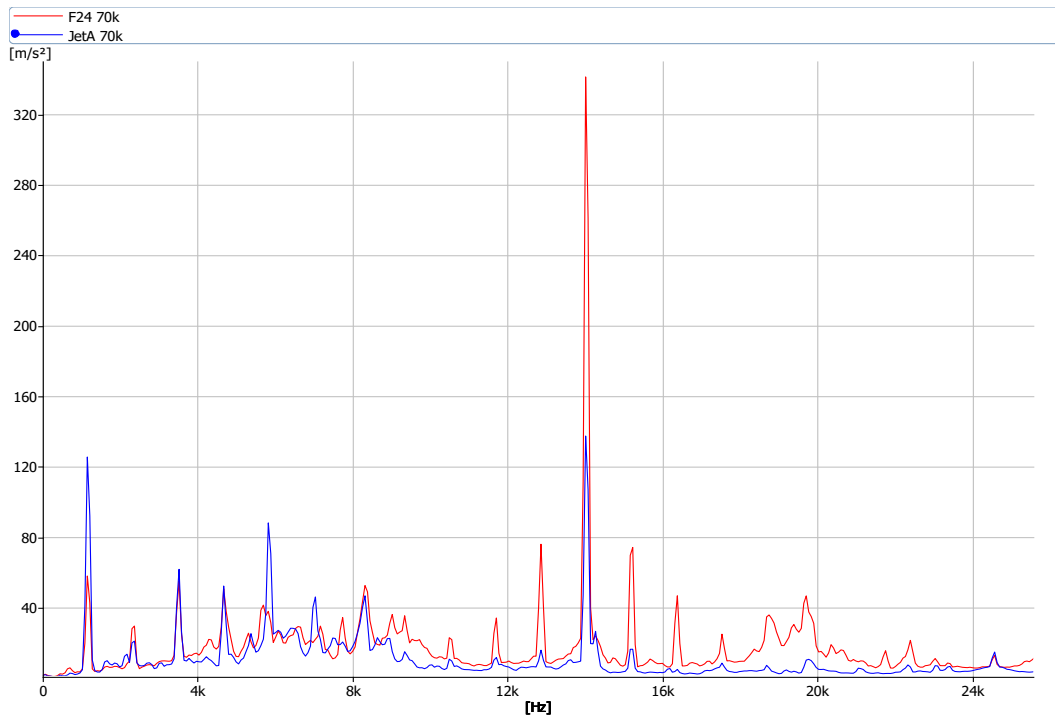


Figure 75: Vibration results for Jet-A and F24 at 70,000RPM.

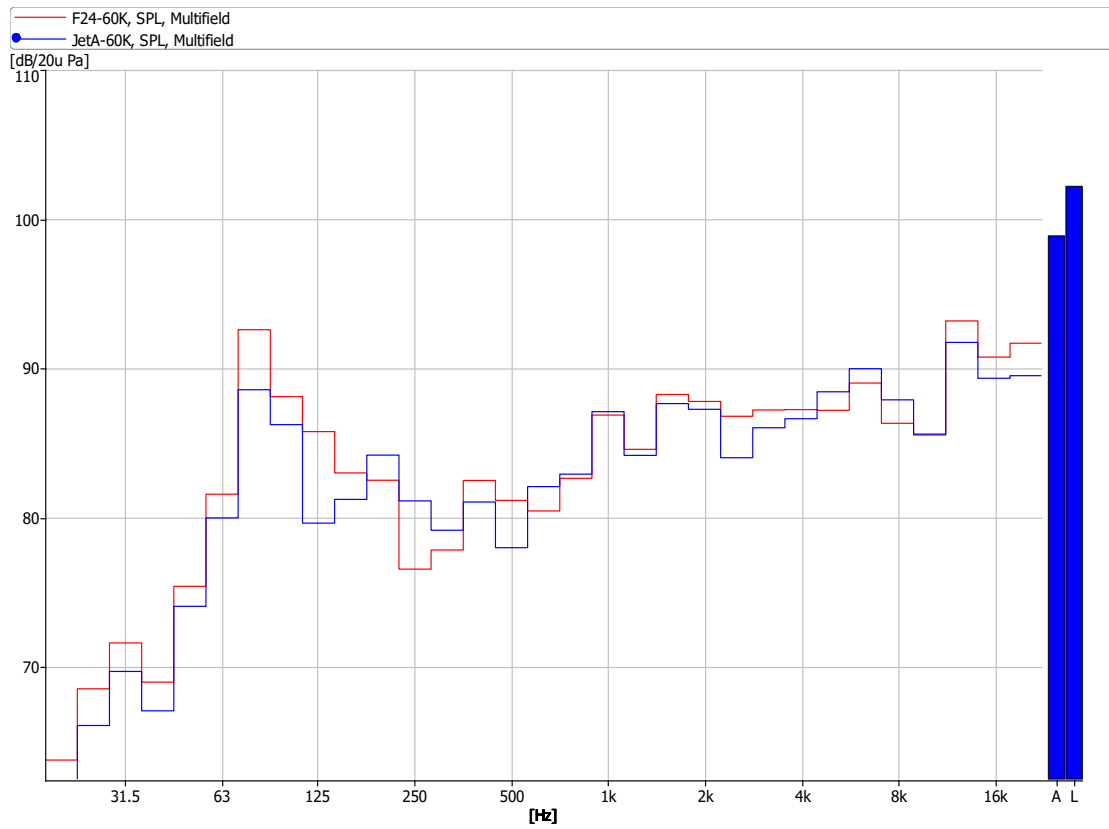


Figure 76: Sound Pressure results from the Multifield microphone for Jet-A and F24 at 60,000RPM.

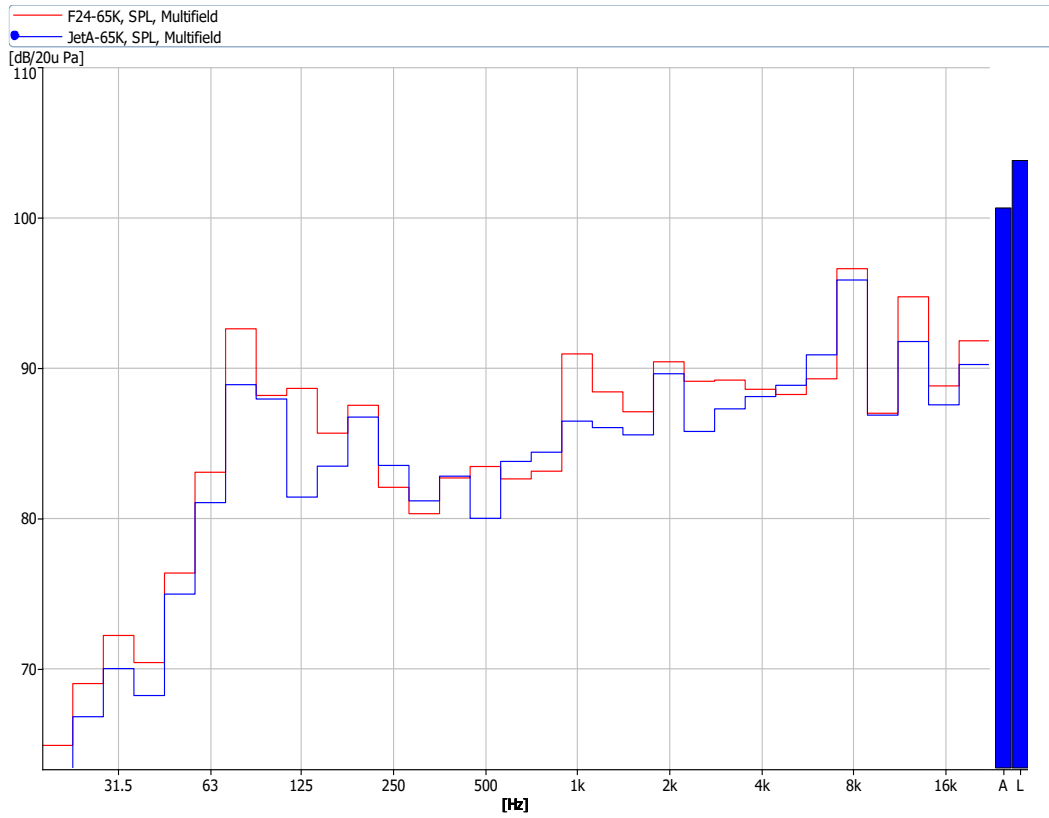


Figure 77: Sound Pressure results from the Multifield microphone for Jet-A and F24 at 65,000RPM.

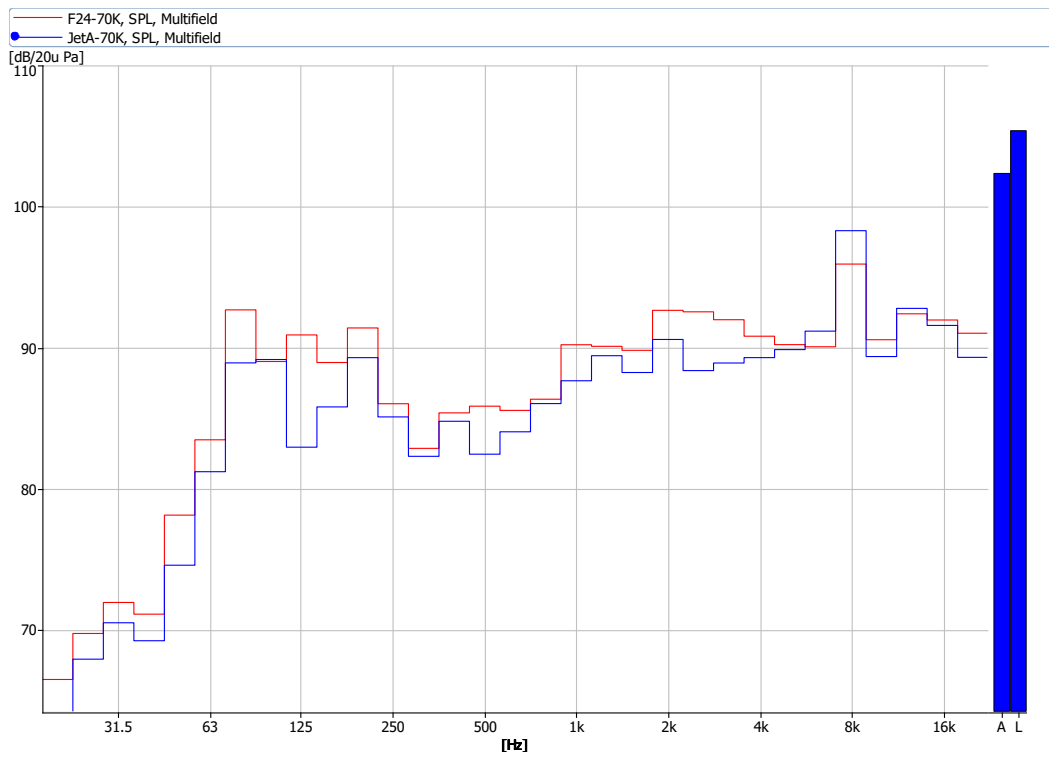


Figure 78: Sound Pressure results from the Multifield microphone for Jet-A and F24 at 70,000RPM.

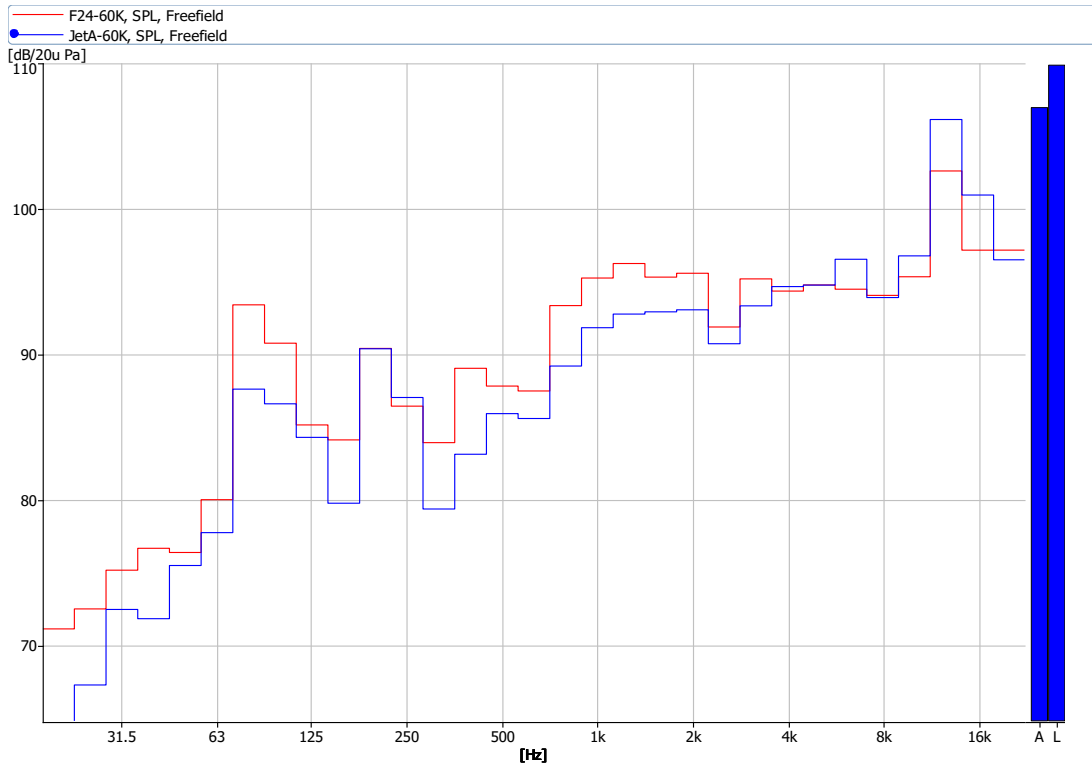


Figure 79: Sound Pressure results from the Freefield microphone for Jet-A and F24 at 60,000RPM

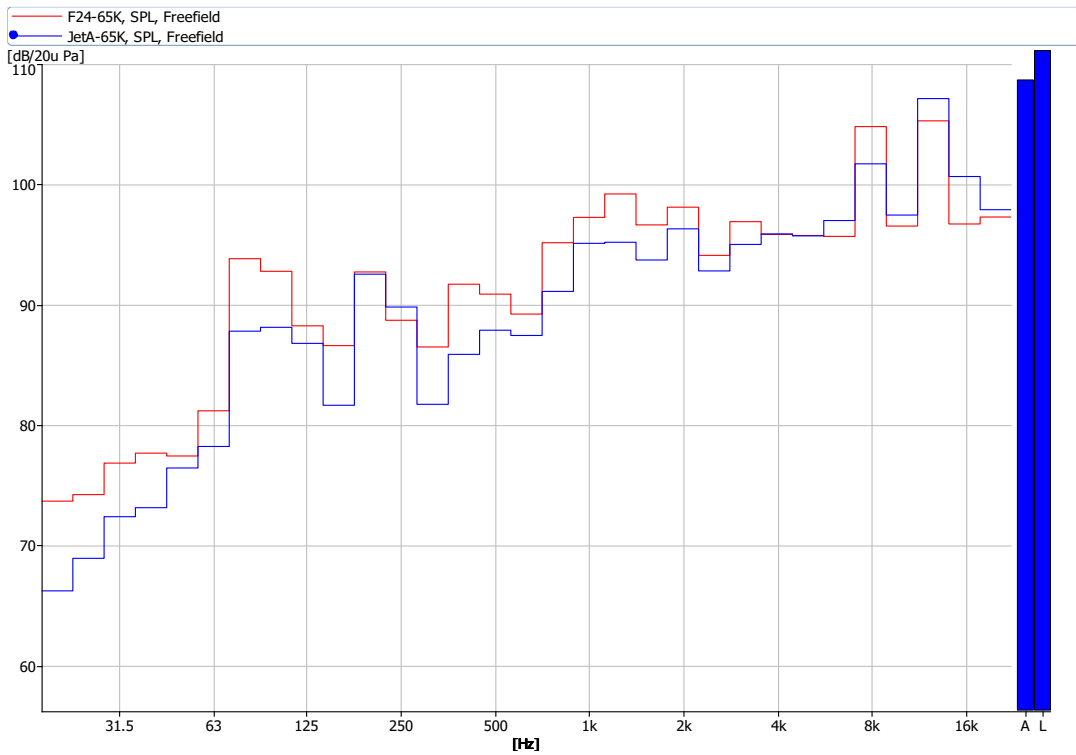


Figure 80: Sound Pressure results from the Freefield microphone for Jet-A and F24 at 65,000RPM.

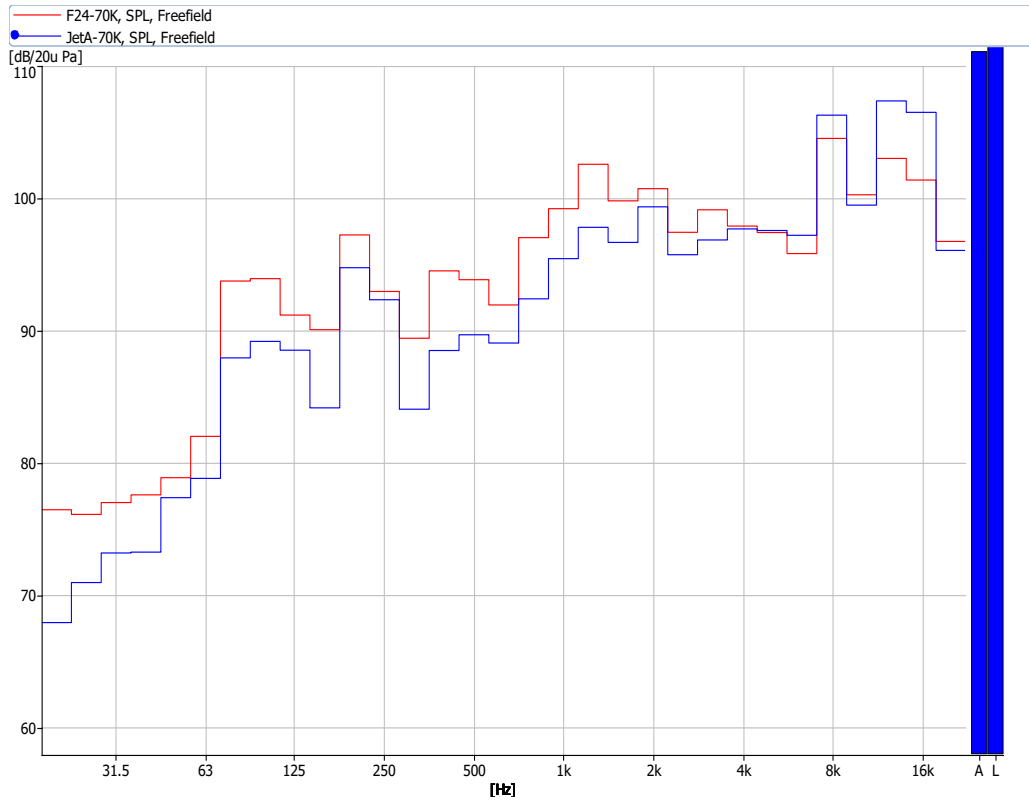


Figure 81: Sound Pressure results from the Freefield microphone for Jet-A and F24 at 70,000RPM.

